A COMPARISON OF MPPT ALGORITHMS FOR HAP-SOLAR POWERED UAV UNDER DIFFERENT CONDITIONS

Master Degree Thesis

Özge KÜÇÜKKÖR

Eskişehir, 2022

A COMPARISON OF MPPT ALGORITHMS FOR HAP-SOLAR POWERED UAV UNDER DIFFERENT CONDITIONS

Özge KÜÇÜKKÖR

Master's Thesis

Department of Civil Aviation

Supervisor: Prof. Dr. T. Hikmet KARAKOÇ

(Co-Supervisor: Prof. Dr. Umut DURAK)

Eskişehir

Eskişehir Technical University

Institute of Graduate Programs

June 2022

This thesis has been supported by the project 121N421 which is approved by the TUBITAK Committee.

15/06/2022

SUPERVISOR APPROVAL

Master's student Özge KÜÇÜKKÖR, whom I supervise, has completed this thesis titled A COMPARISON OF MPPT ALGORITHMS FOR HAP-SOLAR POWERED UAV UNDER DIFFERENT CONDITIONS. According to my inspections, the work is scientifically and ethically appropriate for the student to the thesis defense exam.

Supervisor

Prof. Dr. T. Hikmet KARAKOÇ

ABSTRACT

A COMPARISON OF MPPT ALGORITHMS FOR HAP-SOLAR POWERED UAV UNDER DIFFERENT CONDITIONS

Özge KÜÇÜKKÖR

Department of Civil Aviation

Eskişehir Technical University, Institute of Graduate Programs, June 2022

Supervisor: Prof. Dr. T. Hikmet KARAKOÇ

(Co-Supervisor: Prof. Dr. Umut DURAK)

Nowadays, with the rapid progress of technology, the aviation industry is also developing and shifting to renewable energy sources. With the use of these resources, Solar Powered Unmanned Aerial Vehicles (UAVs) have brought a great innovation to the sector. As a result of the use of the endless energy obtained from the sun in charging the batteries, the flight time of the aircraft has been increased.

Environmental conditions cause nonlinear changes in Photovoltaic (PV) output power. Maximum Power Point Tracking (MPPT) is needed in order to supply the battery and avionics on the aircraft with a constant power using the maximum power point at the PV output power. In short, MPPT keeps the voltage of the system close to the maximum voltage obtained from the PV cells under variable conditions. Thus, by ensuring that the maximum power extracted from the PV panel is fed to the battery on the aircraft with a constant current, a longer flight can be achieved and health of the battery can be protected.

This thesis study has been prepared with reference to the High Altitude Platform (HAP)-Alpha UAV project developed within German Aerospace Center (DLR). With taking into account the technical features of the UAV used in this HAP Project MATLAB/Simulink models for MPPT have been developed. Afterwards, the MPP tracking efficiencies of Perturb and Observe (P&O), Incremental Conductance (InCond) and Hill Climbing algorithms on the system were investigated for simulated MPPT, which is planned to be used in UAV. The simulation results were compared for different temperature and altitude values, and predictions were made about which algorithm works more efficiently under different conditions.

Keywords: HAP, Solar powered UAV, MPPT, Algorithm, Efficiency.

ÖZET

FARKLI KOŞULLAR ALTINDA YÜKSEK İRTİFA PLATFORMU-GÜNEŞ ENERJİLİ İHA'LAR İÇİN MGNİ ALGORİTMALARININ KARŞILAŞTIRILMASI

Özge KÜÇÜKKÖR

Sivil Havacılık Anabilim Dalı

Eskişehir Teknik Üniversitesi, Lisansüstü Eğitim Enstitüsü, Haziran 2022

Danışman: Prof. Dr. T. Hikmet KARAKOÇ

İkinci Danışman: Prof. Dr. Umut DURAK

Günümüzde, teknolojinin hızla ilerlemesi ile havacılık sektörü de gelişme göstermekte ve yenilenebilir enerji kaynaklarına yönelmektedir. Bu kaynakların kullanılmasıyla güneş enerjili insansız hava araçları (İHA), sektöre büyük bir yenilik getirmiştir. Bataryaların şarj edilmesinde güneşten elde edilen sonsuz enerjinin kullanılması sonucu hava araçlarının havada kalış süreleri arttırılmıştır.

Güneş enerjili İHA'lerde kullanılan fotovoltaik (FV) cells çevre koşullarından oldukça etkilenmekte ve bu çevre koşulları FV çıkış gücünde doğrusal olmayan değişimlere sebep olmaktadır. Hava aracı üzerindeki bataryanın ve aviyoniklerin FV çıkış gücündeki maksimum güç noktasıyla sabit bir güçle beslenebilmesi için MGNİ'ye ihtiyaç duyulur. Kısaca MGNİ, değişken şartlar altında sistemin voltajını FV hücrelerden elde edilen maksimum voltaja yakın tutmaktadır.

Bu tez çalışması Alman Havacılık ve Uzay Ajansı (DLR) bünyesinde geliştirilen yüksek irtifa platformu (YİP) HAP-Alpha İHA projesi referans alınarak hazırlanmıştır. Bu HAP projesinde kullanılan İHA'nın teknik özellikleri dikkate alınarak MATLAB/Simulink üzerinde modeller geliştirilmiştir. Sonrasında İHA'de kullanılması planlanan MGNİ için İzle ve Gözle (P&O), Artımsal İletim (InCond) ve Tepe Tırmanışı algoritmalarının sistem üzerindeki MPP takip verimlilikleri araştırılmıştır. Ortaya çıkan sonuçlar farklı temperature ve altitude değerleri için karşılaştırılmış, ve değişen koşullar altında hangi algoritmanın daha verimli çalıştığı hakkında kestirimlerde bulunulmuştur.

Anahtar Sözcükler: YİP, Güneş enerjili İHA, MGNİ, Algoritma, Verimlilik.

ACKNOWLEDGEMENTS

I would like to thank my advisors, Prof. Dr. Tahir Hikmet KARAKOÇ and Prof. Dr. Umut DURAK for providing all the support and knowledge during the preparation of this thesis, Lect. Bahadır CİNOĞLU who tried to guide me in every aspect of my study, and all my valuable teachers and friends who did not hesitate to share their knowledge and experience.

I would like to express my gratitude and love to my dear father Selamet and my dear mother Seçil KÜÇÜKKÖR, who have been by my side all my life and made many sacrifices in their lives to get me where I am today. I would like to express my endless thanks to my siblings Ömür and Gözde KÜÇÜKKÖR, who have always supported me in all matters and put forth their best..

Özge KÜÇÜKKÖR

15/06/2022

STATEMENT OF COMPLIANCE WITH ETHICAL PRINCIPLES AND RULES

I hereby truthfully declare that this thesis is an original work prepared by me; that I have behaved in accordance with the scientific ethical principles and rules throughout the stages of preparation, data collection, analysis and presentation of my work; that I have cited the sources of all the data and information that could be obtained within the scope of this study, and included these sources in the references section; and that this study has been scanned for plagiarism with "scientific plagiarism detection program" used by Eskişehir Technical University, and that "it does not have any plagiarism" whatsoever. I also declare that, if a case contrary to my declaration is detected in my work at any time, I hereby express my consent to all the ethical and legal consequences that are involved.

Özge KÜÇÜKKÖR

CONTENTS

Page

LIST OF TABLES

Page

LIST OF FIGURES

LIST OF IMAGES

GLOSSARY OF SYMBOLS AND ABBREVIATIONS

CO	:	Carbon Monoxide
CO_2	:	Carbon Dioxide
N	:	Nitrogen
SO	:	Sulfur Oxide
Ni-Cd	:	Nickel-Cadmium
HALE	:	'High Altitude Long Endurance
HALSOL	:	High Altitude Solar
ERAST	:	Environmental Research Aircraft and Sensor Technology
DLR	:	German Aerospace Center
HABLEG	:	High Altitude Balloon Launched Experimental Glider
ELAHA	:	Elastic Aircraft for High Altitudes
HAP	:	High-Altitude Platform
MPPT	:	Maximum Power Point Tracking
UAV	:	Unmanned Aerial Vehicles
PV	:	Photovoltaic
DC	:	Direct Current
I	:	Current
V	:	Voltage
P	:	Power
Mono c-Si	:	Monocrystalline Silicon
Poly-Si	:	Polycrystalline Silicon
Ga	:	Gallium
As	:	Arsenic
A-Si	:	Amorphous Silicon
SiH_4	:	Silane
CdTe	:	Cadmium Telluride
CIS	:	Copper Indium Diselenide
CIGS	:	Copper-Indium Gallium Diselenide
D	:	Duty Cycle
PWM	:	Pulse Width Modulation

L	:	Inductance
C	:	Capacitor
FBT	:	Flyback Converter
SRC	:	Series Resonant Converter
PRC	:	Parallel Resonant Converter
$ZnSO_4$	:	Zinc Sulfate
Cu_2SO_4	:	Copper(II)Sulfate
NiMH	:	Nickel Metal Hydride Batteries
Li-Ion	:	Lithium-Ion Batteries
LiPo	:	Lithium Polymer Batteries
Li-S	:	Lithium-Sulfur
EU	:	European Union
CFRP	:	Carbon Fiber Reinforced Polymer
InGap	:	Indium Gallium Phosphide
GaAs	:	Gallium Arsenide
InGaAs	:	Indium Gallium
ELO	:	Epitaxial Lift-Off
AM	:	Air Mass
MACS	:	Modular Aerial Camera System
DOAS	:	Differential Optical Absorption Spectroscope
HAPSAR	:	High Altitude Platform Synthetic Aperture Radar
MPP	:	Maximum Power Point
P&O	:	Perturb and Observe
InCond	:	Incremental Conductance
NOCT	:	Nominal Operating Cell Temperature

1. INTRODUCTION

The world population is constantly increasing. Along with the increasing population, technological developments are accelerating due to the competitive environment in the sectors serving this population. With the developing technology, the industry and industrial area are growing, and the energy needed increases accordingly. This needed energy is generally met from fossil fuels such as natural gas, oil, and coal, which have limited resources.

The use of fossil energy sources in the industrial field is quite common. Electricity is generated with the energy produced as a result of the combustion of these fossil fuels. In the 19th and 20th centuries, especially after the industrial revolution, with the ever-increasing need for energy, these limited fossil fuel reserves are decreasing, and there is an increasing concern about the consequences of these decreases. In addition, increasing fossil fuel consumption negatively affects the environment, human health and causes a global warming problem by creating a greenhouse effect (Pandey et al., 2016). According to studies conducted in recent years, 34.7% of primary global energy use originates from petroleum, 9.9% from coal, and 34% from natural gas (EIA, 2021). In other words, it can be said that approximately 78.6% of the obtained energy originates from fossil fuels. Emissions arising from the combustion of these fossil fuels have become a primary problem for countries. Gases harmful to nature such as carbon monoxide (CO), carbon dioxide (CO_2), nitrogen (N), sulfur oxide (SO) in these emissions are released into the atmosphere.

The greenhouse effect occurs with the accumulation of greenhouse gases, mainly the emission of fossil fuels (Shpirt and Goryunova, 2009). These gases create a greenhouse effect in the atmosphere, keeping the sun's rays on the earth, and as a result, the temperature of the earth increases. Due to the increase in the greenhouse effect due to fossil fuel consumption, problems such as global warming and climate change arise. These problems created by fossil fuel consumption pose significant risks to the health of living things, and their environmental impacts are substantial (Lelieveld et al., 2019). Moreover, it poses a threat to the sustainability of resources (Whiting et al., 2017). These dangers have become increasingly global over time. Academic studies have focused on this field to find alternative solutions and eliminate the damages of this energy source, which causes many serious problems worldwide. Many theoretical and experimental studies are carried out on the subject, and new potential solutions are presented according to the results obtained. With the developing technology, these solutions have been divided into many areas and have recently become the focus of researchers.

One of the most prominent solutions among the presented potential solutions is sources (Dyatlov at al., 2020). Such resources have gained critical importance in recent year due to not stealing from the future generations' resources and being "sustainable" in that their negative effects on the environment are minimal (York and Bell, 2019). The use of renewable energy sources can reduce environmental pollution and meet the energy needs without posing a threat to the health of living things. In addition, these resources do not face the problem of depletion. This will also reduce concerns about the energy crisis. Thus, future generations can be provided with a healthier environment without compromising the resources by using them whilst not consuming. Many energy sources such as solar energy, wind energy, geothermal energy can be given as examples of renewable energy sources. These resources have attracted attention due to their environment-friendly, cheap and renewable nature and studies on this subject have increased. Today, solar energy is one of the most preferred sources in terms of its easy access, unlimited source, low amount waste, low cost, long warranty periods of solar panels, suitability for modular design and ease of maintenance. (Hegedus and Luque, 2003).

The conversion of solar energy to electrical energy is done using solar panels. Electricity is obtained by the photons from the sun hitting the photovoltaic panel surface during the day. With this technology, the use of solar energy has increased rapidly to meet the electrical energy needed in most technological devices today. One of the places where these photovoltaic panels are tried to be used most frequently is the aviation industry. This technology, which has the potential to create a solution to the limited energy source on the aircraft, has breathed a new life into the aviation industry. (Abbe and Smith 2016).

From the past to the present, the energy problem in aircraft has always been a subject that has been studied. Electrical energy plays a critical role in feeding the avionics on the aircraft and ensuring flight continuity throughout the flight period. In this case, the solar energy system has become a new solution for the problem caused by the limited energy sources. With the integration of the solar energy system into the aircraft, these vehicles have become more advantageous compared to conventional aircraft by means of reduction in the pollution caused by CO_2, SO_X and NO_X emissions (Sukumaran and Sudhakar, 2017), the reduction in the amount of noise as Db and the increase in sustainability (Zhang et al., 2021). In the meantime, as a result of integration of alternate energy sources into aircraft a newly found field of study has been created on storing the power that is generated. There exists ongoing studies on this subject since there is a potential for battery technology to provide the necessary power in solar-powered aircrafts under various conditions.

1.1. Background of Solar Powered Aircraft

Since the first flight experiments in the world, the aviation industry has always been intertwined with the developing technology. Technological developments, which gained momentum especially after the industrial revolution, contributed to the rapid growth of civil aviation and paved the way for the formation of today's sustainable and modern aviation sector.

With the development of the aviation industry, traditional energy sources are replaced by renewable sources over the years. For many years, improvements in renewable energy technology have increased the number of studies done on utilization of solar-powered systems on aircraft

The first successful development as solar powered aircraft started in 1884, when Charles Renard and Arthur Krebs used electrical energy on aircraft. They traveled a distance of 8 km in 23 minutes with an electric motorized airship (Image 1.1) belonging to the French Army. This airship, with a length of 170 ft (~51 m) and a volume of 66000 ft^3 (~1869 m^3), which has an 8.5 horsepower electric motor, made the first fully controllable free flight. Although this was a big step against steam engines at that time, the necessary importance was not achieved with the start of the use of gasoline engines. This is why the development of electrical systems on aircraft has been delayed for some time. (Boucher, 1984).

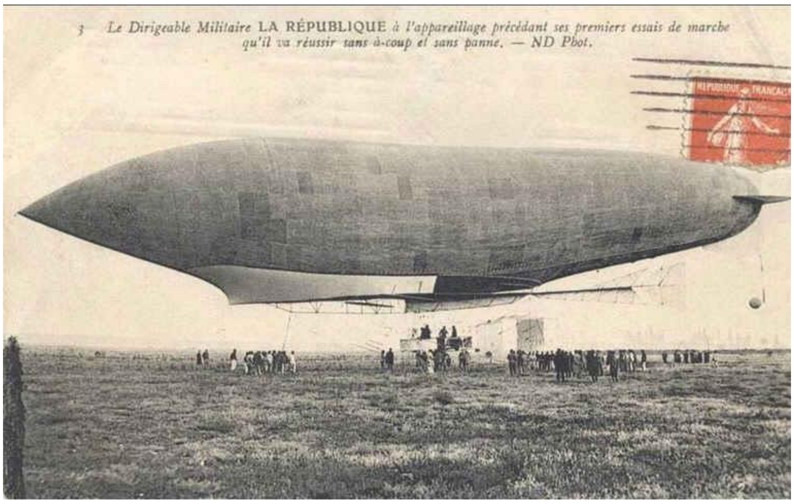

Image 1.1. *The 'La République' on the ground, ready to take-off (http-1)*

After many years, on June 30, 1957, a radio-controlled-electric aircraft was flown in the United Kingdom, which was the first of its kind in official records. This aircraft, which they named Radio Queen (Image 1.2), used a permanent magnet engine and silver-zinc battery, and the first successful flight was made by a German citizen, Fred Militky, in October of the same year. (Kranjec et al., 2018). After this flight, the developments in the engines and batteries gained importance, and these developments also contributed to electric flights.

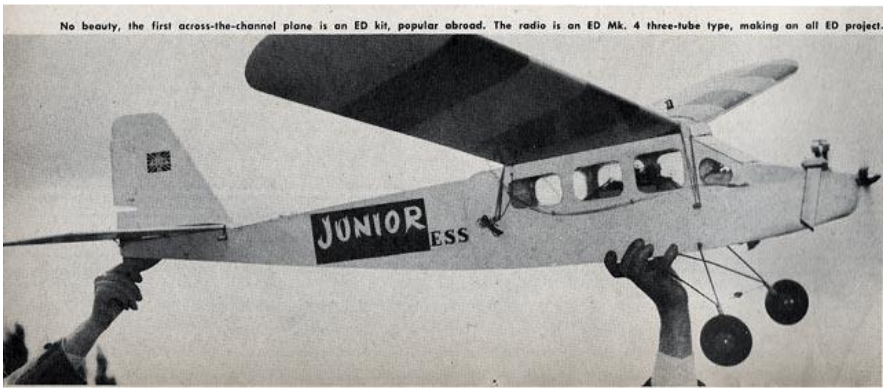

Image 1.2. *The Radio Queen (http-2)*

On November 4, 1974, the first flight of the solar-powered unmanned aerial vehicle, called Sunrise-I (Image 1.3), was carried out in California. Designed by Astro Flight Inc, the aircraft completed its flight in 20 minutes at approximately 330 ft. cruising altitude. The aircraft's design features are 9,76 m wingspan, 12,25 kg weight, and 4096 solar cells. 450W power was generated with the panels consisting of these cells on the aircraft. (Boucher, 1984).

Image 1.3. *The Sunrise I*

After Sunrise-I was damaged during flight, the design features of this aircraft were improved, and the Sunrise-II (Image 1.4) was produced on September 12, 1925. In Sunrise-II, the weight was reduced to 10,21 kg, and 4480 solar cells with 14% efficiency were used. In this way, 600W of power was produced from the solar cells. (Boucher, 1985).

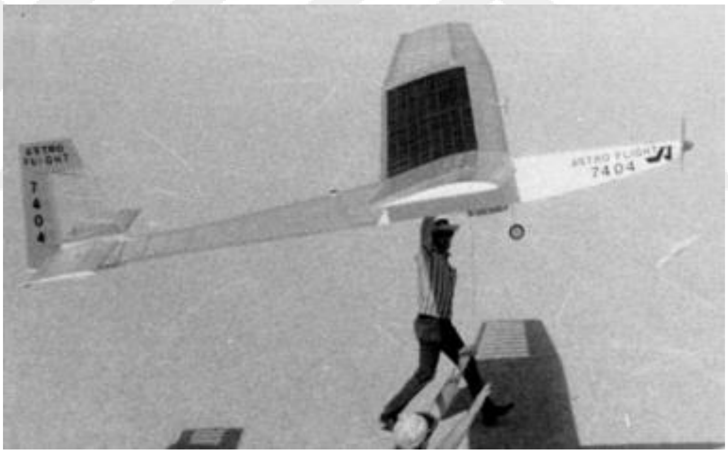

Image 1.4. *The Sunrise II*

Studies on solar-powered aircraft accelerated in Germany, and Solaris (Image 1.5) was manufactured in 1975. Flight attempts were unsuccessful due to overheating problems in solar cells in the first studies. However, in 1976 it broke fresh ground in Europe by accomplishing 150 seconds of flying at 165 ft after overcoming this issue. (Bruss, 1991).

Image 1.5. *The Solaris*

In 1978, a Ni-Cd (Nickel-Cadmium) battery was used in the Solar One (Image 1.6) aircraft to meet the necessary energy needs, and a short flight was carried out. Afterward, Solar Riser was manufactured in 1979, and solar panels were placed on its wings. As a result, 350W of power was produced with these solar panels. However, this generated power could not meet the required power for the engine on the aircraft. The Ni-Cd battery in the aircraft was charged with solar cells during a 3-hour flight. As a result, it was observed that the batteries were charged to keep the aircraft in the air for only 10 minutes. Solar Riser was able to fly for 800 m at altitudes ranging from 1.5-5m.

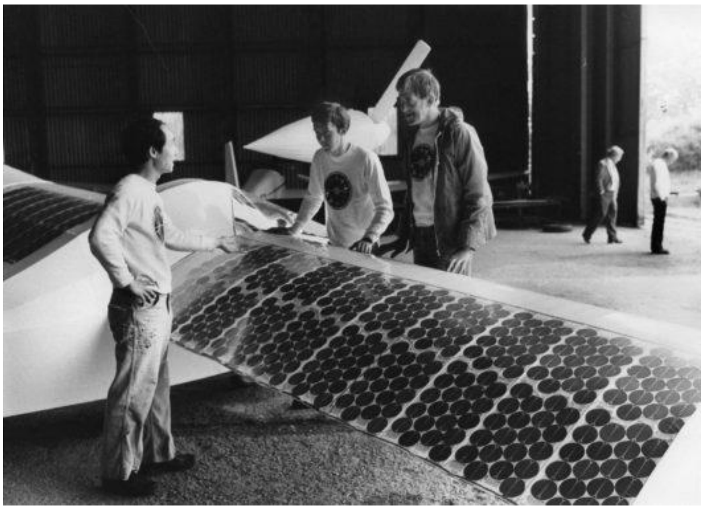

Image 1.6. *The Solar One*

After the manufacture of electric airplanes, the manufacture and development of solar-powered airplanes have gained momentum. The successful flight of solar-powered aircraft when adequate sunlight is provided has inspired the development of new generation solar-powered aircraft. These studies have moved solar-powered aircraft forward, and depending on the results of the tests, they have gained new features such as an increase in altitude and flight time. After many studies and flight trials, the aviation industry has dreamed of manned solar-powered aircraft.

Since 1978, solar-powered manned aircraft studies have increased and many flights have been carried out. With the flight tests of the designs carried out, mostly in Germany and the United States, improvements have been made in solar-powered aircraft. Many flights have been made, notably Gossamer Penguin (Image 1.7), which is considered the world's first piloted solar-powered flight in 1980. (Boucher, 1984). Parallel to the advances in these aircraft, the energy systems of these aircraft have also been developed. With the increase in the power requirement of the avionics in the system and the flight range of the aircraft, the energy sources used in these aircraft have started to play an important role. With the studies on energy storage systems, an increase in flight time has been achieved.

Image 1.7. *The Gossamer Penguin (http-4)*

Each development in solar-powered aircraft has created more curiosity and desire to do more in human beings. This situation has brought solar-powered aircraft to a different dimension by causing variability in flight conditions. Each development in solar-powered aircraft has created more curiosity and desire to do more in human beings, and this has brought solar-powered aircraft to a different dimension due to the various flight conditions required.

1.1.1. High Altitude Long Endurance (HALE) platforms

As aircraft develop, their capabilities increase day by day. Thus, successful flights were carried out at high altitudes. On the other hand, there have been advances in battery technology that supports flights at these altitudes. As a consequence, the advanced technological batteries, long flights are provided at high altitudes. These developments have led to forming a new platform in the aviation industry, and the concept of 'High Altitude Long Endurance (HALE) has emerged. Afterward, the HALE platform has become an important alternative to achieve many purposes, and these platforms have many different uses (Runge et al., 2007). Main examples of these are telecommunication applications, security and remote sensing. (Romeo and Frulla, 2004). These usage areas provide advantages in satellite and terrestrial/airborne infrastructure. Due to these advantages, the development of HALE platforms from past times to the present is observed.

After successful studies, a solar-powered aircraft capable of flying over 19,812 km (65,000 ft) was developed in the USA. Although the first studies were carried out on High Altitude Solar (HALSOL) in 1983, they were unsuccessful due to the inadequacy of the energy source. Then, in 1993, Pathfinder (Image 1.8) successfully flew with solar energy. Pathfinder, which belongs to Environmental Research Aircraft and Sensor Technology (ERAST) program, is designed to have a wingspan of 30 m and a weight of 254 kg. In 1995, it reached an altitude of 15390 meters and held the world altitude record. Pathfinder Plus has emerged with the increase of the wingspan of this aircraft over time and the integration of new technologies. (Boucher, 1984). This aircraft broke a new record by reaching an altitude of 24400 meters (Hoffborn, 2009).

Image 1.8. *The Pathfinder*

Between 1997 and 1999, the Centurion was designed as a scientific sampling and imaging aircraft capable of flying for months. The design of this aircraft has been a technological inspiration to many solar-powered aircraft. Enabled by its structural features, Centurion can fly at an altitude of 80,000 ft with its 45 kg mission equipment. Although the lithium battery placed to be used during these flight operations provided energy for up to 5 hours after sunset, it could not provide enough energy for the flight during the night.

After the problem with the lack of energy, this problem was solved with Helios. Due to its battery, which can provide enough energy for all-night flights, it was named "Eternal Aircraft". This aircraft is capable of continuous flight at an altitude of 100,000 ft, with at least 14 hours of its 24-hour continuous flight above 50,000 ft. As a result, it has improved the world record in this field by flying at approximately 96,000 ft in 2021. It was possible to fly for 40 minutes at this altitude.

1.1.2. Previous HALE platform studies at DLR

Studies on aircraft that provide high altitude endurance (HALE) at high altitude have become popular over the years in Europe. The design and development of HALE platforms for many purposes, especially for commercial applications, are illustrated. DLR (German Aerospace Center) has also been involved in the development of HALE platforms and has become a pioneer in Europe in this regard. By combining the knowledge of researchers working within DLR and the fields of study of young researchers, they have been bringing innovative approaches to the field of solar-powered aircraft for many years.

At first, Strato 2C and Icare 2 aircraft were developed with the studies including DLR. Between 1994 and 1998, “Solitair” was developed by the DLR Flight Systems Institute.

The designed 'Solitair' aircraft has a 5.2 m wide wingspan in terms of technical features. It has a net weight of 8 kg with a payload of 0.4 kg. The propulsion of this remotely controlled aircraft is provided by two solar-powered engines (Hepperle et al., 2007). It has adjustable solar panels on its body as shown in Image 1.9. These solar panels provide a way to measure maximum solar radiation. Thus, it can perform a longer flight with more power provided by the PV panels (http-5).

Image 1.9. *The Solitair (Runge et al., 2007)*

After the Solitair project developed by DLR for high-altitude flights, the number of the studies on this subject have increased. Afterward, aircraft equipped with new technological equipment such as 'HABLEG (High Altitude Balloon Launched Experimental Glider)' and 'ELAHA (Elastic Aircraft for High Altitudes)' developed for high altitude flights added a plethora of field of studies and applications to HALE platforms. In addition, after this project, many research studies have been carried out on solar-powered aircraft within DLR until today. One of these studies is the DLR High Altitude Platform (HAP) project, which is currently being worked on.

1.2. Aims of The Study

The aim of this thesis is to evaluate the performance of the algorithms used in MPPT technology, which utilizes the power obtained from solar panels in solar-powered aircraft at maximum values, under different conditions. The system design developed within the scope of the thesis was made with reference to the DLR HAP project, which is a HALE platform. Different output power efficiencies of the PV (photovoltaic) panels used on this designed system under different irradiance and temperatures have been calculated. A comparison of the power to charge the battery was made according to the calculated efficiencies. The different powers obtained from this PV panel have traditionally been tracked by the 3 most used algorithms. System analysis was performed by comparing the tracking efficiency of 3 different algorithms under environmental conditions. Maximum power will be extract from the PV panels via the MPPT, which is operated with the most efficient algorithm. In this way, by increasing the amount of voltage and current obtained from the PV panels, it will be easier for the HALE platform vehicles to stay in the air for a longer time. Thus, it will be possible to charge the batteries in the system with higher values. In addition, the use of MPPT (Maximum Power Point Tracking) with the appropriate algorithm according to the flight conditions in the solar-powered aircraft with the obtained data will ensure that the avionics and batteries on the aircraft can be fed at constant power. Thus, the battery life, charging speed, and charging efficiency of the aircraft will be increased.

1.3. Thesis Organization

The thesis consists of 6 main parts. In the first chapter, a general introduction to the thesis topic was made, general information are given about the aircraft that was referenced during the development of the thesis, and the purpose of writing the thesis is stated. In the second part, PV panels, converters, and batteries used in aircraft solar systems are examined and detailed information is given. In the third chapter, detailed information about DLR High Altitude Platform Alpha are given. The purpose and aim, design of solar cells, battery technology and load systems of this UAV are mentioned in detailed. In the fourth chapter, MPPT and the most widely used traditional MPPT algorithms, which form the basis of the thesis, are emphasized. In the fourth chapter, the model design, which is the purpose of this thesis, and the comparison of the MPPT algorithms used in the system are given. In the fifth chapter, the subject is discussed by comparing the efficiency of the algorithms analyzed in the system and is further elaborated upon by including suggestions. In the sixth chapter, a general conclusion is made about the results of the study in the thesis. Furthermore, the test results are discussed and ideas for possible future studies are given.

2. SOLAR AIRCRAFT TECHNOLOGIES

2.1. Solar Cell Systems

Solar cells, which form the smallest unit of the solar energy system, constitute photovoltaic systems. Therefore, solar cell structures are also called 'photovoltaic' cells, which are formed by using the words 'photon' meaning light in Greek and 'voltaic' from Alessandro Volta. Invented at the beginning of the 19th century, these panels are the result of the physical effect observed by the French physicist Alexandre Edmond Becquerel in his studies. The working logic of solar cells, developed in line with this effect, is based on the principle of conversion of sunlight into electrical effect. Since its invention, many researchers, including important scientists such as Albert Einstein and Nikola Tesla, have made important contributions to this subject. As a result of these studies, many usage areas of solar cells have emerged.

2.1.1. The structure of PV modules

The light from the sun is converted into DC electrical energy via photovoltaic cells. Since the output power obtained from a single cell is insufficient, in order to increase this power, photovoltaic cells in different numbers are connected to each other in series or parallel depending on the power needed (Messenger and Ventre, 2004). The structure obtained by connecting these multiple solar cells to each other in series or parallel is called a PV module. With the increase of the power obtained by observing the connection structure of the PV module, systems of different sizes can be operated, and the structure formed by connecting these modules is called a PV array. The relationship between these 3 basic terms is shown in Figure 2.1.

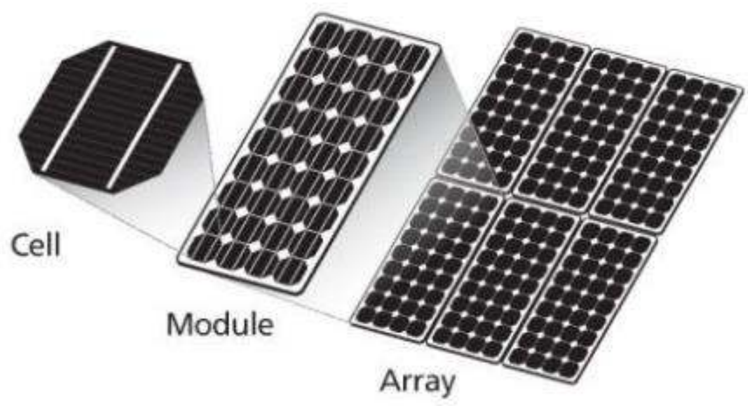

Figure 2.1. *A Typical Photovoltaic Panel Illustration*

The general structures of these cells can be designed as a square, rectangular or circular. It is formed by combining the materials that provide the properties of the PV panel during its production in a layered structure. Since this structure is thin and fragile, it is necessary to use a protective frame with glass.

In order to minimize the effects due to physical effects, a frame structure made of aluminum material may be preferred. With this frame structure, the assembly infrastructure of the PV cells is built.

2.1.2. Type of solar cells

Solar cell types differ depending on the semiconductor's response to sunlight. The use of silicon in solar panels is advantageous since silicon does not contain toxic materials and is easily available due to large silicon reserves on Earth. These advantages make silicon the most preferred semiconductor material in PV panels.

With the advancements in technology, new materials have also been used on PV panels. According to the studies carried out in recent years, the efficiency of the new generation PV cells has increased depending on the new materials used.

2.1.2.1. Crystalline PV cells

Silicon, which is used in the internal structure of this type of cell, is the second most abundant element on Earth. Consequently, the production of Crystalline PV Cells has a lower cost than other PV cell types. There are two different cell types, depending on the production method.

One of these cell types is Monocrystalline Silicon (mono c-Si). This cell provides high efficiency under technically suitable radiation conditions. Silicon, which is the internal building material of these cells, has a homogeneous structure, and the properties of silicon are seen in the cells for a long time. As a consequence of these features, it is observed that it has higher efficiency when compared to different cells. Market product efficiency is 19-21%. The production phase of these cells includes high heat and chemical applications. The reason for this is that a high-rate purification process is applied during production for the formation of silicon ingots. However, due to material losses during the production phase, its production is costly.

Another type of Crystalline PV cell is Polycrystalline Silicon (Poly-Si). Although the production of this cell type is easy and lower cost compared to Monocrystalline

Silicon, it has 11-15% lower efficiency than Monocrystalline Silicon. The actual efficiency of these PV cells after production is 16-19%.

2.1.2.2. Gallium Arsenide cells (GaAs)

The production of this cell is accomplished via the usage of gallium (Ga) and arsenic (As) compound semiconductors. It performs well in terms of efficiency when compared to silicon-based cells. In addition, these cells also have an advantage when compared in terms of weight. However, it has higher heat tolerance than other cells in its class. Although they have a value of 26% in terms of efficiency, they are expensive.

2.1.2.3. Thin film PV cells

Due to the long-striped structure of thin-film PV cells, material loss in Monocrystalline Silicon cells is prevented. As a consequence of these material savings, they can be produced more cheaply. Despite many advantages such as high efficiency, thin strip films could not be developed due to stability problems in long-term use. The basic building materials of these cells are amorphous silicon, cadmium telluride, and copper indium-diselenide.

If we start with the first essential building materials, an Amorphous Silicon (A-Si) solar cell has been produced by making use of the Silane (SiH_4) gas plasma-assisted chemical precipitation technique. The expected efficiency of this solar cell decreases when exposed to sunlight. Under normal conditions, it has a low efficiency of 6-8% compared to other types (Lynn, 2010). However, it is a highly preferred type among small-sized solar cells. After using these cells, the use of direct bandgap materials begins. As a ramification, a cheaper system has been developed. Moreover, providing a solid performance boost, their development has also been accelerated.

Cadmium Telluride (CdTe) solar cells were produced by combining another type of solar cell, Cadmium element, and tellurium element. Unlike amorphous silicon solar cells, although the laboratory efficiency is above 21%, it cannot meet the expectations in terms of module efficiency. Still, it can be used in large surface area production.

Another technique used in solar cell research is as follows: Copper indium diselenide (CIS) solar cells are produced using the evaporation technique of copper, indium, and selenium materials. The appearance of these cells is homogeneous.

Table 2.1 compares various solar cell technologies from 4 different manufacturers in terms of cell efficiency and power density. The advantages and disadvantages of the solar cell technologies in the table can be evaluated according to their usage areas, and the most suitable one can be preferred.

Table 2.1. *The market research of solar cells technologies (Nikoderm and Biering, 2020)*

Technology	Manufacturing Company	Cell Efficiency	Power Density	Advantages	Disadvantages
Monocrystalline silicon cells	SunPower	up to 23%	about 0.50 Wp/g	Relatively cheap	Low power density
Copper-Indium Gallium Diselenide (CIGS)	Flisom; Ascent Solar	up to 15%	about 0.65 Wp/g	Attractively priced Relatively easy to integrate	A lot of space required degradation under moisture
Single Junction Gallium Arsenide	AltaDevices (bis 2019)	up to 25%	about 1.20 Wp/g	High power density Relatively cheap	Currently no suitable manufacturer
Triple junction based on Gallium Arsenide	MicroLink; Azur Space; SolAero	up to 32%	about 1.40 Wp/g	High power density	Very expensive

2.2. DC-DC Converters

DC-DC converters are a power transformer that raises or lowers the DC voltage level obtained by solar energy in the system, depending on the source to which the power will be transferred (Hart, 2011). The basic working logic of this converter is based on the duty cycle. The input voltage is converted to a different output voltage by duty cycle (D). The variation in the magnitude of this voltage is based on the type of dc-dc converter used. The input voltage in the system can decrease or increase according to the desired output voltage. The DC-DC converter needs to store the input voltage to change voltage. This electric field storage function is realized with the help of a capacitor. As a result of the magnetic field feature in the transformer, electrical energy is stored in the dc-dc converter.

The regulation of the output power according to the input power is made through the duty cycle. Thus, the duty cycle can control the output voltage and current and provide constant power output. Converters vary in their characteristics, such as the complexity of their structures or the amount of costs. Therefore, it is necessary to pay attention to these features during the use of this electronic equipment in the circuit.

Although there are many types of this converter according to the places of use, the most used types are:

- Buck Converter
- Boost Converter
- Buck-Boost Converter

2.2.1. PWM (Pulse Width Modulation)

PWM (Pulse Width Modulation) is built into the DC-DC converter. This solar charge controller is located in the connection between the PV panels and the battery. Thus, it allows for controlling the output power of the DC-DC converter and the battery charging current. PWM uses a 'rapid switch' during this operation. This rapid switch is located between the power supply and the load. This switch works on the principle of opening and closing hundreds of times per second. According to this, initially, it stays on until the battery's absorption charge voltage limit. It then maintains the battery voltage at a constant value by adjusting the current to the appropriate value. In this way, the voltage and current transmitted by the load can be adjusted.

2.2.2. Duty cycle

Duty cycle is a term expressed as the ratio of the time a circuit is open to the time it is closed. This expression is used as a percentage. If pulse occurs in different time stamps duty cycle varies with it. Pulse width modulation allows precise control of the power supplied to the battery. The voltage average is determined in each duty cycle according to the open pulse duration. If the duty cycle is associated with power, the duty cycle with a high ratio corresponds to high power. As the reason for this, it can be deduced that the high-rate duty cycle system remains off for a longer period of time compared to the open state. Thus, the relationship between power and the duty cycle can be understood.

As seen in Figure 2.2, the signal wave of the duty cycle is a digital wave. It can be seen that this square wave spends half of its operating time on. Therefore, the wave in the image can be interpreted as a 50% duty cycle. In Figure 2.3, which represents a lower power, a 75% duty cycle is seen. For this figure, it can be interpreted that it is active ¾ of the time while running and it is turned off ¼ of time.

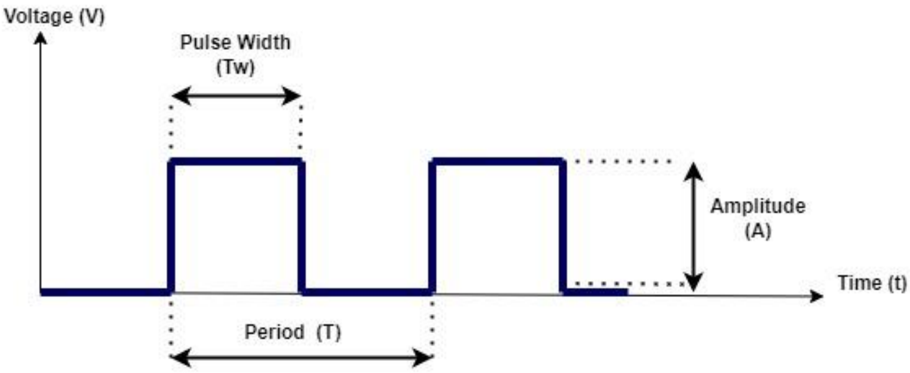

Figure 2.2. *Duty cycle (50%)*

The ratio of the period of a square signal to the pulse width and the calculation of the duty cycle is given in Equation 2.1.

$$\text{Duty Cycle} = \frac{\text{Tw}}{T} \times 100\ \% \tag{2.1}$$

Here, Tw is a pulse width time, and T is a period.

In Figure 2.3, there is a square wave with a wider pulse.

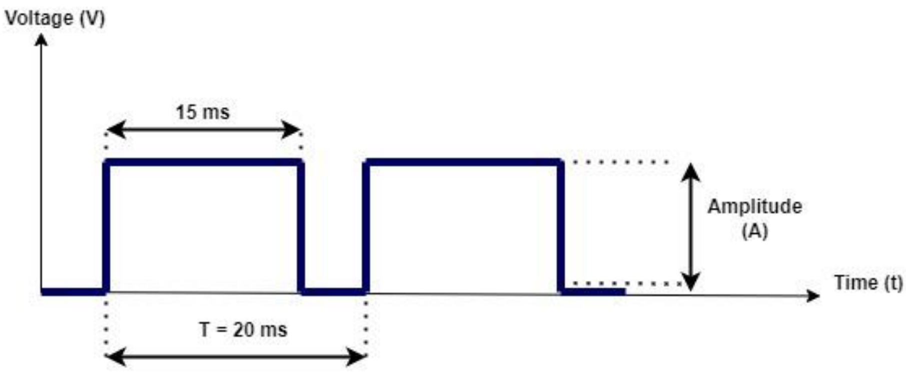

Figure 2.3. *Duty cycle (75%)*

Duty cycle calculation in Equation 2.2 was made by using the frequency formula in Equation 2.1.

$$\text{f} = \frac{1}{T} = \frac{1}{20\text{ ms}} = 200\ Hz \tag{2.2}$$

$$\text{Duty Cycle} = \frac{\text{Tw}}{\text{T}} \times 100\ \% = \frac{15}{20} \times 100\ \%$$

$$\text{Duty Cycle} = 75\ \%$$

2.2.3. Variation of DC-DC converters

In order to the PV arrays on the UAV to operate at optimum efficiency, a system is established in which the power obtained from the PV panels can be transmitted to the battery at the maximum value (Shiau et al., 2009). This forwarding can be done in the DC-DC converter. During the flight, the output power of the PV panels changes as the flight conditions change. Even if the input power of the DC-DC converter is variable, the power to feed the battery must be transmitted at a constant value. Even if the PV output power is variable, the charging current delivered to the battery must be transmitted at a constant value in order to prolong the battery's lifetime. Several configuration variations have occurred within the system in this power transmission phase, depending on the feature expected from the converter (Abouelela, 2020). This yields to another type of converter.

2.2.3.1. Buck converter

The first of these converter types is the step-down Buck DC-DC converters, which reduce the voltage from solar panels (Taghvaee et al., 2013). The buck converter reduces the DC voltage at its input to a lower DC voltage level and transfers it to its output. It is used to obtain output voltages such as 5, 12, 24, 48, 110, 220V from 12, 24, 48, 110, 220, 400V input voltages.

The basic Buck converter circuit design is shown in Figure 2.4. Circuit design includes a diode, a switch, an inductor, and capacitors. A low pass filter is created with the inductor and capacitor in the circuit. Its operating principle changes depending on whether the circuit is open or closed. According to Pulse Width Modulation (PWM), the switching element is switched on and off. The period that occurs when the signal is on is called the duty cycle of the signal (Rashid, 2017). The duty cycle varies depending on the open time of the switch. In the off state, the current is expected to pass through the inductance (L). The inductor changes the voltage instantly so that the current can be kept constant within itself. When the switch is closed, due to the magnetic field created in the inductor during the current flowing over it, equal and opposite voltage to the battery is formed, and resistance to this flow occurs.

Meanwhile, electrical energy is stored in the magnetic field of the inductor. This process continues until the magnetic field reaches a constant level. After magnetic field stabilization, the maximum current flowing makes the circuit closed. After the current passes, the switch in the circuit turns on. When the switching element in the circuit is conducting, the diode becomes an insulator, and the energy stored in the inductance is used. The circuit continues to flow through L until the switch is in the closed position.

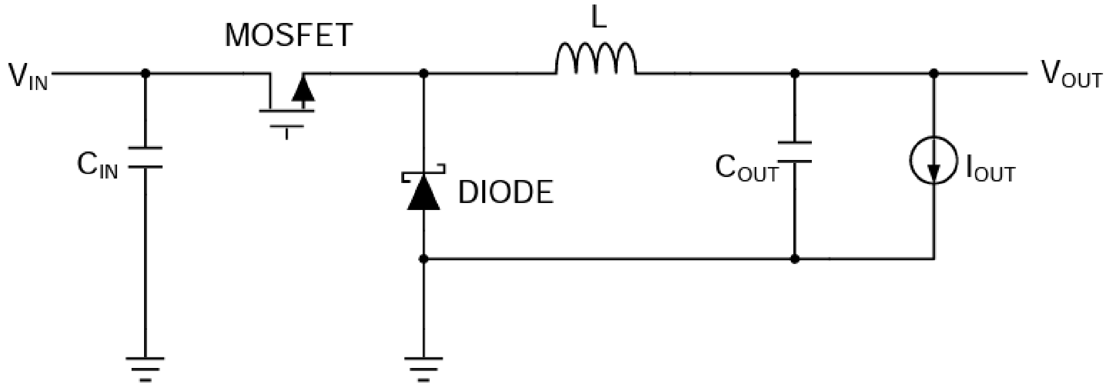

Figure 2.4. *The circuit design of the basic Buck converter (De Stasi, F., 2015)*

The current in the circuit varies according to the position of the switch in the buck converter circuit. Various formulas are needed to perform calculations according to the flow in the circuit. The mathematical calculation of the power conversion in the Buck converter consists of the following Equations (Baharudin et al., 2018). Calculations in reducing the output voltage with a buck converter are made depending on the input voltage and duty cycle values. When the switch is on, the voltage provided by the inductance while it is on, and the voltage provided during the time it is closed should be equal to each other. Equation of duty cycle calculation is included in Equation 2.3.

$$D = \frac{V_o}{V_i} \tag{2.3}$$

Here, V_o is the output voltage, and V_i is the input voltage.

Equation 2.4 is used to calculate the minimum inductance value while selecting the inductor in the buck converter circuit to be created. The point to be considered in this Equation is the frequency selection. To prevent the deterioration of electronic components, the value of the operating frequency that the inductor can support should be selected.

$$L_{min} = \frac{(1-D)R}{2f} \tag{2.4}$$

Here, D is the duty cycle value, R is the load connected to the circuit, f is the inductor operating frequency and the minimum value of the inductor.

Equation 2.5 is used to calculate the inductor value in the circuit. The calculation process in this Equation depends on Equation 2.4. The inductor value is reached using the L_{min} value calculated in Equation 2.4.

$$L = k\, L_{min} \tag{2.5}$$

Here, the inductor ratio required for uninterrupted operation of the k converter is the minimum value of the inductor, and L is the inductor value used in the circuit. The k in the equation is determined by how much less than L its value should be in percent. $\frac{L}{L_{min}}$ can be considered as the k coefficient.

Using Equation 2.6, the inductor current is calculated.

$$I_L = \frac{V_o}{R} \tag{2.6}$$

Here, Vo is the output voltage, R is the load connected to the circuit, and I_L is the inductor current.

As long as the current value is positive, the current is considered to be continuous. Equation 2.7 and Equation 2.8 are used to calculate the maximum (I_{max}) and minimum values (I_{min}) of the inductor current by using the calculated I_L value.

$$I_{max} = I_L + \frac{\Delta i_L}{2} \tag{2.7}$$

$$I_{min} = I_L - \frac{\Delta i_L}{2} \tag{2.8}$$

Here, I_L is the inductor current, Δi_L is the difference between the inductor current waves, I_{max} is the maximum value of the inductor current, and I_{min} is the minimum value of the inductor current.

Finally, the capacitor (C) value can be calculated using Equation 2.9. The output ripple voltage is used to calculate the capacitor value. Part of the output voltage creates the ripple output voltage and is calculated using Equation 2.9.

$$C = \frac{1-D}{8L(\frac{\Delta V_o}{V_o})f^2} \tag{2.9}$$

Here, D is the duty cycle, L is the inductor current, ΔV_o is the peak-to-peak value of the output voltage signal, V_o is the DC output voltage of the circuit, f is the inductor frequency, and C is the capacitor value.

The waveforms of the signals formed on the elements in the circuit are also given in Figure 2.5.

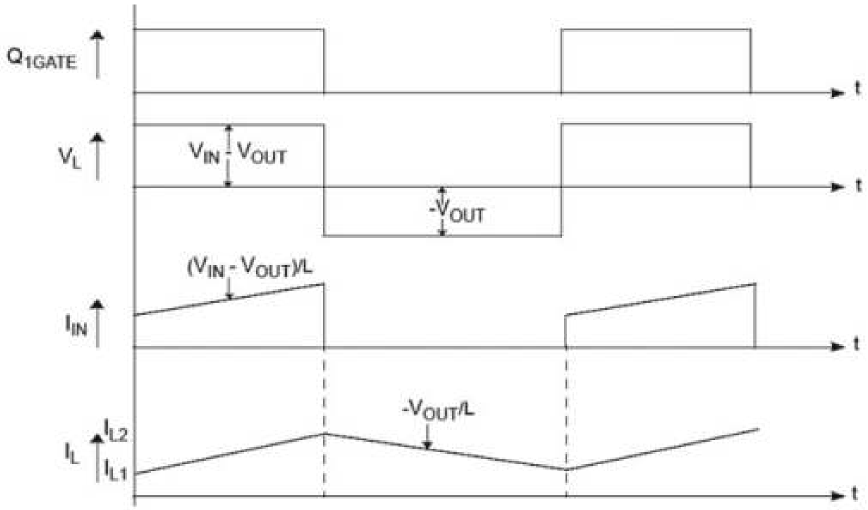

Figure 2.5. *The circuit waves of the basic Buck converter (Abouelela, M., 2020)*

Here, the waves represent the gate pulse, inductor voltage, input current and inductor current of the switching element, respectively.

2.2.3.2. Boost converter

The second type of DC-DC converter is the Boost DC-DC converters, which are used to increase the voltage applied to its input. The boost converter is the most well-known and simple-structured development booster circuit that converts a voltage to a higher voltage. These converters are sometimes called Step-up Converters. It is necessary to regulate the power from PV panels for batteries (Barreto et al., 2014). The boost converter tries to balance the current by taking advantage of the magnetic field property of the inductor. Changes in the inductor's magnetic field regulate the changes that may occur in the current flowing in the circuit. By doing so, it ensures that the output voltage is higher than the input voltage. It is used to obtain output voltages such as 12, 24, 48, 110 220, 400V from 5, 12, 24, 48, 110, 220V input voltages used in the circuit.

A basic boost converter contains a diode, a switch, an inductor, and capacitors., as seen in Figure 2.6.

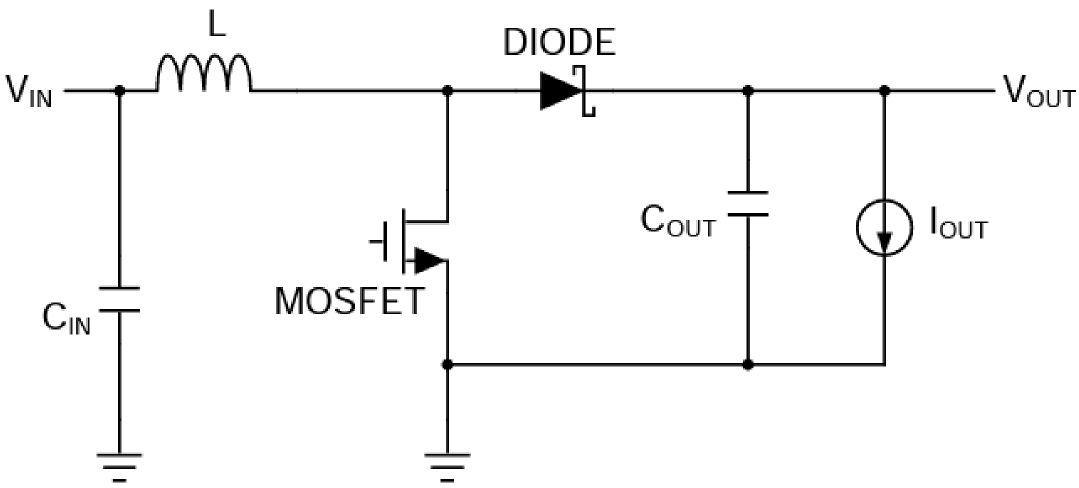

Figure 2.6. *The circuit design of the basic Boost converter (De Stasi, F., 2015)*

As the operating principle of the boost converter, it can be said that it is based on the operation of the circuit elements by changing the direction of the current according to the switching in the circuit. Thus, the expected operation from the circuit is carried out. When the switch in this converter circuit is closed, the current comes from the source and flows over the coil and the switching element, and thus energy is stored in the coil. When the switch is open, the current completes the circuit through the diode and capacitor instead of completing the circuit through the switching element.

When the switch is closed, the coil transfers the energy stored on it to the capacitor and the load via the diode. The capacitor charges when the switch is open and discharges when the switch is closed. If the circuit's switching process is done very fast, the coil cannot wholly discharge its energy during charging and discharging, and it always remains loaded. In this way, the energy of the source and coil is loaded onto the capacitor. The load is fed from the capacitor when the switch is closed and from the source and coil when it is open. Thus, a low-level DC voltage becomes a higher-level DC voltage.

To make the component selection in the boost converter circuit in the most efficient figure according to the desired voltage and current, a couple of equations must be used. First of all, the input and output voltage and the frequency at which it is expected to operate must be determined. Afterward, the required duty cycle is calculated. Equation 2.10 is used to calculate the duty cycle.

$$D = 1 - \frac{V_i}{V_o} \tag{2.10}$$

Here, V_i is the input voltage of the circuit, V_o is the output voltage of the circuit, and D is the duty cycle. After the duty cycle is found, the inductance value is calculated using this value. Equation 2.11 is used to calculate the minimum value of the coil. With this Equation, the minimum value for the circuit is found.

$$L_{min} = \frac{D(1-D)^2R}{2f} \tag{2.11}$$

Whereas; D is the duty cycle, R is the load connected to the circuit, f is the frequency value to be applied in the circuit, and L_{min} is the minimum value of the coil. The maximum current that can pass through the coil is given by Equation 2.12.

$$I_L = \frac{V_i}{(1-D)^2R} \tag{2.12}$$

Here, V_i is the input voltage of the circuit, D is the duty cycle, R is the load of the circuit, and I_L is the current passing through the coil. Equation 2.13 is used for calculating the capacitor value.

$$C \geq \frac{D}{\frac{\Delta V_0}{V_0} f R} \tag{2.13}$$

In which; D is the duty cycle, ΔV_0 is the peak-to-peak value of the voltage signal, V_0 is the DC voltage of the circuit, f is the frequency of the circuit, R is the load of the circuit, and C is the capacitor in the circuit.

The capacitor value in the Equation 2.13. must be greater than or equal to the result of this equation. The value in this equation represents the ripple rate. Another name for the ripple rate is the ripple factor. Ripple rate can be explained in the following Figure 2.7, in DC voltages, the waveform is expected to be close to flat, so it is desired that the upper and lower values of the wave formed, that is, the value from peak to peak, be small. The peak-to-peak value of the voltage is called the peak-to-peak voltage. These Equations are used when designing the Boost converter. While designing a Boost converter circuit, the operating frequency is determined by specific forms of utilization. To conclude, the coil value becomes smaller if the frequency increases.

The waveforms formed in the circuit components of this converter are shown in Figure 2.7.

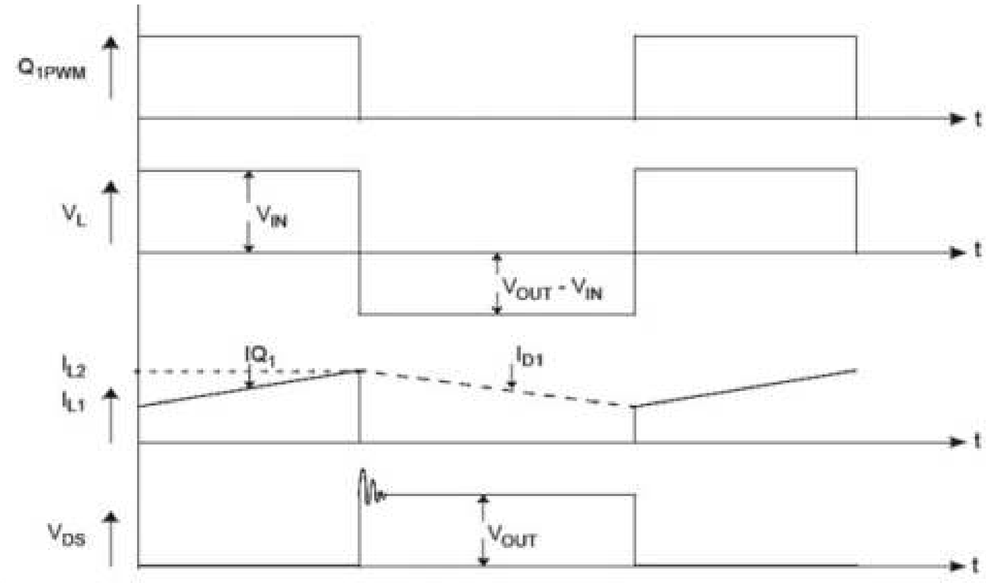

Figure 2.7. *The circuit waves of the Boost converter (Abouelela, M. 2020)*

In this figure, the waves indicate the gate pulse of the switching element, the inductor voltage, the current between the switching element and the diode, and the voltage forms in the switching element, respectively.

2.2.3.3. Buck – Boost converter

The Buck converter, known as the step-down converter, and the boost converter, known as the booster, were combined to form the Buck-Boost converter. Thus, the Buck-Boost converter has a circuit that can set the output voltage higher or lower than the input voltage. It either increases or decreases the voltage according to the system it is acting on. The buck-Boost converter circuit is in Figure 2.8.

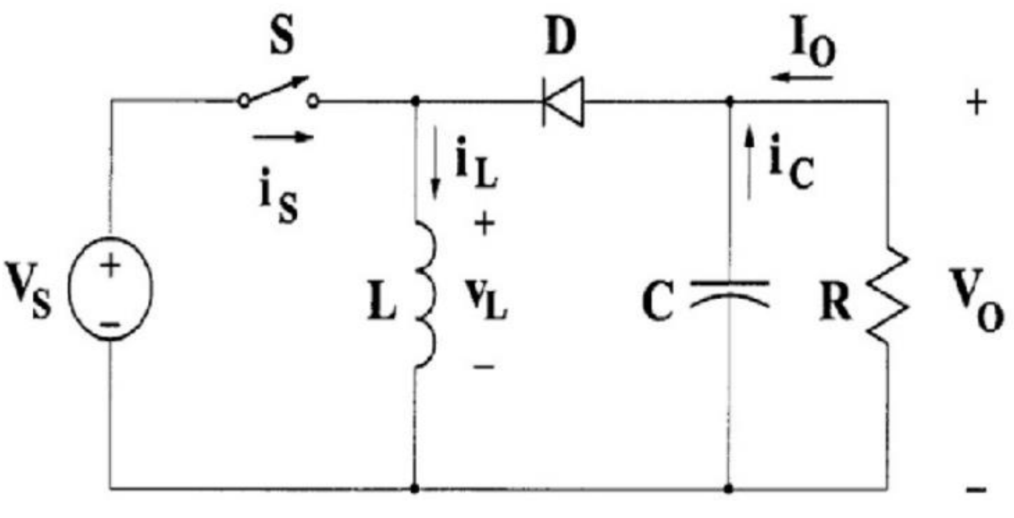

Figure 2.8. *Basic view of the Buck-Boost converter circuit (Bhattacharjee and Saharia, 2014)*

It is made of a switch, a diode, an output capacitor, and an inductor. There is a power supply in the circuit. The diode is in the circuit opposite to the current flow in the circuit. This diode is connected in reverse bias to the current from the inductor and forward biased to the current from the capacitor. Pulse Width Modulation (PWM) pulses activate the switch that is connected to the circuit. After receiving these pulses, the switch is either opened or closed. The position of the switch determines the output voltage. The output voltage of the circuit is formed with reverse polarity. In other words, if the input voltage is negative, the output voltage is positive.

The formula of the output voltage is given like this.

$$V_O = \frac{-V_i D}{1-D} \tag{2.14}$$

In this equation, V_i is the input voltage, D is the duty cycle, and V_O is the output voltage. Since it is known that the output voltage has negative polarity, there is a negative sign in the formula to make its value positive.

The working principle of the buck-boost converter depends on the resistance to rapid changes in current. This converter is evaluated in two figures as operating mode.

The first of these two modes is the mode in which the switch in Figure 2.9 is closed and conductive. In this case, since the diode, which is one of the other components in the circuit, is in a closed state, it does not allow the current to flow in the direction of the circuit flow and plays the role of an insulator. Therefore, the inductor has zero resistance, and current flows through the switch and inductor and back. But while the current is flowing, the inductor does not allow sudden changes in this flow by resisting, and this resistance will lower the input voltage. This causes the current to remain at low levels. This situation continues until the moment when the inductor reduces the obstacle in the current flow. Thus, the voltage drop across the inductor also decreases. This provides energy storage in the inductor, and no current flow is observed in the load.

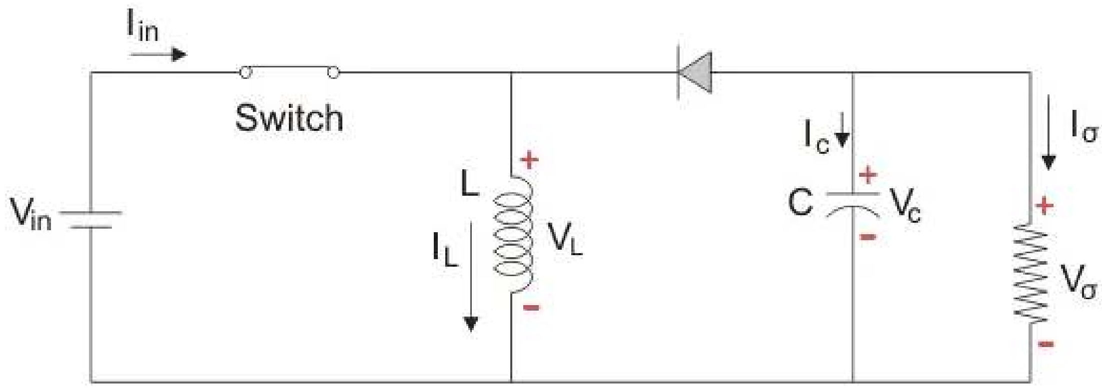

Figure 2.9. *View of the circuit when the switch is closed*

Another mode is the mode in which the switch in Figure 2.9 is closed, and its transmission is cut off. Since the switch is closed in this mode, the sudden drop in current causes the return voltage to be induced in the inductor.

$$V = L\frac{dI}{dt} \tag{2.15}$$

Here, L is the inductance of the inductor, $\frac{dI}{dt}$ is the change in current over time, and V is the voltage generated in the inductor.

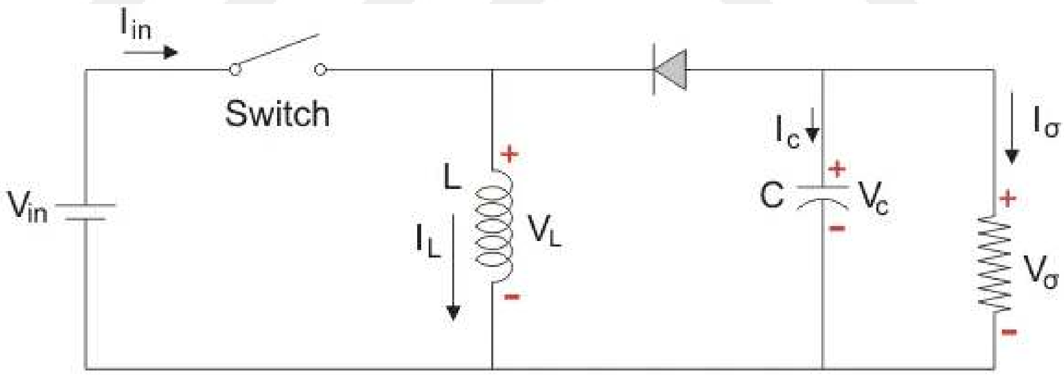

Figure 2.10. *View of the circuit when the switch is opened*

After the switch is opened, the polarity of the inductor is reversed. Current in the circuit is a closed-loop and flows through the load and diode. So, the current through the inductor continues to flow in the same direction. The diode is conducting and makes the output voltage flow in the opposite direction. In this case, the fluctuations formed by the capacitor in the circuit are filtered.

Changes in the states of the components in the circuit also cause changes in the current and voltage values on the components. Some basic formulas are needed to calculate values on circuit elements. The mode of the circuit should be taken into account when applying these formulas.

The open or closed state of the switch in the phase constitutes the basic working principle of the circuit. Therefore, the calculation of the switching frequency here is fundamentally important. The equation required for the calculation is in Equation 2.16.

$$f = \frac{1}{T} \tag{2.16}$$

Here, T is the operating period of the converter, and f is the switching frequency.

The equation of the Buck-Boost converter, which is created depending on the open time of the switch in duty cycle calculation, is seen in Equation 2.17.

$$D = \frac{T_{on}}{T} \tag{2.17}$$

Whereas; T_{on} is the duration the switch is open, T is the total operating time of the circuit, and D is the duty cycle.

In addition, in the Buck-Boost converter circuit, the inductor voltage and the input voltage are equal, and the inductor current, which flows steadily when the switch is open in the circuit, primarily shows a positive slope. In this case, the inductor current rises to its maximum value. Afterward, the slope becomes negative and decreases towards the starting point. As a result, the net change in the inductor current does not occur. In line with this information and assumptions, the calculations in Equation 2.18 were made while the switch was in the open position.

$$\begin{gathered} V_i = V_L \\ V_L = L\frac{dI_L}{dt} = V_i \\ \frac{dI_L}{dt} = \frac{\Delta I_L}{\Delta t} = \frac{\Delta I_L}{\mathrm{DT}} = \frac{V_i}{L} \\ (\Delta I_L)_{off} = \frac{V_i}{L} DT \end{gathered} \tag{2.18}$$

Here, V_i is the input voltage, V_L is the inductor voltage, L is the inductor inductance, $\frac{dI_L}{dt}$ is the change in the inductor current over time, ΔI_L is the change in the inductor current, D is the duty cycle, T is the period of the circuit, and $(\Delta I_L)_{off}$ is the change in the inductor current when the switch in the circuit is closed.

In the Buck-Boost converter circuit, when the switch is closed, the inductor voltage is equal to the output voltage and the inductor current, which flows steadily, has a positive slope in the beginning. Also, in this case, the net change in the inductor current is zero. However, if the switch in the circuit is closed, the equations in Equation 2.19 are accepted.

$$V_L = V_o$$
$$V_L = L\,\frac{dI_L}{dt} = V_o$$
$$T_{off} = T - T_{on} = T - DT = (1-D)T$$
$$\Delta t = (1-D)T$$
$$\frac{dI_L}{dt} = \frac{\Delta I_L}{\Delta t} = \frac{\Delta I_L}{(1-\mathrm{D})T} = \frac{V_o}{L}$$
$$(\Delta I_L)_{on} = \frac{V_o}{L}\,(1-D)\,T \tag{2.19}$$

In which, V_L is the inductor voltage, V_o is the output voltage, L is the inductor inductance, $\frac{dI_L}{dt}$ is the change of the inductor current over time, ΔI_L is the change in the inductor current, D is the duty cycle, T is the period of the circuit and $(\Delta I_L)_{on}$ is the change in the inductor current when the switch is in the open position.

The change in inductor current with the switch in the open position is opposite and equal to the inductor current when the switch is in the closed position, and the ratio of output and input voltages is given in Equation 2.20.

$$(\Delta I_L)_{off} + (\Delta I_L)_{on} = 0$$
$$\frac{V_i}{L}\,DT + \frac{V_o}{L}\,(1-D)T = 0$$
$$\frac{V_o}{V_i} = \frac{-D}{1-D} \tag{2.20}$$

Here; $(\Delta I_L)_{off}$ is the change in the inductor current when the switch is closed in the circuit, $(\Delta I_L)_{on}$ is the change in the inductor current when the switch is in the open position, V_i is the input voltage, V_i is the output voltage, L is the inductor inductance, D is the duty cycle, and T is the period of the circuit.

In the Buck-Boost converter circuit, a change in the voltage of the circuit is observed depending on whether the position of the switch is open or closed. Through this switching, the duty cycle value of the circuit changes between 0 and 1. If the duty cycle is greater than 0.5, the output voltage will be greater than the input value, but if the duty cycle is less than 0.5, the output values are smaller than the input. And if the duty cycle is 0.5, it means that the input and output values are equal. If the output voltage is greater than the input voltage, it acts as a boost converter. In this situation, it is seen that the input current value is greater than the output current. Otherwise, if the output voltage is less than the input voltage, it will act like a buck converter, and the input voltage will be less than the output voltage.

2.2.3.4. Other converter types

The types of buck converter, boost converter, and buck-boost converter, which are mostly used as DC-DC converters, are mentioned. Apart from these mentioned converters, there are many different converters that serve different tasks. These various converter types are as follows;

The operational structure of Forward Converters is based on the basic buck converter topology. More flexibility is made available for the control stage when proportioning the output voltage of this converter to the input voltage. It also uses a transformer between the load in the circuit and the input source. In this way, it isolates the load from the circuit.

On the other hand, Flyback Converter (FBT) is similar to Forward Converter in terms of its basic working structure, although it has some differences. This type of converter is different from FC; the secondary output is out of phase for this converter. The transformer in the circuit functions the same as the inductor, so there is no need to add an inductor to the circuit.

The method of operation of the push-pull converter is based on the simple forward converter. This converter circuit is isolated from transformers. The task of the transformer in the circuit is to reduce the voltage. Moreover, isolation is provided between the input and the output.

In the Half-Bridge Converter, unlike the others, only a center-tipped transformer is used in the secondary winding in the circuit design. It is named this way because of the difference in connecting the elements in the circuit and therefore the voltage being applied in a different way.

A high frequency switching element is used in the Half-Bridge Resonant Converter circuit. Thus, the volume of the passive components and the transducer size are generally reduced. But increasing the speed of the switch causes power losses. The efficiency of the high-frequency switch in the circuit drops.

Series Resonant Converter (SRC) is connected to the primary ends of the transformer in the circuit. This causes the primary current to have a sinusoidal structure. Thus, the current passing through the switching phase is reduced to low values, and the switching losses are minimized.

There is a resonant circuit in the Parallel Resonant Converter (PRC) circuit. This resonant circuit is connected to the transformer in parallel in the circuit. The resonant frequency of the circuit is lower than the switching frequency. The switching frequency varies in direct proportion to the load. When the circuit is operated under high input voltage, it causes high energy consumption and a high turn-off current in the circuit. Therefore, a parallel resonance converter is not suitable for a front-end DC/DC converter.

The LLC Resonant Converter circuit uses a primary transformer, an inductor, and a capacitor. Depending on the circuit design, the inductor and capacitor can be connected in series or parallel with the transformer. In this converter design, the switching frequency is higher than the resonant frequency of the circuit. A lighter load can be used with this converter, and the frequency range can be lowered even when there is no load if the voltage switching is zero. Equipped with mentioned features, this converter is the most suitable choice for front-end DC/DC applications by providing direct current gain.

2.3. Battery Technologies

Today since electric vehicles are trending, the issue of energy storage in aircraft has become an important issue (Barreto et al., 2014). Energy storage units play a critical role in meeting the electricity needs of the avionics on the aircraft (Chen and Khaligh., 2010). Although it is possible to store electrical energy using different technologies such as capacitors and hydrogen in aviation applications, the most commonly used one of these technologies is batteries (Luo et al., 2015).

Since chemical substances are used in batteries, electrical energy must be converted into chemical energy. In doing so, electrical energy can be stored in batteries as chemical energy properly. Afterward, depending on where the batteries are used, the chemical energy stored in them can be recycled into electrical energy and used to meet the required power. The capacity of a battery determines the total amount of energy that can be stored in it, and this capacity value is defined in ampere-hours (Ah). The stored energy is directly proportional to the battery capacity. 1 Ah is considered equal to 3600 coulombs of charge.

The capacity of 1 Ah implies that it can provide 1 A or 1 coulomb/sec of energy continuously for 1 hour. Depending on the number of electrodes in the designed battery and the type of electrolyte, its capacity increases in direct proportion. For this reason, batteries with the same voltage but differing in volume also vary in size and capacity. Since the power obtained from the batteries is produced depending on the chemical reactions that take place inside, they are affected by environmental factors such as the lifetime of the cells, current size, current duration, and temperature. Batteries are classified in terms of their properties. The current provided by the battery with a certain capacity and the amount of time it can provide the current can be determined. Depending on the amount of current supplied by the battery, the discharge rate is the main factor in the efficiency. In other words, the efficiency varies depending on the discharge rate of the battery. The discharge rate and efficiency of the battery are inversely affected by each other. For example, a decrease in discharge rate increases the efficiency of the battery.

As seen in Figure 2.11, battery cells contain a metal anode that acts as a negative electrode, a metal oxide cation that acts as a positive electrode, and an electrolyte.

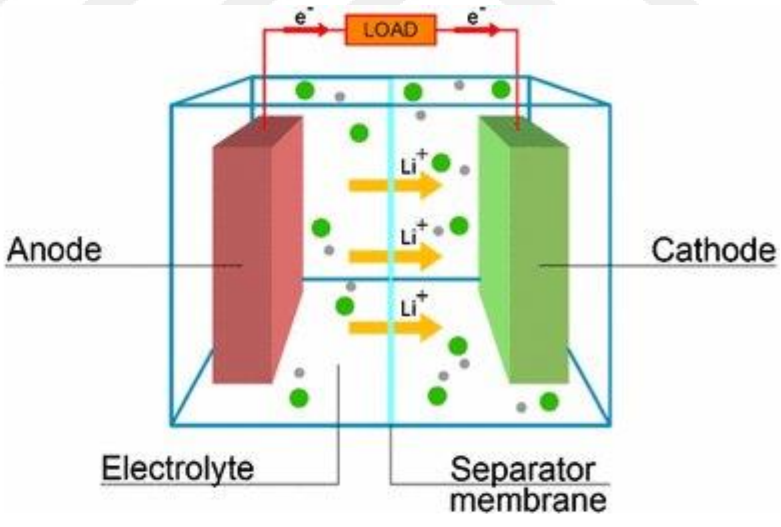

Figure 2.11. *Basic view of a battery cell (Grazioli, 2016)*

The electrolyte between the electrodes of the battery cell allows the chemical reaction to occur in the cell. While corrosion is observed at the anode of the cell during the chemical reaction, an electrical current is generated at the cathode as a result of the ionization reaction. Enabled by this chemical event in the battery cell, the battery, which is the primary power source for many devices, provides electrical energy. After this electrical energy is obtained from a cell, different results can be obtained by providing various connections of several cells with each other. For example, if the positive (+) pole of one of the battery cells and the negative pole (-) of the other cell are brought together to form a series connection with each other, the voltage of the battery increases. With this serial connection, theoretically, the life of the battery is fixed. If the positive poles of the battery cells are to be connected to each other, and the negative poles of the battery cells are to be connected to each other, the cells are considered to be connected in parallel. This parallel connection stabilizes the battery voltage. In addition, the life of the battery is extended as much as the number of cells used in this circuit.

Although studies on and research of battery technology have been suspended for a certain period, the importance of batteries has jumped to the forefront again after an airplane accident in 2013, and battery technology has been linked to rapid development. (National Transportation Safety Board, 2013; Willard et al., 2013). However, with the development of electric aircraft, the use of batteries has increased and has gained critical importance in these vehicles.

The purpose of using batteries in aircraft is as follows;

- Balancing the sudden loads on the electrical system
- To provide the necessary power for the operation of the system and the engine
- Providing energy in case of emergency

Batteries are divided into numerous types regarding their intended use. Participation of the aircraft in specific missions demands that the most suitable one is selected from these different types of batteries. Since the requirements of many aircraft such as satellites, passenger and military aircraft, and UAVs differ, the battery used in each must be carefully selected. If an assessment is made only for aircraft, then even factors such as the altitude at which the aircraft will cruise, the electrical power required by the aircraft's avionics, and the type of mission are reasons for using different battery types in aircraft (Yildiz and Karakoc, 2017). Some parameters for battery selection to be used in aircraft can be listed as follows (Howey and Alavi, 2015);

- Energy density
- Cycle life
- Instant and continuous power required

- Operating life
- Thickness
- Environmental conditions
- Cost

2.3.1. Background of batteries

The history of the batteries that we frequently use today dates back to the ancient Egyptians. Some evidence of electricity has been found in artifacts from ancient Egypt. Although there are no official records, it is thought to be an ancient electricity storage system. The first battery, officially discovered in 1938, is known as the Baghdad battery. A pot-like battery made of yellow clay was found in the Khujut Rabu region, as shown in Image 2.1. (Von Handorf, 2002). The Baghdad battery is made of clay, has an oval shape, and is 13.5 cm long. Copper layer, iron rod, asphalt, and acidic liquid such as wine were found in the internal structure of the battery.

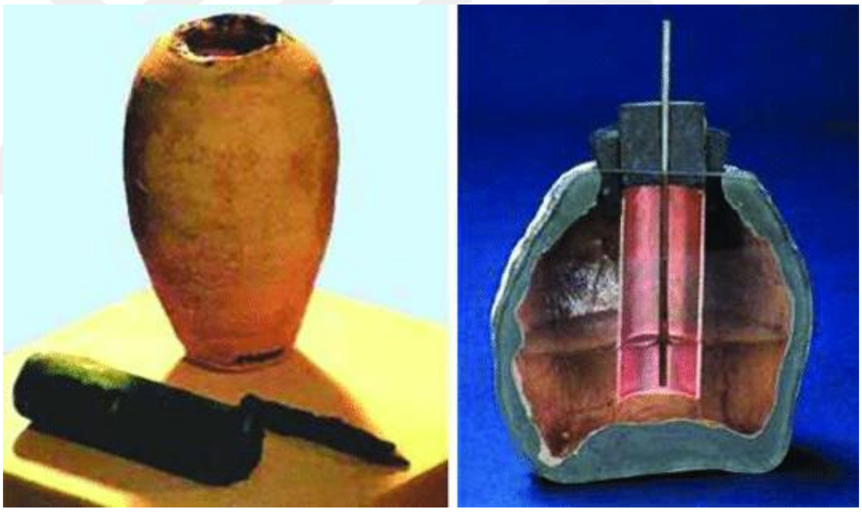

Image 2.1. *External and internal view of The Baghtat Battery (AlShemmary et al., 2013)*

With the studies on this evidence, it is known that the existence of batteries dates back to the end of the 18th century. With the experiments of Luigi Galvani on animals, studies on the battery started. At the end of these experimental studies, he reached a finding called 'metallic electricity' and published the results he obtained from the experiments in 1791, becoming a pioneer for new studies. These studies formed the basis of research for Alessandro Volta.

In 1795, experiments began to be carried out on materials, not animals. Volta proved that electrical current could only be created by placing a damp cloth or fluid between two dissimilar metals. After this, he made his invention in 1799. This invention, named Volta battery or Chain of Containers, is as in Image 2.2.

Image 2.2. *The Volta Battery (Finger et al., 2013)*

In this battery setup, cylindrical cardboards moistened with saltwater are stacked on top of each other (Figure 2.11). Copper-zinc or silver-zinc metals are placed on the top and bottom of the stacked discs.

After this discovery, the number of studies on the subject has been increased, and a more innovative battery was produced by Frederic Daniell in 1836. This battery, called the Daniel battery, consists of two separate parts, as shown in Figure 2.12. The first part contains zinc sulfate ($ZnSO_4$) solution. A zinc rod is dipped in this material. The other part contains copper(II)sulfate (Cu_2SO_4) solution. There is also a copper rod inside it. The two parts were separated from each other with the help of a porous container. A chemical reaction occurs between the positively charged zinc ions moving towards the copper plate and the negatively charged SO_4 ions on the other part. The positive charges of copper(II)sulfate on the other side accumulate around the copper plate. The electrical charges of the ions here are reset. As a result of these reactions, electrical flow occurs. The plates in the experiment consist of the poles of the battery. Daniel's work formed the basis of today's batteries.

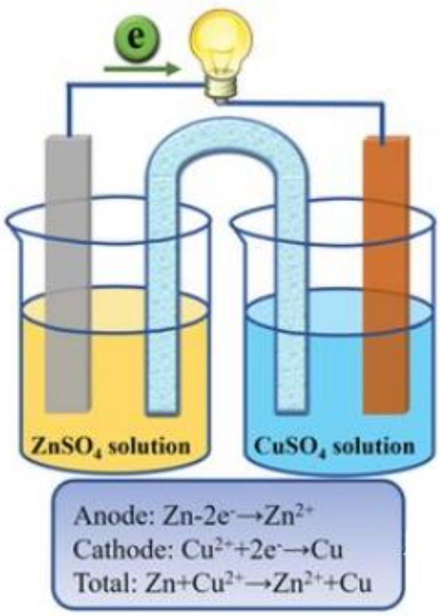

Figure 2.12. *The Daniell Battery test setup (Zhu et al., 2019)*

Afterward, different studies were carried out, and the first fuel cell was invented by William Robert Grove in 1839 by producing constant current and power as a result of the reverse reaction of water electrolysis. In 1859, the first rechargeable battery, the lead/acid battery, was invented by the French physicist Gaston Planté. Georges Leclanché produced the dry cell in 1868. The first nickel-cadmium rechargeable battery was invented by Waldmar Junner in 1899. In 1917, non-rechargeable lithium batteries were theoretically invented by Gilbert Newton Lewis, but their production started approximately 50 years later. Although battery studies were interrupted due to safety problems, Sony launched the first lithium-ion battery on the market. (Kul, 2020).

2.3.2. Types of batteries

Depending on the type of battery cell production, there are two types of batteries: primary and secondary. The main distinguishing feature of primary cell structures must be non-rechargeable. The reason for this is that the chemical structure in the battery cannot be re-reacted. In other words, its chemical structure is not suitable for recharging. Primary cells are considered dead after the initial reaction. These batteries are disposable. In this type of battery, cells can be connected in series to obtain a certain voltage level. The point to be considered in this regard is that these cells should never be connected in parallel. Because in this connection, cells can charge each other. Primary type batteries are also called dry batteries. Examples of these batteries are:

- Carbon/Zinc batteries
- Alkaline Manganese batteries
- Mercury batteries
- Silver oxide batteries
- Lithium manganese dioxide batteries

Another type of batteries are the secondary type batteries. These batteries are also known as storage batteries. The main feature of these batteries is that they can be recharged. The battery is charged by re-powering it by a power source. This process is achieved by reversing the chemical reaction in the battery, and in this way, the battery can provide electrical energy repeatedly after its first use. The battery cells can be connected in series and/or parallel. Thus, the desired voltage and capacity can be obtained from the battery. These batteries have a long life compared to primary-type batteries. Due to this feature, it is possible to come across a secondary battery in today's portable technological devices. In addition, such batteries provide uninterrupted power. With this feature, the endurance of devices using secondary batteries is high. Examples of secondary type batteries can be given as;

- Lead/acid batteries
- Gel (Gel) batteries
- Nickel Cadmium (NiCd)
- Nickel metal hydride batteries (NiMH)
- Lithium-ion batteries (Li-Ion)
- Lithium Polymer batteries (LiPo)

2.3.3. Batteries used in aviation

Although batteries are divided into many types according to their characteristics, some of these types have come to the fore in the aviation industry. Some battery types are more common than others, depending on the mission of the aircraft and the features expected from the battery. Essential batteries for aircraft can be categorized as lead-acid batteries, nickel-based batteries, and lithium batteries. (Tariq et al., 2017).

2.3.3.1. Lead–acid battery

Lead acid batteries were invented in 1859 as the first type of rechargeable battery. It was also the first commercially used battery. (Soloveichik, 2011; Canis, 2013). Although many years have passed since its invention, and it is the most primitive example of rechargeable batteries, its use continues today. The main reason why it has been widely used for such a long time is that it is durable and stands out in price-performance comparison compared to other competitors in the market. These types of batteries are referred to as lead-antimony and lead-calcium. Adding antimony and calcium causes a decrease in battery performance, and other materials are added to reduce this effect. According to the place of use, there are two types: open type lead/acid battery and closed type lead/acid battery.

Lead-acid batteries are heavier compared to other battery types. In addition, it is seen that the battery is more unstable if it is completely discharged. Lead-acid batteries should be kept charged to prevent deterioration. This battery can be charged and discharged cyclically, but the capacity decreases with each charge cycle. Although this situation is seen at a minimum level under suitable operating conditions, the decrease in capacity accelerates after a certain number of cycles. The battery has no memory effect, and the battery life is moderate. Compared to Ni-Cd batteries, less capacity loss is observed in a certain period of time. Lead-acid batteries have good operating performance in cold ambient conditions without a high degradation of internal chemistry.

Lead-acid batteries are charged by applying constant current and constant voltage. These batteries have a 3-stage charging mode. In the first stage, a constant current is applied until the terminal voltage level of the battery is maximum. The second stage is the stage where the voltage reaches its maximum level. At this stage, a decrease in the charging current is observed. The last stage is when the charging current reaches the minimum level. There is also a slight decrease in the battery terminal voltage at this stage. The graph in Figure 2.13 shows the changes in current and voltage according to the stages.

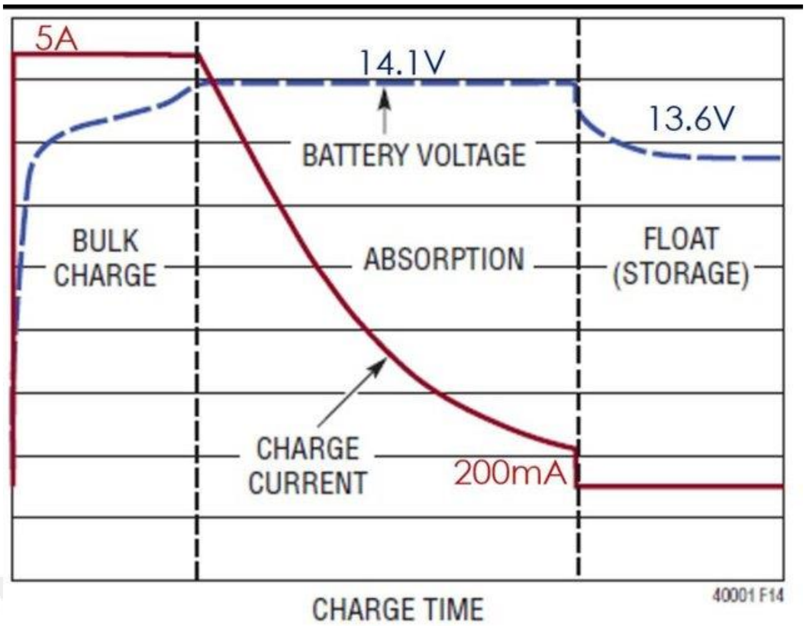

Figure 2.13. *Charging curve of lead acid battery (El Kamouny et al., 2015)*

2.3.3.2. Nickel cadmium battery (Ni-Cd)

Nickel-Cadmium batteries were introduced to the market by Waldemar Junger in 1899 (Miao et al., 2019). With the invention of this type of battery, more affordable batteries began to appear on the market. As a result of replacing the cadmium in the battery with iron in 1901, a new nickel-based battery emerged, but due to the decrease in its performance at low temperatures and the high internal discharge current of the nickel-iron battery, the usage area was not formed, and the studies were directed to the nickel-cadmium field. Liquid insulation of nickel-cadmium cells has been achieved over the years. Thus, these batteries have been widely used, but due to the damage to the environment, the use of these batteries in EU (European Union) countries has been restricted since 2013 (European Parliament, 2013). The advantages of nickel-cadmium batteries can be listed as follows;

- Possibility of simple and fast charging without high deterioration in the battery structure
- Stable energy supply even at low ambient temperatures
- Inexpensive compared to lithium batteries
- Long-lasting use with adequate maintenance
- Variety of size and performance
- Can be stored in discharged state

Although this type of battery has many benefits, it also has many disadvantages. Those disadvantages are:

- Low energy density compared to new versions
- Periodic charging/discharging requirement for protection against adverse effects
- Relatively high internal discharge current
- Negative environmental effects due to the toxic nature of the cadmium in it
- Obtaining high voltage with more cell connections than other batteries when low voltage difference (approximately 12 Volt) occurs between cells

The charging method of nickel-based batteries is different from other battery types. The constant current constant voltage method in Li-Ion and lead acid batteries cannot be used. When Ni-Cd batteries are charged with a constant current, the rise in voltage acts independently. When the charging process is completed, a decrease in battery voltage and an increase in temperature over time are observed. The general cellular characteristics of the battery during charging are shown in Figure 2.14.

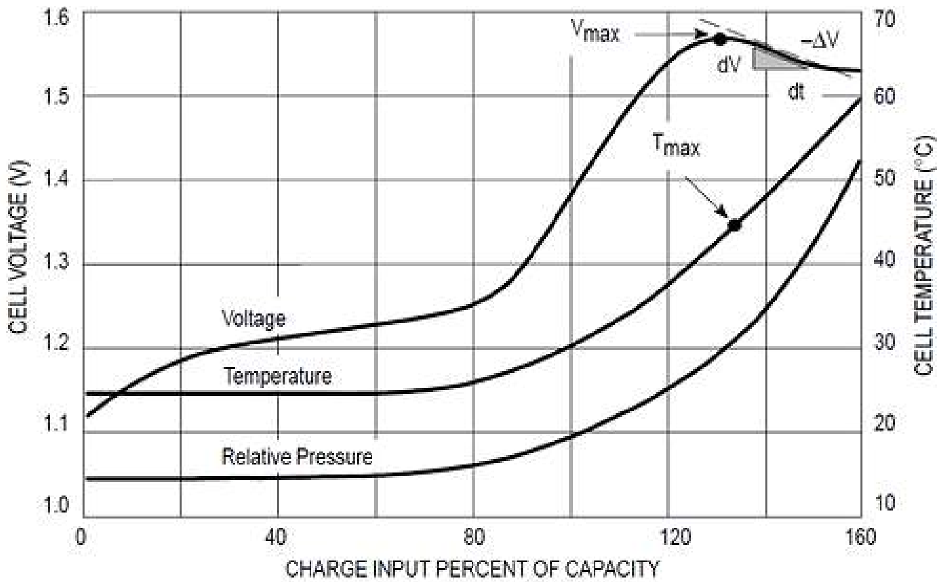

Figure 2.14. *Charging curve of nickel cadmium battery*

2.3.3.3. Nickel–metal hydride battery (Ni-MH)

After Ni-Cd batteries, more efficient and higher energy density Nickel Metal Hydride batteries have been produced. In addition, Nickel Metal Hydride batteries have started to replace Ni-Cd batteries over time because of not contain harmful substances (Muratoğlu & Akkaya, 2015; Cano et al., 2018). Although they have the same chemical structure as Ni-Cd batteries, the energy densities of Ni-MH batteries increase over time with the increase in technological developments (Cano et al., 2018; Vidyanandan, 2019). In addition, Ni-MH batteries have shorter charging and discharging times than Ni-Cd batteries. However, Ni-MH batteries with advanced technology and many advantages are more expensive than other batteries. They can also be self-discharged when not in use.

2.3.3.4. Lithium batteries

The popularity of lithium-based batteries, which emerged in the 1980s, increased with their commercialization in 1991, and lithium-based batteries began to be seen as one of the latest products of technology. In the first years of its invention, the imbalance in the anode material of lithium batteries caused a disadvantage for the development of this type of battery. For this reason, the idea of making the anode metal in battery design was abandoned, and studies were carried out on the non-metallic lithium-ion type. Although it seems like a disadvantage that lithium has less energy density than metal, its better reliability makes lithium-based batteries the reason for preference.

Lithium is an element that has high electrochemical potential and energy density and is considered in the category of light metals. Lithium, which is used as the anode material, provides high energy density in the battery, but this anode structure can produce undesirable chemical reactions. This undesirable reaction causes a short circuit in the battery (Vidyanandan, 2019; Gerlitz et al., 2021). However, there is an increase in temperature, and the heat level approaches the melting point of lithium, posing a danger. Thermal runaways are also observed.

Lithium-based cells have anode, cathode, and electrolysis to store energy. The battery has the anode as the negative electrode and the cathode as the positive electrode. The internal structure of the lithium-ion battery has a cathode made of metal oxide and an anode made of carbon material (Khaligh and Li, 2010; Miller, 2015; Wen et al., 2020).

Solid polymer electrolyte is used in lithium-ion polymer (LiPo) batteries. While the battery is charging and discharging, the Lithium ions in it are exchanged between the plates. In these battery types, an increase in voltage is observed when cells are connected in series, while an increase in current is observed when connected in parallel.

Lithium-ion battery

After the problems experienced in lithium-based batteries; Lithium-ion battery has become one of the most preferred battery types due to its fast charging, high energy density, light weight, small volume, low maintenance costs and environmental friendliness. In addition, the advantage of these batteries in terms of usage time and performance brings this battery type to the fore. However, low operating performance at low temperatures, short shelf life and high safety problems are the shortcomings of this battery (Pózna et al., 2017). Cells of lithium-ion batteries have a voltage value of approximately 3.6 Volts. For this reason, it can be said that this battery type has a high energy density. In addition, the active and electrolyte materials of these batteries can be shown among the reasons for their high energy density.

Lithium–sulfur battery

Today, especially with the increase in electric cars, the need for batteries with long-term endurance has begun to arise (Young et al., 2013). Therefore, battery technology has gained importance day by day, and studies on the subject have increased. With the researches, it is aimed to create batteries with better properties by changing the chemicals of current battery types. Thus, at the latest point in technology, new battery types have started to be developed by using substances such as sodium and sulfur in batteries (Muratoglu & Akkaya, 2015).

These newly developed Lithium-Sulfur batteries have a higher load-carrying capacity than other types with the new material used. In addition, Li-S batteries have a smaller volume compared to other batteries with the same load capacity. In other words, it is observed that the Li-S battery provides energy for a longer time when compared to the Li-S and another battery of the same size.

When these batteries were first invented, they had excellent properties in the theoretical tests, but it was observed that the cathode was damaged after the charge-discharge cycle at the time of application. This causes the battery to end its life and become non-rechargeable. However, upon this situation, researchers started to come up with new findings and turned to new methods inspired by previous studies to prevent deterioration in the battery. The Li-S battery, which was successful in the tests, thus extended its life and increased its operating performance.

When the technical features of the Li-S battery are compared with other lithium-based batteries on the market, it is seen that it has many advantages. While the Li-ion battery, one of the most used batteries, stores 150-200 Watt-hours of energy per kg, the level of 400 $Wh.kg^{-1}$ has been reached in 2016, as seen in Figure 2.14, with the development of Li-S batteries over the years. With the continuation of the studies, it has been seen that it has 500-600 $Wh.kg^{-1}$ weight energy densities in real use (Omar et al., 2010; Kisacikoglu et al., 2012; BuddeMeiwes et al., 2013). In addition, since the sulfur in the structure of the Li-S battery is one of the most abundant elements in nature, these batteries are more economical than other batteries on the market. The energy comparison of battery technologies can be seen in Figure 2.15.

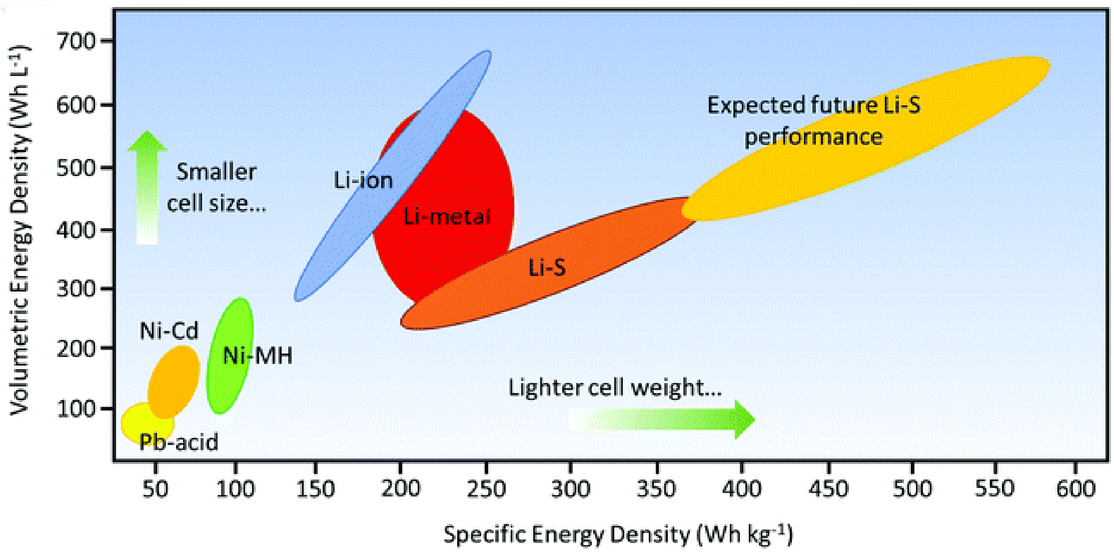

Figure 2.15. *Energy density comparison of different battery technologies (Hagen et al., 2015)*

3. DLR HIGH-ALTITUDE PLATFORM - HAP ALPHA PROJECT

The information under this topic has been written with reference to "Nikoderm and Biering, 2020", the document prepared for the DLR HAP project.

Due to the ability of aircraft to fly in the stratosphere, the usage areas of these vehicles have increased. With this increase, the HALE platform aircraft has become the focus of attention both in the academic community and in the industry (Watts et al., 2012). The vehicle designed in the project has the general advantages of the HALE platform.

The main purpose of using the HALE platform in this project is to take advantage of high altitude for scientific reconnaissance and surveillance missions. Since they are unmanned aerial vehicles, they can be used autonomously. Also, these vehicles have good take-off and landing skills. Furthermore, they have ease of maintenance and operate. It is known that aircraft on this platform have traditionally been used in remote sensing systems or Earth observation (Hepperle et al., 2007). In addition, they can take an active role in communication networks and crisis areas. Since airplanes and helicopters are not suitable for these missions, DLR has designed the 'HAP Alpha' aircraft seen in Image 3.1 for various scientific experiments using the mentioned advantages and is actively using it today.

Image 3.1. *The HAP Alpha design by DLR*

The HAP Alpha is designed to fly at high altitudes. Since the aircraft flies at a higher altitude than commercial aircraft, it is exposed to low air density and low temperature in the layer it flies. This aircraft requires high system security, and it is crucial to design it at the most optimum values.

3.1. Technical Information about Design

DLR continues its work on a high-altitude platform that can fly at the stratosphere level. This HAP Alpha platform is a solar-powered drone. 5 kg of the calculated total weight of the aircraft is the payload. The body of the aircraft constitutes 75% of the aircraft's weight. Although it is designed relatively light, a stable structure is achieved. In the design concept of the aircraft, the wing structure was determined as a tubular mast, ribs, and cladding. The pipes, which are used as the mast, body, and tail pillars, which form the basic skeleton of the vehicle, have been preferred to have wall thicknesses that vary according to the place of use. Carbon Fiber Reinforced Polymer (CFRP) sandwich rib structures are mounted in the main wing and tail sections. Its structural design is shown in Figure 3.1.

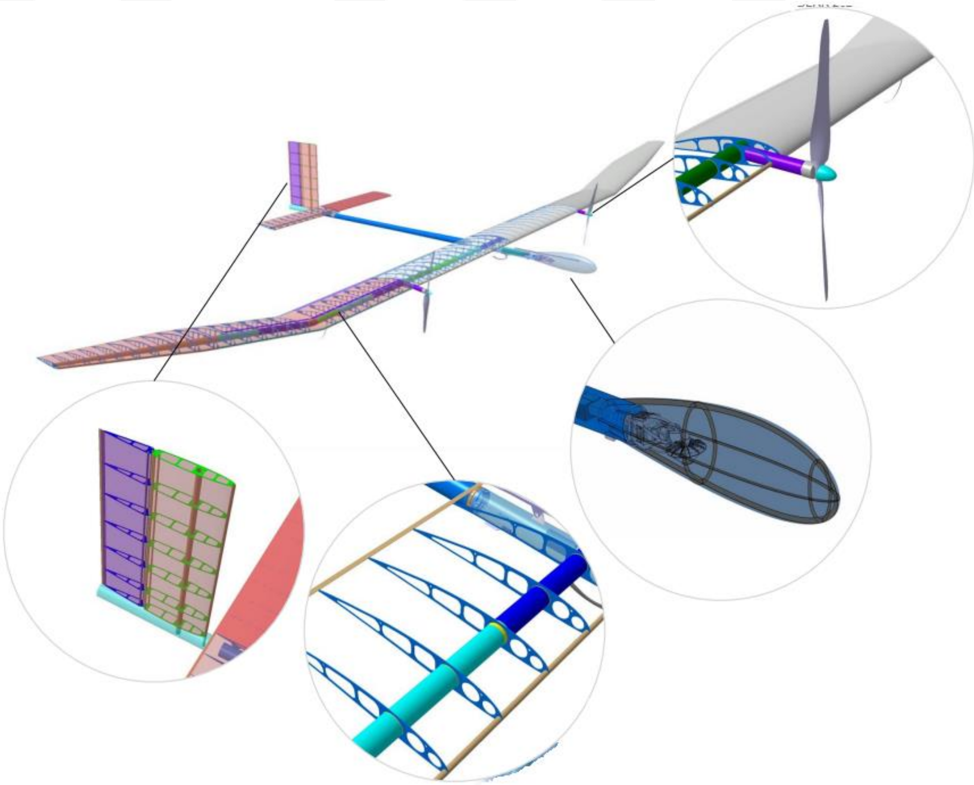

Figure 3.1. *Structure of HAP-Alpha (Nikoderm and Biering 2020)*

The aircraft, designed as seen in the design dimensions in Figure 3.2, has a length of 11 meters and a wingspan of 27 meters. This design provides ease of assembly.

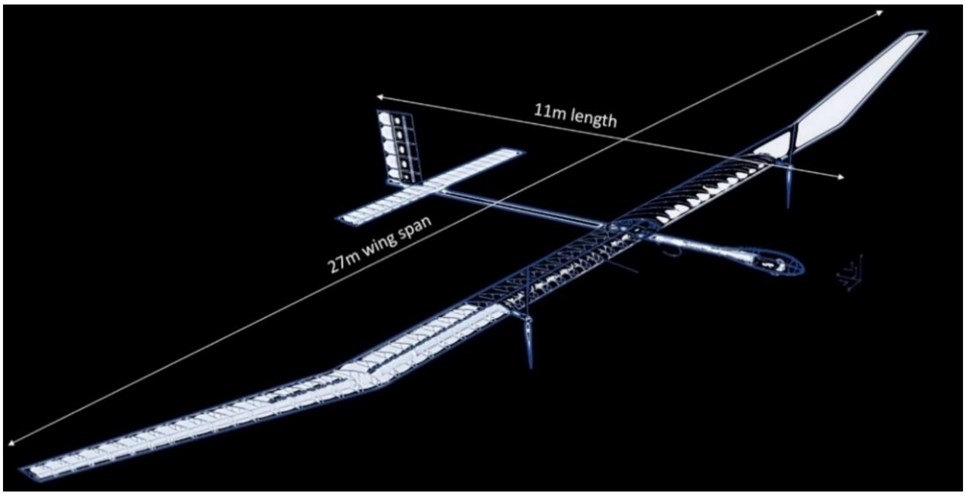

Figure 3.2. *The light-weight structure of the HAP Alpha (Nikoderm and Biering, 2020)*

This aircraft, which is aimed to fly at high altitudes, is primarily tested at low altitudes. In the second step, as shown in the graph in Figure 3.3, it reaches a certain cruise altitude with a parabolic altitude increase and then descends parabolically. It is aimed that the HAP will perform its mission for up to 24 hours, with a test period of 2 hours at an altitude of 20 km. Since the aircraft is flying at high altitudes, it is exposed to very low temperatures. Cruising flight at these altitudes and ascending and descending to these altitudes can be done by solar-powered PV panels and batteries. Structural materials and avionic systems used in the aircraft are produced at a total cost of 13 million euros. This aircraft, whose work started in 2018, is planned to make its first test flight at the end of 2022.

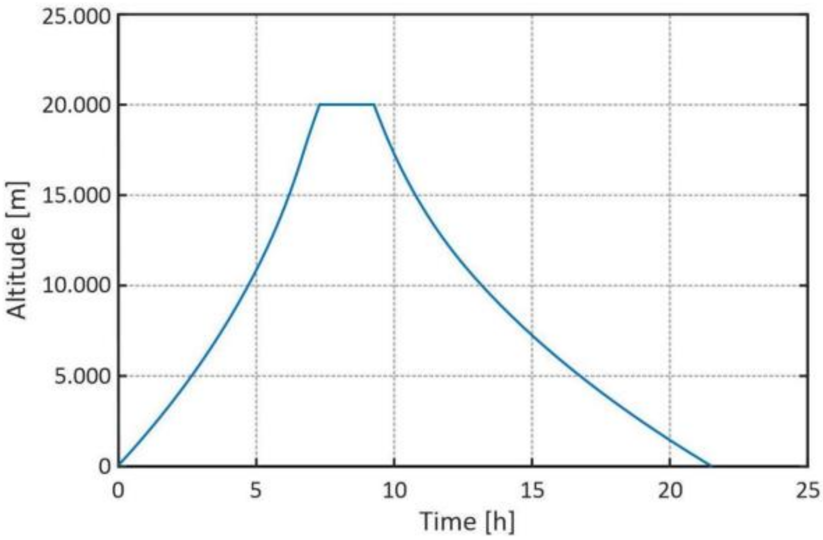

Figure 3.3. *HAP Alpha flight Altitude(m) – Time (h) graph (Nikoderm and Biering, 2020)*

When HAP Alpha performs a flight as shown in Figure 3.4, it is subject to variable conditions depending on altitude. Some of these have a fixed value, such as temperature, while some values, such as the irradiance value, vary according to the instantaneous situation. Irradiance varies depending on the values such as latitude, altitude, time of day, and day of the year, on which the UAV is flying and does not have a fixed value. Therefore, the irradiance values that the aircraft can be exposed to at the altitude are as in Figure 3.4.

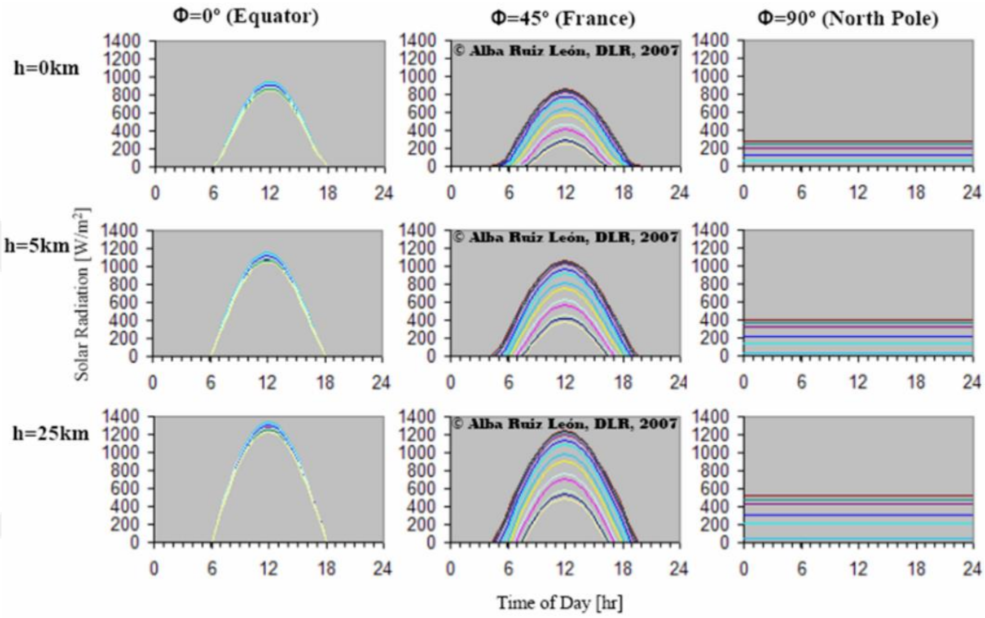

Figure 3.4. *Irradiance values under different conditions (Hepperle et al., 2007)*

The graph shows the variation of irradiance values at three different altitudes, according to 6-hour time zones and three different latitudes. Also, each colored line on the chart represents the months of the year.

In this case, the value of ϕ=45° (France) in Figure 3.4 can be accepted as the closest to the location, since DLR's HAP Alpha project tests will be carried out in Germany. In this case, according to different altitude values, the average approximate irradiance values for HAP Alpha for 12:00 PM in different months of the year are listed in Table 3.1 from low to high.

Table 3.1. *Average approximate irradiance values to which HAP Alpha is exposed, based on altitude in each month*

h=0 km (ground)		h=5 km		h=25 km	
Month	**Irradiance (W/m^2)**	**Month**	**Irradiance (W/m^2)**	**Month**	**Irradiance (W/m^2)**
1	250	1	375	1	500
2	300	2	400	2	550
3	375	3	450	3	575
4	400	4	575	4	700
5	450	5	625	5	775
6	575	6	750	6	900
7	650	7	800	7	975
8	700	8	925	8	1100
9	775	9	975	9	1150
10	825	10	1000	10	1200
11	850	11	1025	11	1225
12	900	12	1050	12	1250

The technical specifications of the HAP Alpha aircraft are given in Table 3.2.

Table 3.2. *Specifications of HAP Alpha (Birschmann and Heil, 2021)*

Wingspan	27 meters
Take-off weight	138 kg
Operating altitude	over 22 kilometers
Payload capacity	5 kg
Platform budget	13 million euros
Energy production	Triple-junction cells based on gallium arsenide (razor-thin, three-layer solar cells with a high efficiency of 32 percent and a power density of 1.40-watt.peak/gram)
Storage	Rechargeable lithium-ion batteries with silicon anode (energy density per cell: 350-watt.hours/kilogram)

3.2. The Purpose and Aim

The primary purpose of the Unmanned High-Altitude Platform (HAP) project is to gain digitization and security in the field of aviation and space. For this, comprehensive studies are carried out continuously at the German Aerospace Center (Deutsches Zentrum für Luft- und Raumfahrt; DLR). A knowledge base can be created by using general systems such as payloads and ground stations used through this HAP, and with this knowledge, these systems can be developed, and new ones can be built and operated.

Tests and studies have been carried out on every critical system for the aircraft, enabling the aircraft in the project to become a lightweight platform equipped with advanced technology, using small-sized avionics equipment and technologies with high storage capacity. When sufficient solar energy is provided for this aircraft, it can take place in the atmosphere at the desired altitude. Depending on the operation, the payloads can be changed to perform different tasks. One of the features that distinguish the vehicles on this platform from conventional aircraft is that they can fly for long periods at lower altitudes of the stratosphere without being affected by weather conditions.

The expected objectives of the HAP Alpha platform are as follows;

- Development of new system concepts and technologies for robust and cost-effective high-altitude solar-powered platforms
- Developing business strategies and mission plans to demonstrate the performance of high-altitude platforms
- Development and testing of innovative sensor systems for ground observation.
- Demonstration and flight test of new technologies, processes, and sensor systems

3.3. Design of Solar Cells

The selection of PV panels, which form the primary energy source of the aircraft throughout the flight, is a critical point. With the proper PV panel selection, the required powers for the avionics on the aircraft are met, and the battery in the aircraft is charged.

For the selection of solar panels to be used in the HAP project, four different solar cell technologies in Table 3.1 were compared with each other. For the purpose of this project, solar cell selection with the most suitable features has been made. According to Table 3.1, it was decided to use Triple junction based on Gallium Arsenide solar panel technology belonging to MikroLink company, which has superiority over others in terms of efficiency and power density. The selected Triple junction based on Gallium Arsenide solar cell's Wavelength Distribution of Solar Photo-Energy and Wavelength Sensitivity is shown in Figure 3.5, together with the graphic and layer structure.

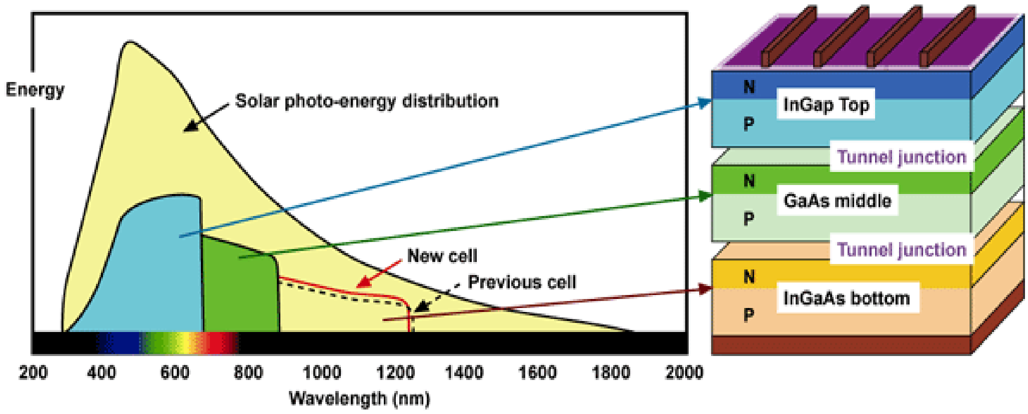

Figure 3.5. *Wavelength distribution of solar photo-energy and wavelength sensitivity of multi-junction solar cell (Nikoderm and Biering, 2020)*

The structure on the right of Figure 3.5 shows the three different layers that make up the Gallium Arsenide Solar Cell sequentially. The order from top to bottom is InGap-Indium Gallium Phosphide, GaAs-Gallium Arsenide, and InGaAs-Indium Gallium Arsenide. Tunel junction is the semiconductor junction where electricity flows as if through metal. On the left side of the figure, the regions corresponding to different materials in the structure of the multi-junction solar cell are shown in the energy-wavelength graph. Derived from the graphic, triple-junction solar cells, due to their structure and materials, ensure the absorption of sun rays with higher wavelengths.

Utilizing the PV panels placed on the wing surfaces, it can generate power from the sun's rays during flight. The number of solar cells used in the aircraft is determined by the wing surface area. According to the design of the aircraft, the maximum number of solar cells is placed on the surface area of the wing suitable for cell use. The number of solar cells placed in the designated area varies depending on the cell size.

Figure 3.6 shows the left-wing of HAP Alpha with solar cells placed. There is a representative picture of a module at the top of the Figure. Dimensional measurements are given on the top and left side of the solar cell shape. Under the solar cell figure, cells placed on a certain area of the wing are seen. A Triple-junction cell of MicroLink, which was decided to be used in the HAP Alpha project, has a surface area of 66x31 mm^2. Epitaxial Lift-Off (ELO) technology is used inside. In addition, irradiance is evaluated in terms of the air mass coefficient (AM), which is effective in its density after passing the earth's atmosphere and is therefore used as a criterion of solar cell performance. Solar cells used in UAV have more than 31% efficiency under AM1.5. This solar cell's

Temperature Coefficient of V_{oc} is -0.2%/K, and the Temperature Coefficient of I_{SC} is 0.08%/K. Moreover, the cell's total thickness is lower than 40 µm, so this feature makes the cell a more flexible structure. Thus, PV cells can easily cover the wing surface with their flexible structure. In the case of under AM1.5, the solar cell characteristic features are listed in Table 3.3 (Ackermann et al., 2021).

Table 3.3. *Solar cell characteristic under AM 1.5 condition*

Parameters	Real	Simulated	No tune
V_{OC} (V)	2.988	2.972	2.984
I_{SC} (A)	0.2465	0.2495	0.2803
V_{MPP} (V)	2.634	2.598	2.615
I_{MPP} (A)	0.2339	0.2381	0.2674
P_{MPP} (W)	0.616	0.6186	0.6991
η (%)	30.79	30.91	34.91

The module made of this Triple-junction cell has an open-circuit voltage of 70V-80V depending on the temperature. Twenty-four cells in series are placed on the surface area of a module. These cells form a module in the Figure 3.6, which will be 24x10 units. It is planned to use a total of 18 PV modules, 9 of which are PV modules on a single wing surface. As a result, by using 2160 cells in a single wing, a total of 4320 cells will be used on the wings. The area of the PV array placed on the wing surface is approximately 5 m^2. This configuration is also valid for the right-wing in Figure 3.6.

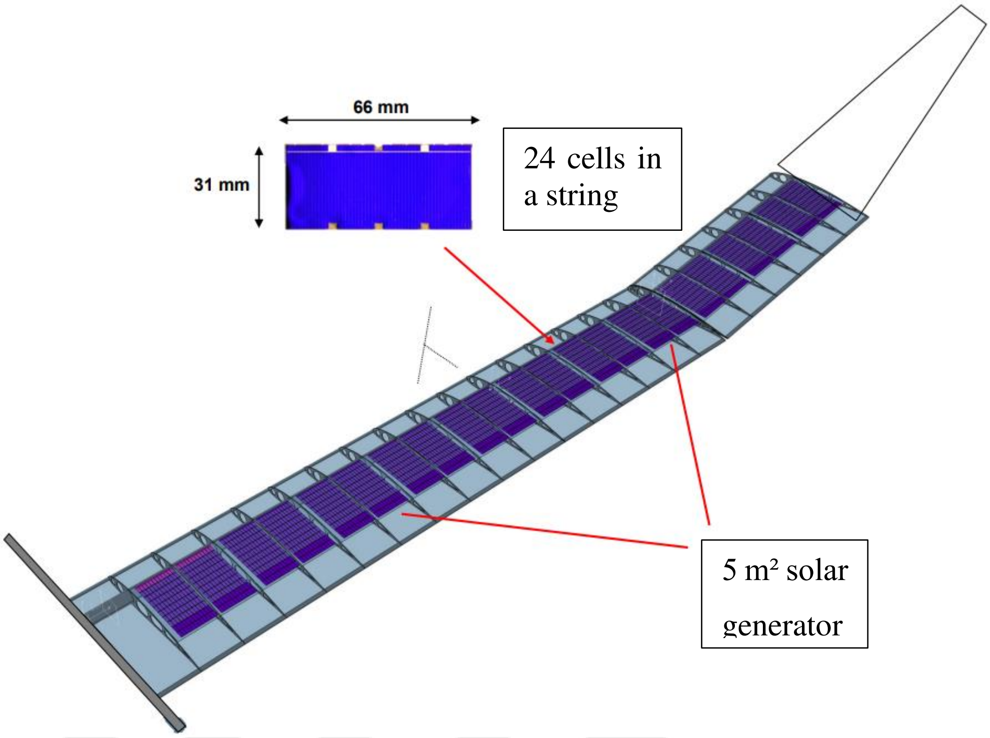

Figure 3.6. *Solar PV array design of a wing of HAP Alpha (Nikoderm and Biering, 2020)*

In the PV system, MPPT transfers the power taken from the wing to the battery and DC load. For this reason, it was deemed appropriate to connect 1 MPPT to two modules in parallel on one wing. Since the number of modules in a wing is odd, 1 MPPT will be connected to only one module (Figure 3.7). Each MPPT has a single channel. Therefore, it means that a total of 10 MPPTs will be used in the HAP-Alpha project (Figure 3.8).

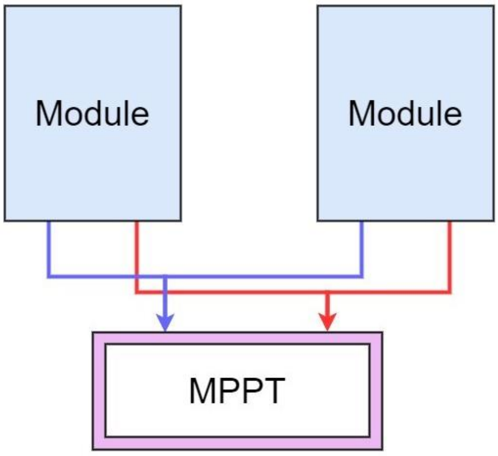

Figure 3.7. *DLR HAP-Alpha MPPT-module connection*

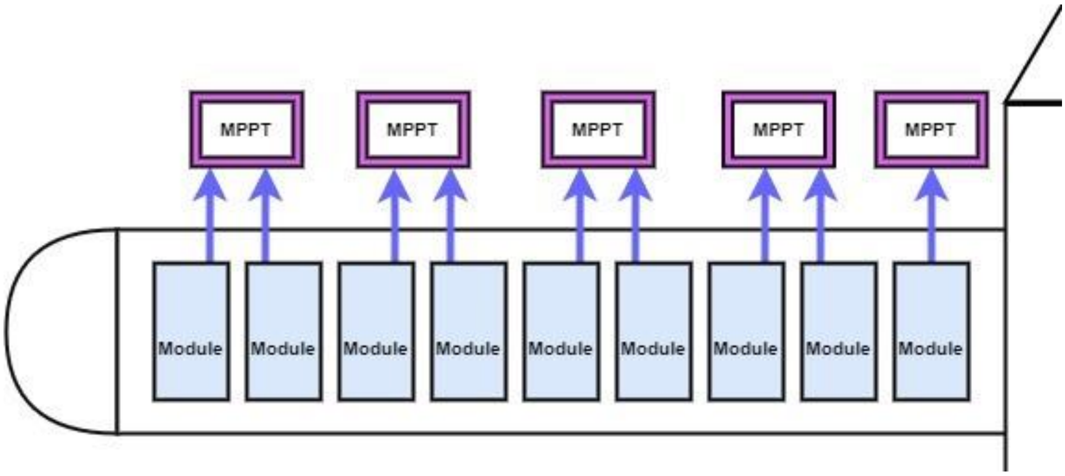

Figure 3.8. *MPPT left-wing configuration on DLR HAP-Alpha*

3.4. Battery Technology

Being able to store that energy is as vital as generating power from the solar panel. An energy source is needed for night flights, as solar panels provide electrical energy as long as the sun's rays are present. In this case, the battery plays a critical role. Therefore, the most suitable battery technology has been selected for the HAP Alpha. Batteries that can provide the necessary power for the avionics on the aircraft are mounted on the HAP Alpha.

The battery used for HAP Alpha must be suitable for charging by solar panels. Therefore, the choice of rechargeable lithium-ion batteries has been made. High power density is expected from the battery so that it can supply the systems on the aircraft with sufficient power throughout the flight. It is photovoltaic panels charged for up to 90 days of flight time. Silicon anode is preferred in order to get high-density energy from the battery. The use of silicon as the anode material allows more lithium to be stored, and thus the battery has a higher energy density. In the battery used on the HALE Alpha platform, the cellular energy density is measured as approximately 350 Wh/kg per cell. Although this is the expected measurement initially, it can be measured as 500 Wh/kg afterward. In addition, HALE platform aircraft are exposed to many variable weather conditions during their long flight times.

Different environmental and systemic variables that the battery will be exposed to may cause deterioration in the battery. Silicon Nanowire Technology is used as a precaution against this situation in the HAP Alpha project. With this technology, the rapid deterioration of the battery is minimized. Although the use of silicon in batteries has been suspended for a while due to the fact that the use of silicon causes swelling, in 2007, a solution to this problem was found with silicon nanowires, and batteries using 100% silicon were started to be produced (Chan et al., 2018). The first of these, Amprius, was decided to be used in the HAP Alpha aircraft. Thus, it will be possible to benefit from the high energy density provided by silicon. In addition, silicon batteries have the highest energy/power ratio and a good charge/discharge life.

The place of use of these batteries on the aircraft is shown in Figure 3.9. The image shows that the battery pack is integrated into the wing pillar and the fuselage. A battery pack consists of 17 cells connected in series. The end-of-charge voltage of the battery pack is 70 V. There are a total of 24 battery packs on the aircraft.

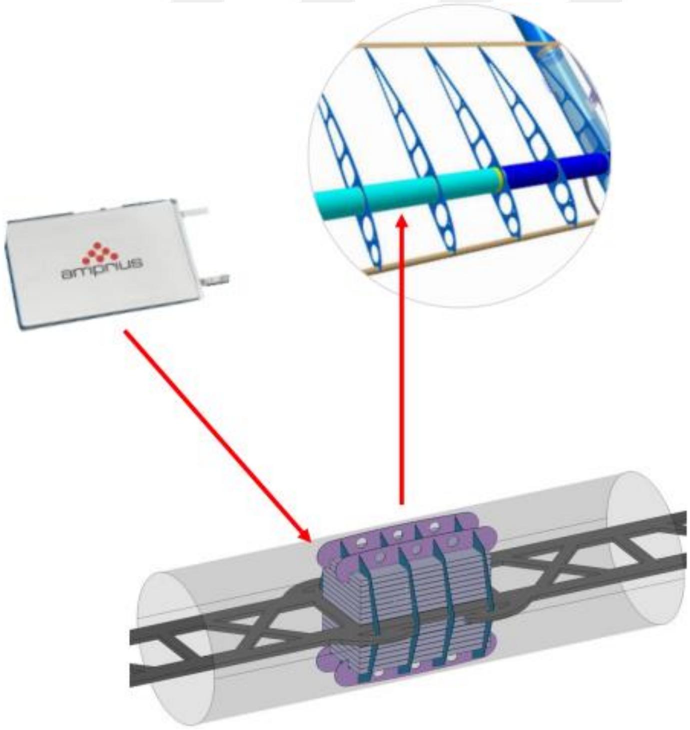

Figure 3.9. *Integration of battery in wing spar and fuselage (Nikoderm and Biering, 2020)*

3.5. Load Systems

It is aimed to perform many tasks in the use of the HAP-Alpha aircraft. To fulfill these targeted missions, the design and features of the aircraft were carried out in accordance with the purpose. There are many payloads on the aircraft for the systems required while performing the missions. The three payloads developed for the HAP-Alpha project are:

- Modular Aerial Camera System (MACS)

- High Altitude Platform Synthetic Aperture Radar (HAPSAR)
- Differential Optical Absorption Spectroscope (DOAS)

During the initial testing stages of the aircraft, studies were also carried out for the skeleton of the MACS. The performance of the system under real conditions has been examined.

3.5.1. Modular Aerial Camera System (MACS)

One of the payloads used in the HAP-Alpha aircraft is the MACS Camera System. The most basic feature that distinguishes this system from others is its self-aligning camera system. This camera system features a 150-megapixel sensor and 15 cm ground resolution. The system has the feature of scanning an area of 400 m^2. With the advanced technology of the MACS camera system, the embedded image analysis task can be performed with high performance. Using the sensors in the system, the target can be identified quickly, and thus on-board image analysis can be performed. This system can be used effectively to detect oil slicks and illegal fishing situations. The location of the MACS system inside the aircraft is shown in Image 3.2.

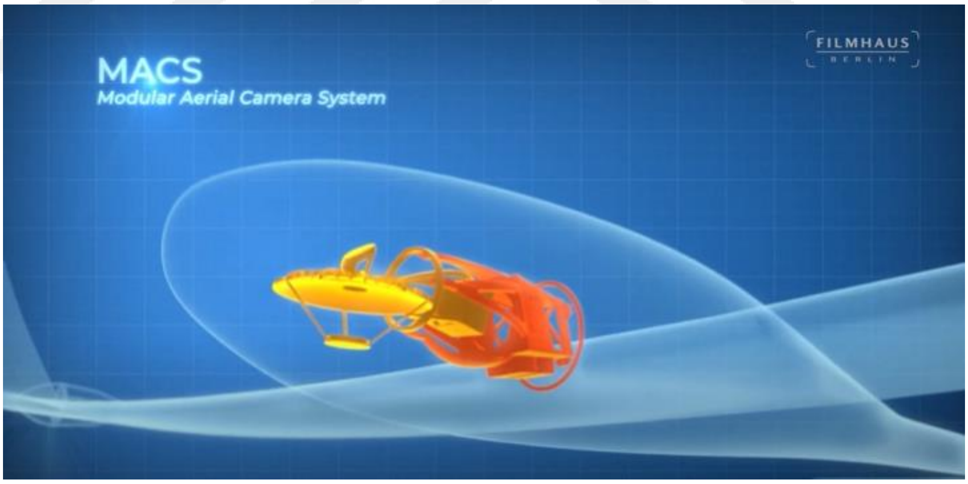

Image 3.2. *Location of the MACS system inside the aircraft*

The Modular Aerial Camera system has a beam source and a reflecting mirror inside. The beam source has three output points, and each output source has five lenses. These lenses are spaced at 5 μm intervals. A deflection mirror with focus adjustment is used to direct the signals coming out of these lenses. The signals reflected from the mirror are directed towards the desired area by passing through two focal points. Figure 3.9 shows how the deflection of the linear beams emitted by the lenses is accomplished with focus-adjusted mirrors. As shown in Figure 3.10, the total width of the system is 200.64

mm, and the total height is 336.8 mm. This system is located under the nose of the aircraft. As shown in Figure 3.11, the system is placed under the nose of the aircraft at a 60-degree angle to align the beams. This placement of the system also minimizes the power consumption of the HAP Alpha.

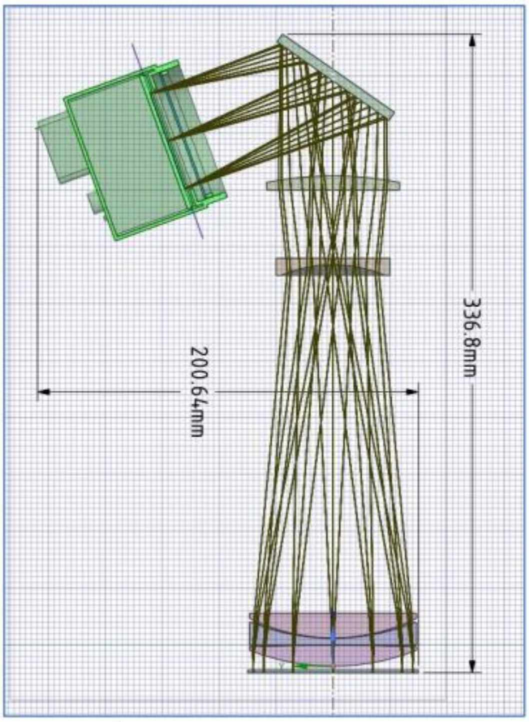

Figure 3.10. *Internal design of the MACS system (Nikoderm and Biering, 2020)*

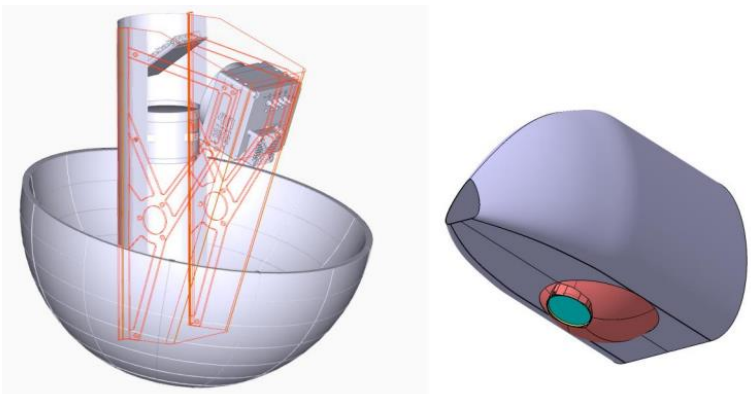

Figure 3.11. *Overview of the MACS system (Nikoderm and Biering, 2020)*

3.5.2. High Altitude Platform Synthetic Aperture Radar (HAPSAR)

The HAP-Alpha is built for cruising at high flight altitudes. The aircraft is exposed to many atmospheric effects, especially during long flights hours at its altitude, and environmental conditions can change rapidly during this flight period. However, it is expected that the aircraft will fully perform its duty in all environmental conditions. A radar system that can operate in all these conditions is placed on the HAP-Alpha. This system is named 'HAP Synthetic Aperture Radar (HAPSAR)' because of the technology it uses while performing its operation. It is possible to conduct a situation analysis under extraordinary conditions with this system. In crisis and disaster situations, it can analyze the environment at an altitude of approximately 20 km. In Image 3.3, there are images taken immediately before and after the event in the Danube flood area near Plattling/Deggendorf in June 2013 using HAPSAR technology. As can be seen from the image, short-term permanent recordings can be taken for unexpected situations. The HAPSAR system can operate 24/7 every day of the year. Using this system, which can operate in all conditions, in the HAP-Alpha aircraft, situation analysis can be performed by scanning the scene from a distant altitude in pre-defined missions. It provides a floor resolution of up to 60 cm.

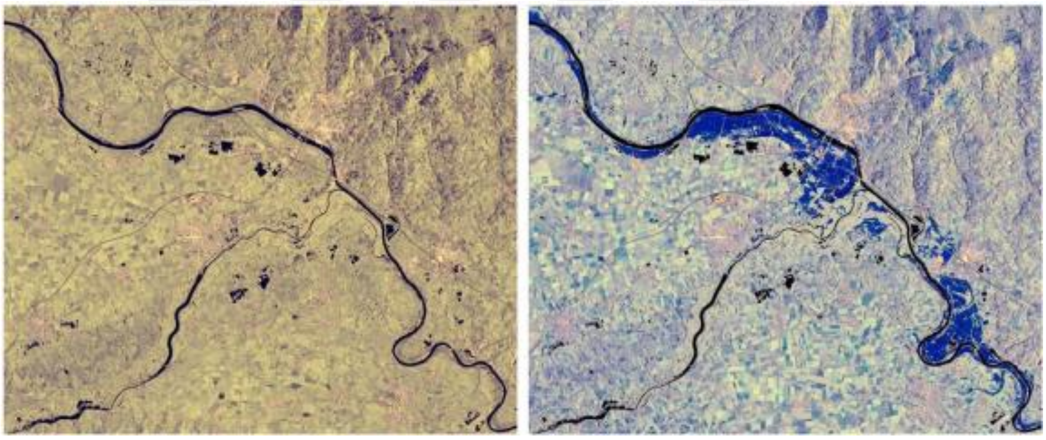

Image 3.3. *Image taken by the HAPSAR system before and after the Danube Flood (Nikoderm and Biering, 2020)*

The location of the HAPSAR system on the HAP-Alpha aircraft is shown in Image 3.4. This system is located in the nose of the aircraft. The weight of this system is less than 5 kg, and the system occupies several liters of volume with a small installation space. The HAPSAR system on the aircraft has advanced technology integrated with microwave electronics. The power consumption of the system on the vehicle is below 500 Watt. As in some electrical energy systems, this system also produces thermal equilibrium waste heat as a by-product while operating. Although this is an inefficient energy output for the waste system, the system heat can be used beneficially in cases where the operating conditions are cold. The limited data rate of the system in communication with the ground station poses a technological challenge for the system. The design of the radar has been made considering the conditions in which it will operate. Changes that occur can be detected with high accuracy by radar. In this way, it can observe natural damage situations and keep them in permanent records. The HAPSAR system has the most suitable design under environmental factors and limited conditions during operation (Nikoderm and Biering 2020).

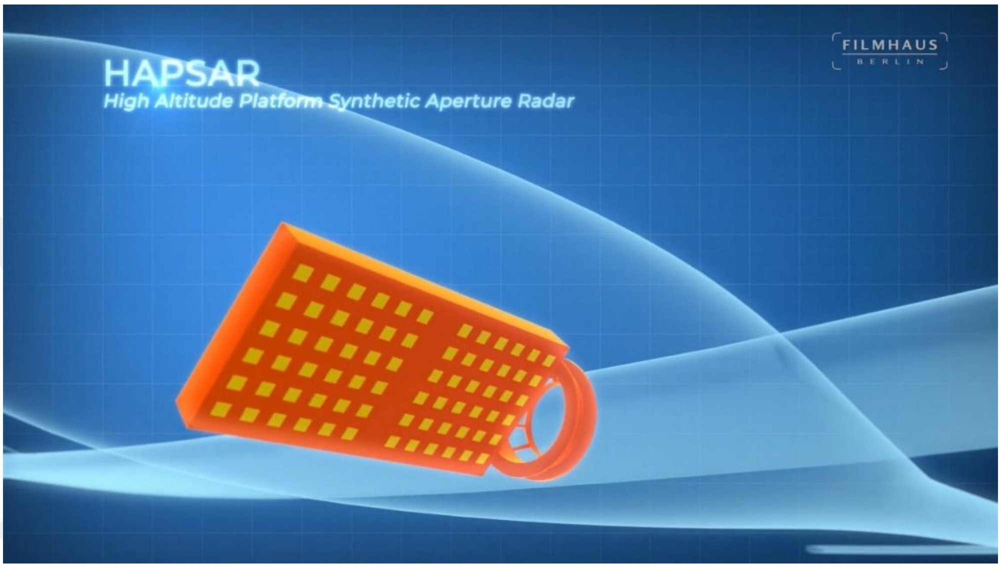

Image 3.4. *View of the HAPSAR system on the aircraft (Nikoderm and Biering 2020)*

3.5.3. Differential Optical Absorption Spectroscope (DOAS)

Another system that works effectively in the aircraft is the Differential Optical Absorption Spectroscope (DOAS), which can also be referred to as a Gas spectrometer. It is a system that plays an active role in the absorption of light by the solar panels on the aircraft. The light scattering detected by this system varies according to different conditions. The change in this scattering creates a difference in the amount of light absorption in the system. In addition, the amount of absorption changes due to trace gases in the atmosphere. Absorption is a characteristic feature for trace gases when the system is considered individually. This absorption can be explained by the Beer-Lambert Law. The general equation of this law for the spectroscope is in Equation 3.1.

$$T = \frac{I}{I_0} = e^{-\sigma l N}$$
$$I = I_0 \, e^{-\sigma d N} \tag{3.1}$$

Here; T is the transmission of light in the material it comes into contact with, I is the intensity of the leaving beam, I_0 is the intensity of the incident beam, σ is the light absorption cross-section of a single particle, d is the distance the light travels through the material (path length), N is the density of the particles absorbed per volume.

Based on these equations, the equation in Equation 3.2 was created.

$$A = \log\frac{Io}{I} = \varepsilon dC \quad (3.2)$$

Here; Io is the light intensity coming to the PV cells, I is the light intensity leaving the PV cell, ε molar absorption coefficient (L mol^{-1} cm^{-1}), d is the path length of the beam, C is concentration (mol L^{-1}) and A is absorbance.

The appearance of the DOAS system on the aircraft is given in Image 3.5. This system is also used as an air analysis system. The equipment weight of the DOAS system is approximately 2 kg, and the volume is approximately 20 liters. Air analysis of the regions where the aircraft is scanning can be done, and the air pollution rate can be found. Thus, the situation in which the amount of substances causing air pollution in countries is within or outside the limits can be examined.

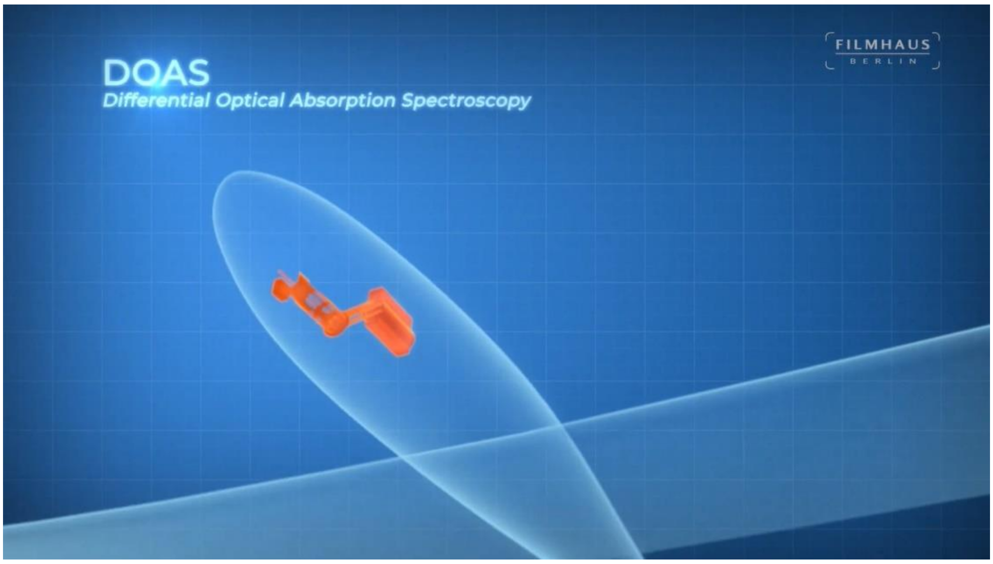

Image 3.5. *View of the DOAS system on the aircraft*

4. MPPT

The output power of solar panels varies depending on the irradiance and temperature conditions (Faranda et al., 2008; Podder et al., 2019). For this reason, Photovoltaic (PV) panels do not have linear voltage-current characteristics. Although the PV panel output values vary due to environmental conditions, there is a point where the generated power is maximum under every situation. For this reason, the point where the power obtained in PV systems is maximum is called the maximum power point (MPP), and the system developed to keep it at this level is called the maximum power point tracking (MPPT) system (Faranda et al., 2008). The efficiency of the power to be obtained from solar panels is directly related to the maximum level of electrical power converted by PV systems after exposure to sunlight. Therefore, this maximum level is directly affected by power efficiency (Yadav et al., 2012). With this developed MPPT system, the PV panel works at maximum power, increasing the efficiency of the overall system and the total power produced (Mosa et al., 2017; Podder et al., 2019).

Maximum Power Point Tracking (MPPT) is a photovoltaic (PV) converter algorithm that constantly monitors the PV panel output power point to maintain the efficiency of the PV system and continuously changes the duty cycle of the system to do so. With the first award in the solar panels' category in 1954, increasing the efficiency and working performance of these panels has become a new field of study for researchers (Eltamaly and Farh, 2020). Thereupon, studies were carried out to determine the point where the PV panels reach the maximum power by examining the P-V relationship under different conditions. The variability in this MPP is seen in the graph in Figure 4.1.

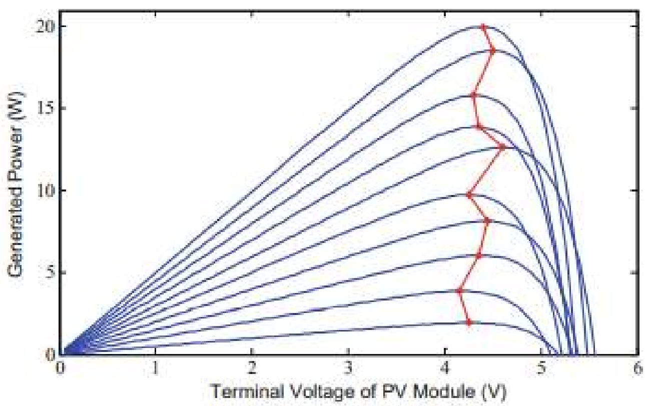

Figure 4.1. *MPP change of a PV module under different conditions (Farh and Eltamaly, 2020)*

4.1. Workflow of MPPT

MPPT is used to provide power control in the PV system. It performs this power control through the connection between the PV panels and the battery. In order to do this, a converter is placed between the PV panels and the battery in the PV system. The general scheme of the PV system and the position of the MPPT in the system are shown in Figure 4.2.

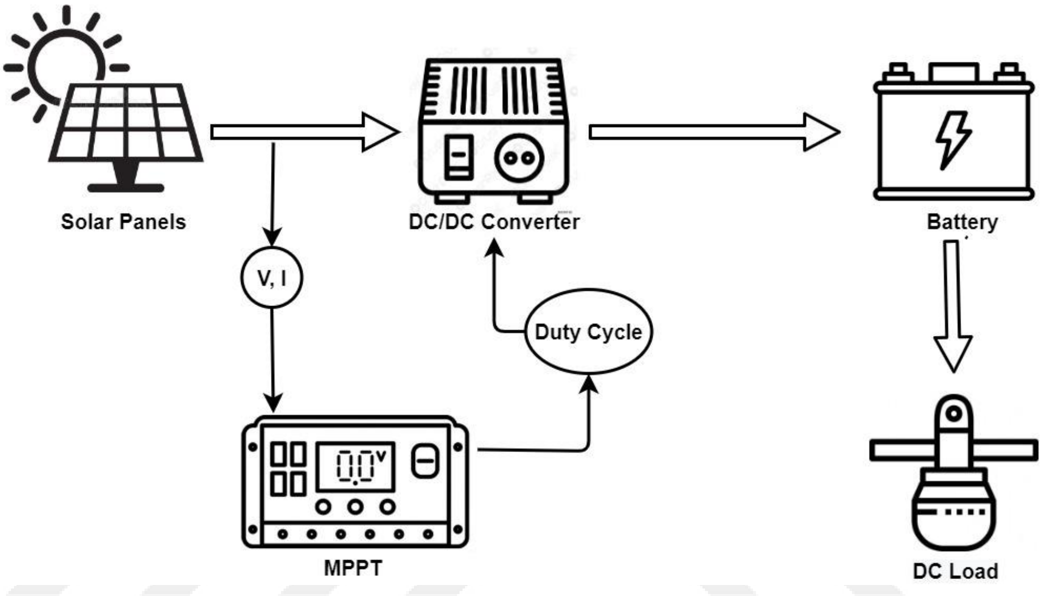

Figure 4.2. *Basic diagram of the PV system*

The MPPT algorithm sends a signal to the converter for adjusting the duty cycle to control the power. Before the control signal is generated, various measurements such as output voltage and output current from the PV panel are transmitted to the MPPT algorithms. Based on these measurement values, MPPT algorithms estimate the maximum power point of the PV panel. As a result of this estimation, the control signal is generated and transmitted to the DC-DC converter. Thus, the control signal becomes the switching signal of the DC-DC converter. This switching signal allows the DC-DC converter to modify the operating points of the PV panel. This process controls the power obtained from the PV system as long as the system is running and ensures that more power is obtained from the PV panel. The effect of the MPPT system on the output power of the PV system is shown in the Power-time graph in Figure 4.3.

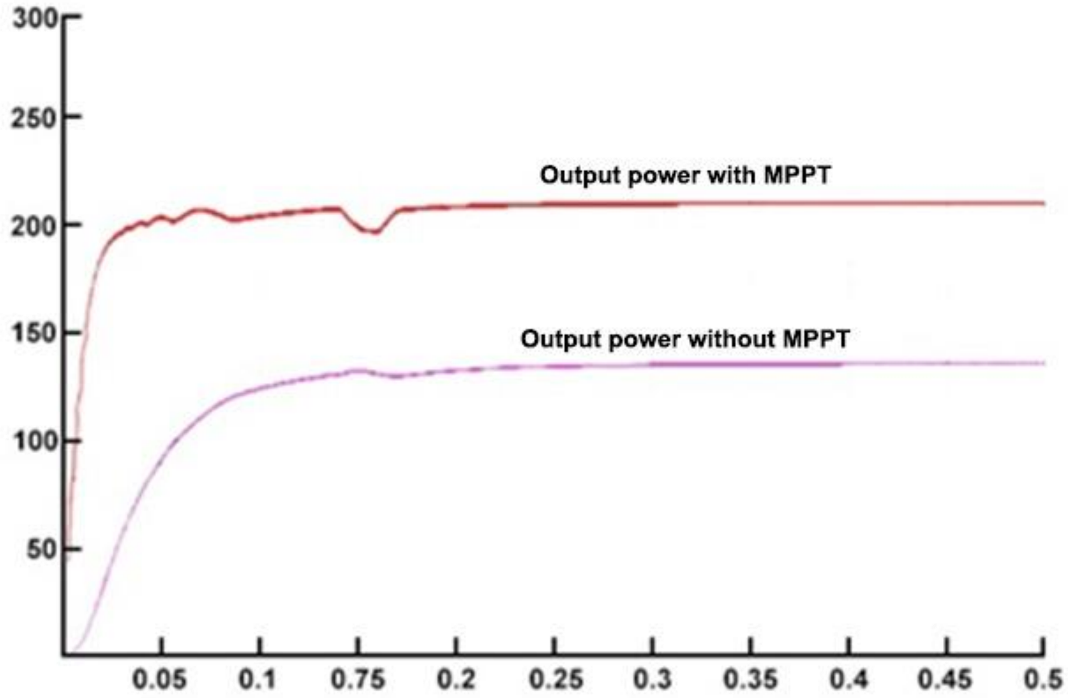

Figure 4.3. *Comparison of output voltage with and without MPPT (Sharma and Katti, 2017)*

MPPT algorithms are one of the most essential elements for the efficiency of PV systems. Therefore, MPPT algorithms are used quite frequently in PV system designs. Changing irradiance and instantaneous temperature values depending on the environmental conditions in which the aircraft is flying cause the MPP to change. Using these algorithms, optimum PV power generation is provided under variable conditions such as different irradiance and temperature.

The operation logic of MPPT is developed on maintaining a certain ratio between maximum power parameters and PV module parameters. This process takes place by controlling the voltage or current. These two different voltages are balanced by changing the converter loop.

In order to MPPT algorithms work optimally in a PV system, they must have the following features (Atia, 2020);

- Rapid response to changing environmental conditions
- Operating performance of PV arrays should not be affected depending on whether they are parallel or serial connection

- There should be robustness against the changes in instantaneous environmental conditions and accordingly the changes in the output value of the PV panel
- System cost should be economical
- Calculations during operation should be simple and provide ease of application.

4.2. Benefits of MPPT

MPPT has an important place in supplying power to avionic equipment in solar-powered UAVs. MPPT, which acts as a solar charger between PV panels and the battery, ensures that the battery is always charged with the most accurate current value with the power obtained from the solar panels. Therefore, the primary purpose of MPPT is to regulate the charging time of the battery and to ensure that the battery is charged optimally. MPPT does this with as little current loss as possible. It cannot be said that MPPT prevents the battery from being over-charged, but the probability of an overcharged battery is lower than the system without MPPT. Thus, MPPT performs the battery's charging process in the system more sensitively and more efficiently.

The MPPT system plays a critical role when the aircraft needs extra power. Some of these situations are as follows:

- **Cold weather** - Solar panels work more efficiently in cold weather. But the excess power gained is lost without use. MPPT prevents energy loss in these cases, especially in winter when solar energy is low. Excess power is stored in the batteries, and it provides the power to be met when this power is needed.
- **Low battery charge** – Another situation where extra power is needed is a low battery charge. In these cases, the MPPT current acts inversely with the battery's state of charge. In other words, the amount of current transferred by the MPPT increases as the charge of the battery decreases.
- **Cable length** – The criticality of this situation depends on the structure of the system used. In other words, if the PV panels placed at a distance of 100 ft from the battery on the aircraft are expected to charge a 12 Volt battery, voltage drop, and power loss depend on the large wire. These problems do not occur if a large wire is used. However, this increases the overall cost of

the system. If this battery is charged using 4 PV modules connected in series and a 48 Volt PV panel, the power loss is minimal. In this case, voltage conversion is required with the help of a converter to power the 12-volt battery. Also, if the PV panel connected to the converter has a high output voltage, a smaller diameter cable can be used.

Some factors affecting the efficiency of MPPT are given in Figure 4.4.

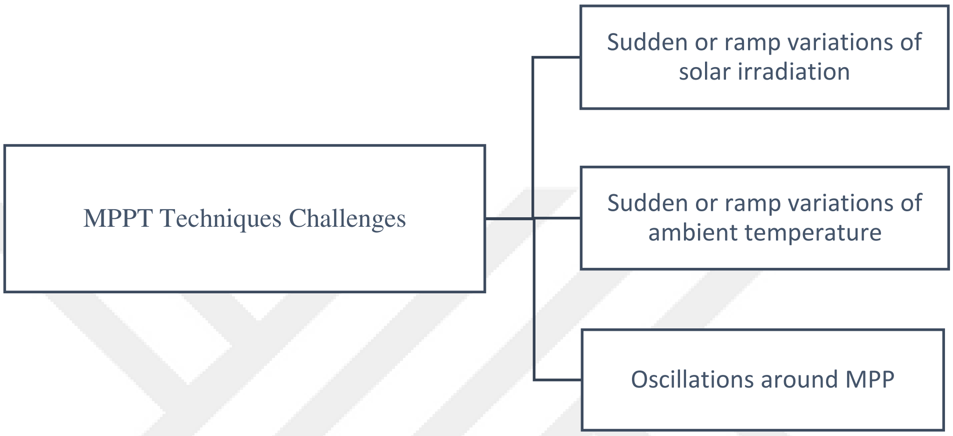

Figure 4.4. *Challenges of MPPT techniques (Eltamaly and Farh, 2020)*

4.3. The Factors Affecting the Operation of MPPT

Earth's atmosphere consists of different layers. As seen in Figure 4.5, each layer has different temperature, density, and wind speed values according to its location. Aircraft can fly in the layers of the lower levels of the atmosphere, where the Troposphere is between 0-11 km and the Stratosphere is between 11-47 km. This is because the air density, which provides the aerodynamic lift required for the flight of aircraft, is limited between these altitudes. This altitude range is not preferred for High-altitude platforms since civil aircraft fly within the 9-12 km range of this limited flyable airspace. Thus, communication with air traffic control systems is not required. That is why HAP platforms fly over 12 km. Preferring the stratosphere layer for HAPs provides an advantage due to the low level of wind profiles. This also reduces the power requirements.

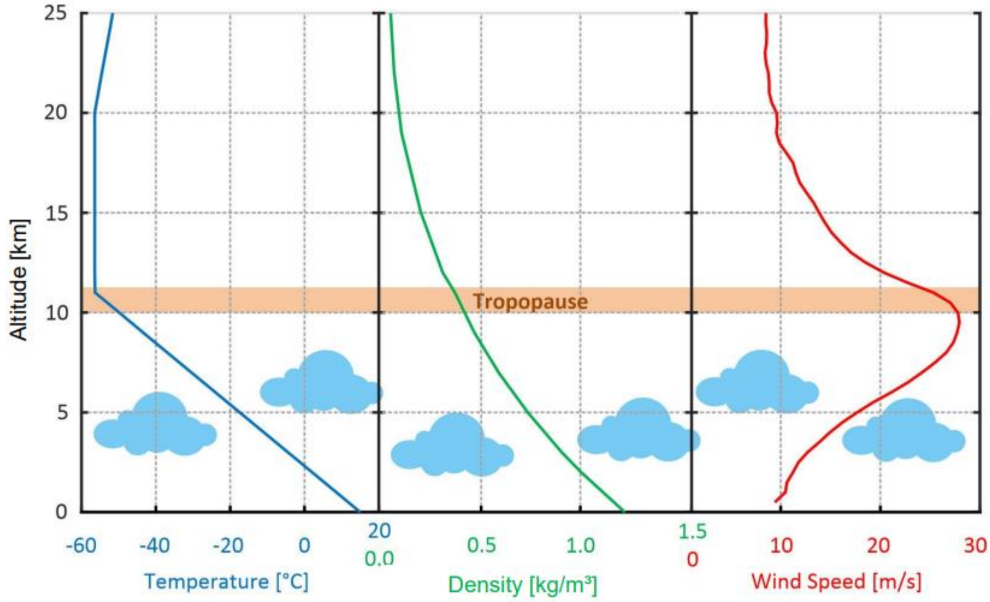

Figure 4.5. *Standard atmospheric conditions*

4.3.1. Various irradiance conditions

The power delivered by the PV panels to the MPPT differs depending on the amount of sunlight falling on the panel. This is seen in Figures 4.6(a) and Figure 4.6(b). The graph in Figure 4.6(a) shows the P-V variation of the PV panels at different irradiance values at a constant temperature, and the graph in Figure 4.6(b) shows the I-V variation under the same conditions. The tested values are the standard values used in the tests of PV panels in the literature. (Mota and Vieira, 2010; Othman et al., 2012; Ibrahim and Anani, 2017; Mohsin and Abdulbaqi, 2018)

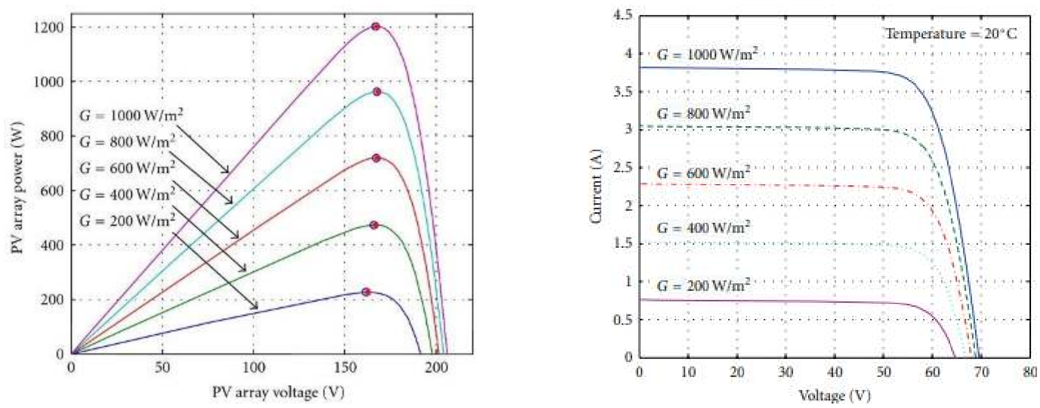

(a) (b)

Figure 4.6. *Effect of irradiance on operating point of PV panels under constant temperature; (a) P-V curve and (b) I-V curve (Mohamed and Shareef, 2011)*

As seen in Figure 4.6, the output power of the PV panel can be calculated theoretically according to the changing irradiance values when the temperature is at a constant value in standard conditions. The increase in the irradiance density under constant temperature creates a positive effect on the PV panel output current, and a direct proportional increase in the short circuit current is observed. MPP changes significantly with irradiance change, especially as can be seen at the red marked points on the P-V curve in Figure 4.6(a). A change in the irradiance value also causes a change in the MPP value. When the P-V curve is analyzed, there is a disproportionate increase in the open-circuit voltage. Even when the irradiance density is low, there is no significant reduction in voltage value. PV output values are measured by assuming irradiance density as 1000 W/m^2 and temperature as 25 °C in international standards. However, it is not always possible to work with these values in real life. Because PV output current and voltage values are affected by temperature, light intensity, and parallel-series resistances. Therefore, the irradiance value at a certain altitude varies depending on many parameters.

Variables such as temperature, light intensity, and dusting on the panels cause fluctuations in the amount of power that can be obtained from PV panels. MPPT algorithms minimize the fluctuations caused by these factors in the power extract from the panels.

When Figure 3.4 and Table 3.1 are taken into consideration, there is a change in the amount of irradiance due to variable environmental conditions at different altitudes. As can be seen in the study, it is seen that three different altitudes have a great effect on irradiance, depending on the location of the study. Moreover, the position of the sun during the day also affects the irradiance value, and it is highest when the sun is directly overhead at 12 o'clock. In addition, the angle of incidence of the beam causes variability depending on the location in the month of flight. In other words, in the Equator (ϕ=0°), the irradiance change is low in different months of flight, while it is high in the poles. Each of these situations affects the power to be produced from the panel. Decreases and increases in power due to environmental conditions affect the operational performance of the MPPT. The role of MPPT is more critical in such cases, as each change in power will cause the MPP point to change as well.

4.3.2. Various temperature conditions

Another factor that causes a change in PV array output power is ambient temperature. The temperature to which the aircraft is exposed varies depending on the altitude at which it is operating. Unlike irradiance, the temperature parameter that affects the MPPT operating performance is a predictable standard value according to the atmospheric layer. The temperature change according to the layers is seen in Figure 4.2. It is observed that the atmospheric temperature is -60ºC (215 K), especially at altitudes between 10 and 24 km, where HAP aircraft can fly. This low temperature can adversely affect the thermal heat and systems inside the aircraft. Depending on the altitude at which it will fly, attention should be paid to the air temperature, and the payload should be protected. At this low temperature, heating is done to protect the systems, and extra power is spent on this. Prior to the flight, the system and aircraft structure should be tested with regard to the temperature value at the altitude at the flight will occur and should be prepared in accordance with the relevant conditions. Because low air temperature and humidity not only have a negative effect on the systems but also cause icing of the aircraft. This icing eventually creates extra weight and friction on the aircraft and affects the lift force. In addition, at altitudes where HALE aircraft fly, the humidity values are extremely low along with the low temperature. Therefore, the icing problem does not appear in these vehicles. However, care should be taken against icing during the ascent and descent.

For the PV panel on the aircraft, the I-V and P-V graphs of the panel under constant irradiance and variable temperature conditions are given in Figure 4.7(a) and Figure 4.7(b), respectively. The tested values are the standard values used in the tests of PV panels in the literature (Othman et al., 2012; Saharia and Saharia, 2016).

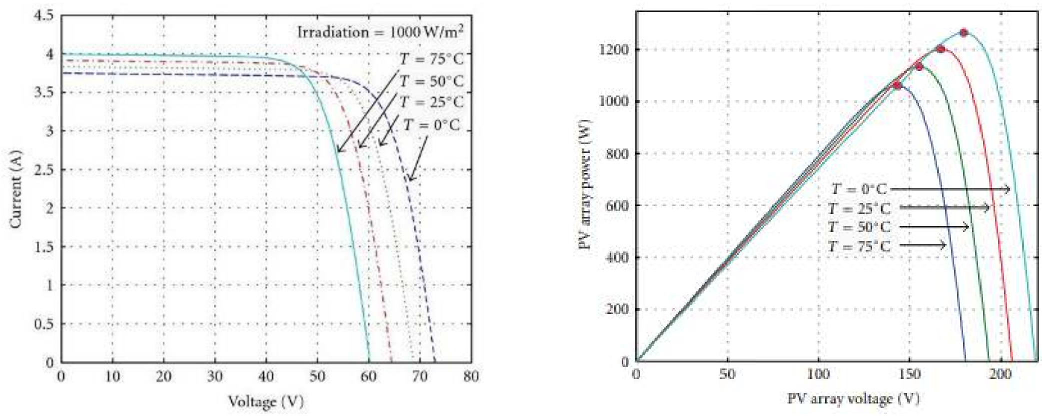

(a) (b)

Figure 4.7. *The effect of temperature on the operation of PV panels; (a) I-V curve and (b) P-V curve (Mohamed and Shareef, 2011)*

Brizon, in a study in 2015, conducted tests regarding places with four different geographical locations. Quebec, one of the four places where the operational tests were conducted, is a city in the northern hemisphere with a latitude of 45º. The output data obtained on the in-flight PV panel temperature of the UAV, which was flown at a 15 km altitude in this city, was evaluated. In the test study, when the angle between the wind flow and the UAV surface was accepted as zero, the latitude was 45°, whereas the output power decreased as the altitude increased. In addition, as the air temperature at which the test was carried out increased, the output power decreased. As seen in this study, no matter how much the ambient temperature varies, the main factor affecting the PV panel is the solar cell temperature. The graph in Figure 4.8 shows the relationship between the temperature of the solar cell and output power according to the test results obtained at 45° latitude and at 12:00 pm.

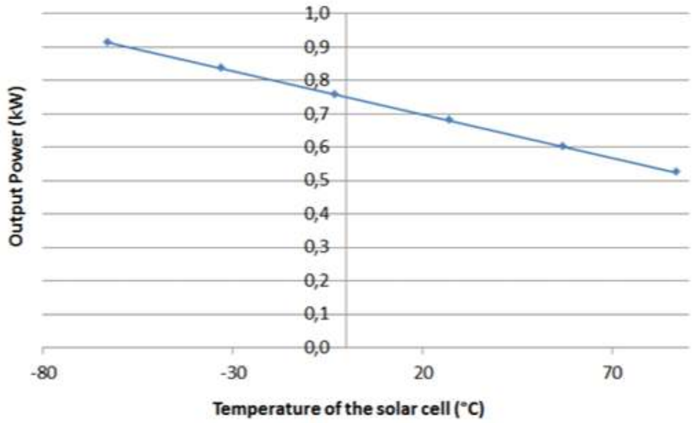

Figure 4.8. *Relation between output power and temperature of solar cell (Brizon, 2015)*

At high altitudes, the cooling effect caused by the airflow significantly reduces the temperature of the solar cell. In addition, since the air density is less than sea level, the heat is spread more and more. It is seen that the temperature difference between the solar panels and the ambient temperature increases as the Altitude increases. The efficiency of solar panels increases up to about 11 km as the solar cells cool down. Then, as the solar cells heat up, the PV panel's efficiency decreases. The maximum electrical power generation efficiency of PV panels is about 11.5 km (Keidel, 2000).

Following this section, information about MPPT algorithms and circuit structures used for MPPT will be given, and the circuits and algorithms used in this study will be examined.

4.4. MPPT Algorithms

The maximum power point varies due to many parameters such as variable light intensity, temperature, angle of incidence of sunlight, usage time of the panels, and pollution of the panel surface. The output current and voltage values of the PV panel are monitored in order to follow this point in every variable condition. Algorithms have been developed that can follow this point. These algorithms are divided into two as indirect and direct control algorithms.

An essential feature of the algorithms that make indirect control is that they do not constantly track the parameters such as current and voltage, which play an active role in the output power of the panel. In this control system, the panel voltage, current, and irradiance values are measured or estimated with experimental data and mathematical calculations to determine the point where the PV panel power is maximum. Examples of these algorithms are:

- Open circuit voltage technique
- Short circuit current technique
- Constant voltage technique
- Constant current technique

In direct control algorithms, the photovoltaic panel output values are continuously tracked. The values obtained from them are compared with the values in the previous step. As a result of this comparison, the most suitable operating conditions for the system are provided. The biggest contribution of these algorithms compared to the other group is the continuous tracking of the output current and output voltage values of the PV panel. Thus, it is ensured that the maximum power is extract from the PV system under the environmental conditions of the aircraft instantly. This situation can be applied to any irradiance and temperature. Examples of these algorithms are:

- Perturb and Observe technique
- Incremental Conductance technique
- Hill Climbing technique

In this section, Perturb and Observe, Incremental Conductance and Hill Climbing algorithms, which are the most used direct control algorithms, will be examined (Motahhir et al., 2020).

4.4.1. Perturb and Observe (P&O) algorithm

Among the MPPT algorithms, Perturb and Observe algorithm is the most popular and the most used one in terms of economy and easy applicability (Abdel-Salam et al., 2018; Shadlu, 2019; El-Atab et al., 2021). This algorithm is also referred to as the P&O Algorithm. The operational logic is to send a signal to the DC-DC converter to regulate the voltage of the system according to the values measured from the PV panel. This algorithm measures the output voltage and current of the PV panel and calculates the power of the PV panel based on this measurement. Then, it changes the duty cycle of the DC-DC converter until it finds the maximum power point. The change in this duty cycle by changing the voltage amount with the signal it sends. This process is repeated to find the MPP point. Figure 4.9 shows the operating logic of the P&O algorithm.

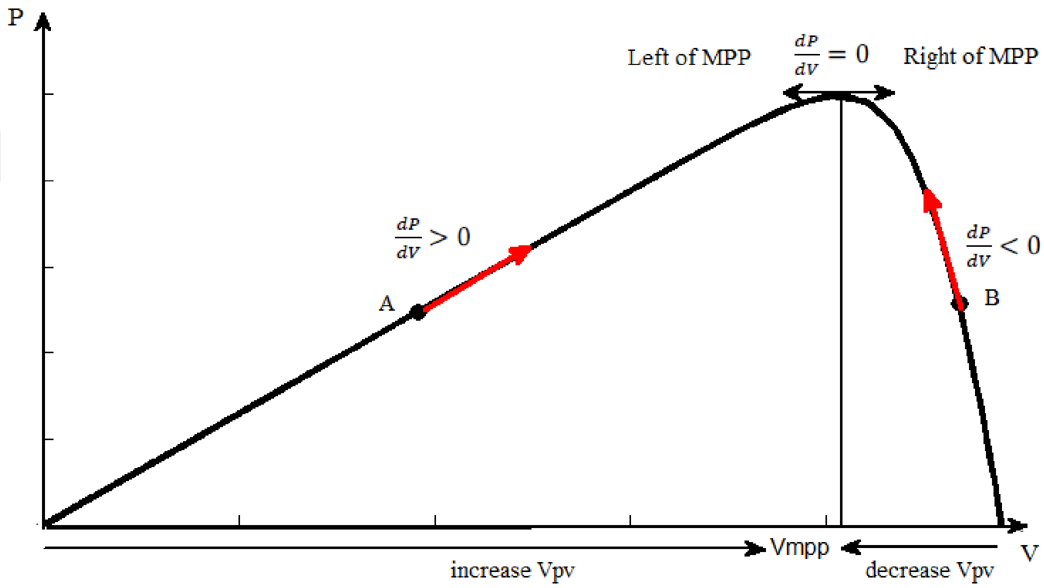

Figure 4.9. *P-V characteristic of Perturb and Observe algorithm (Yahdou et al., 2017)*

As can be seen from the graphic in Figure 4.10, Perturb and Observe technique; It works by perturbing the output voltage of the PV panel and then observing the change in output power. In this algorithm, the decrease or increase in power as a result of perturbing the voltage is determined by the position of the operating point according to the MPP and the perturb direction is determined according to the polarity of the output power (Figure 4.10). The next step is decided.

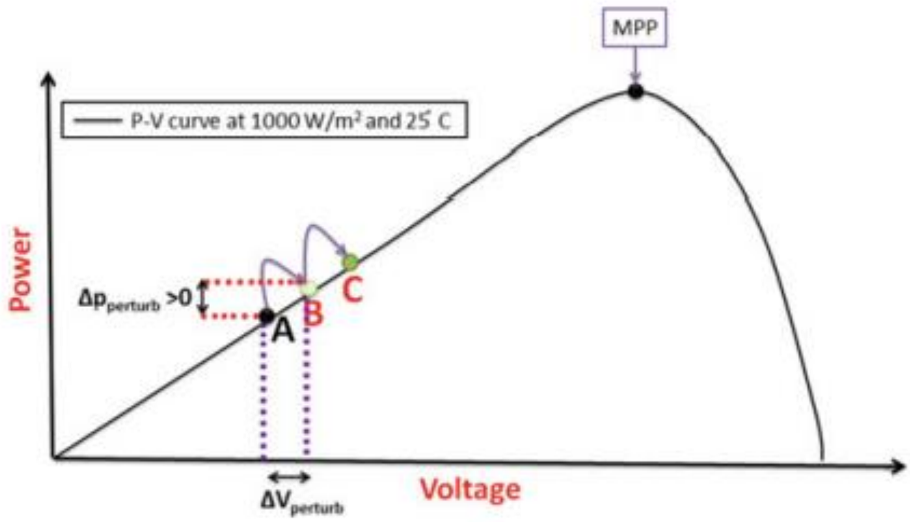

Figure 4.10. *Steps of the working point in the P&O algorithm (Abdel-Salam et al., 2020)*

Possible situations in the operation of the algorithm are listed below.

If the increase in voltage causes an increase in power when the algorithm perturbs during tracking, it means that the operating point is to the left of the MPP and the tracking direction is kept the same.

If the decrease in voltage causes a decrease in power when the P&O algorithm perturbs, the operating point is to the left of the MPP and the tracking direction is reversed.

When this algorithm perturbs, if the increase in voltage causes a decrease in power, it means that the operating point stays to the right of the MPP and the tracking direction is reversed.

When this algorithm perturbs, if the decrease in voltage causes an increase in power, it means that the operating point is to the right of the MPP and continue in the tracking direction.

The common reason for all these perturbs is their convergence to the MPP point. These evaluations can be made by observing a decrease on the left and an increase on the right of the MPP point on the P&O algorithm P-V graph. The same evaluations are made again in each variable condition. The increase or decrease in this voltage continues until $dP/dV = 0$. If $dP/dV = 0$ is found, MPP is found (Cristea et al., 2010; MacAlpine, 2014; Wu and Yu, 2018).

While each evaluation is made, each operation takes place within flowchart steps. The flowchart of the P&O algorithm is in Figure 4.11.

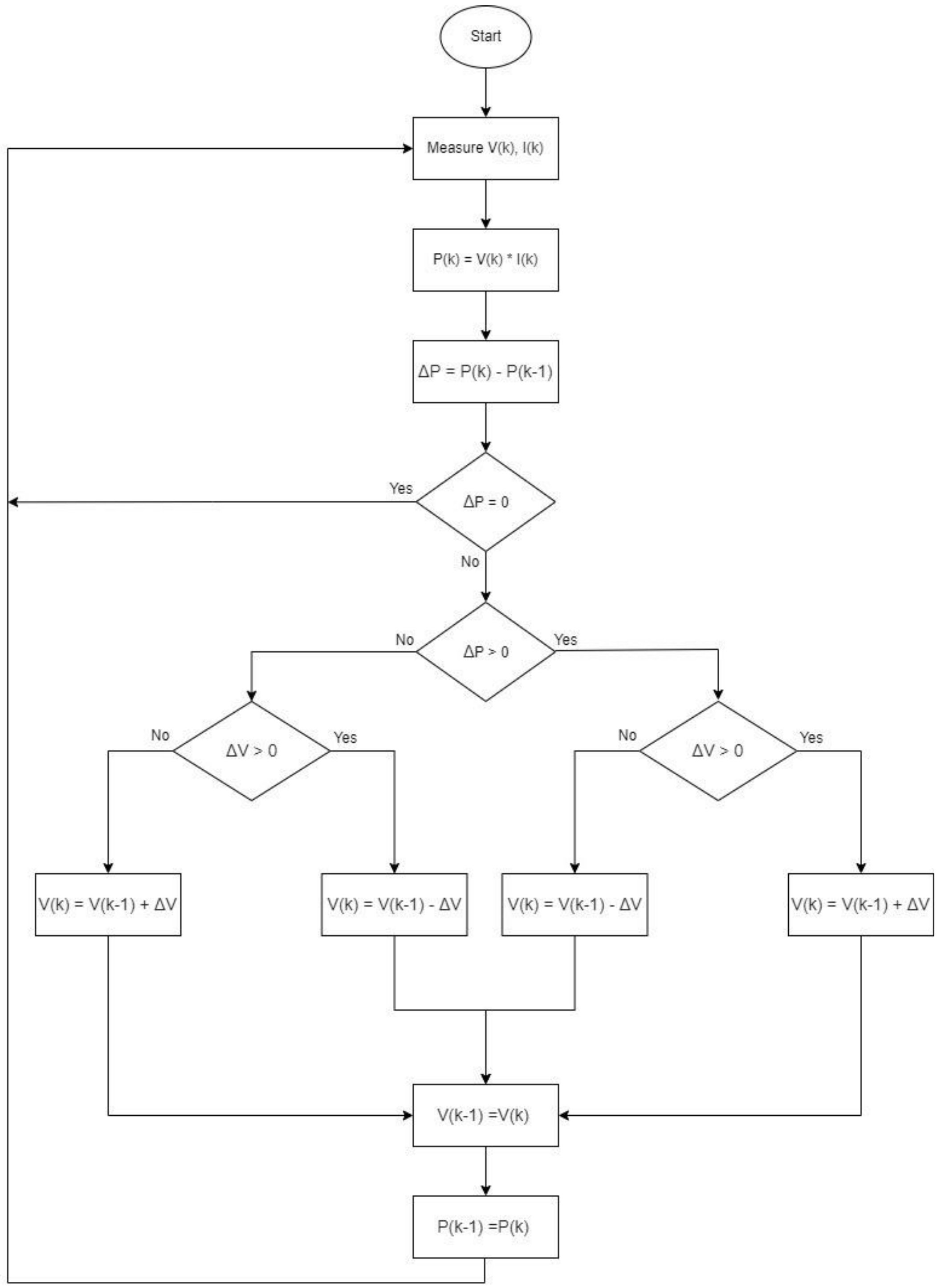

Figure 4.11. *The flowchart of P&O algorithm*

The working steps of the Perturb and Observe algorithm are listed. During operation, the progress step is determined according to the instant situation.

1. Step: The program starts running.
2. Step: Sampling is done to measure the output current and output voltage of the PV panel.
3. Step: The output power of the PV panel is calculated with the values measured in 2. step (Equation 4.1).

$$P\,(k) = V(k) * I(k) \tag{4.1}$$

4. Step: The calculated power value in 3. step is compared with the previous power value (Equation 4.2). The difference of these values is taken and expressed as ΔP.

$$\Delta P = P(k) - P(k-1) \tag{4.2}$$

5. Step: Whether the ΔP value calculated in the 4. step is equal to zero or not is evaluated (Equation 4.3). If ΔP = 0, MPP is reached. The loop returns to 2. step. Else, it proceed to 6. step.

$$\Delta P = 0 \tag{4.3}$$

6. Step: The polarity of the ΔP value, that is, whether it is greater than 0 or not, is evaluated. (Equation 4.4). In this case, two conditions are met. If ΔP > 0, it continues to Step 7. If ΔP > 0, it goes to 8. step.

$$\Delta P > 0 \tag{4.4}$$

7. Step: If ΔP is not > 0, the voltage value measured in 2. Step is compared with the previously calculated voltage value and the difference is taken. If the calculated value is greater than 0, it is evaluated (Equation 4.5). Two conditions occur as a result of this evaluation. if ΔV > 0. it goes to 7.2. step. Else, it continues to 7.1. step.

$$V(k) - V(k-1) > 0$$
$$\Delta V > 0 \tag{4.5}$$

7.1.Step: If ΔV is negative, the algorithm detects that the operating point is to the left of the MPP and the direction of advance is opposite from the MPP. So the next perturbation will be positive. In this case, the voltage is increased by increasing the duty cycle (Equation 4.6). It continues to 9. step.

$$V(k) = V(k-1) + \Delta V \quad (4.6)$$

7.2.Step: If ΔV is positive, the algorithm detects that the operating point MPP is on the right and the direction is opposite from the MPP. So the next perturbation will be negative. In this case, the duty cycle is reduced and the voltage is reduced (Equation 4.7). It continues to 9. step.

$$V(k) = V(k-1) - \Delta V \quad (4.7)$$

8. Step: If ΔP > 0, the voltage measured in 2. step and the ΔV value of the voltage in the previous perturbation are calculated. The ΔV polarity, that is, being greater than 0, is evaluated (Equation 4.5). Two conditions occur as a result of this evaluation. If ΔV > 0, it continues to 8.1. step. If ΔV > 0, it passes to 8.2. step.

8.1.Step: If the value of ΔV is negative, the algorithm detects that the operating point is to the left of the MPP and the direction is towards the MPP. So the next perturbation will be positive. In this case, the voltage is increased by increasing the duty cycle (Equation 4.7). It continues to 9. step.

8.2.Step: If the value of ΔV is positive, the algorithm detects that the operating point is on the right and the forward direction is towards the MPP. So the next perturbation will be negative. In this case, the voltage is reduced by reducing the duty cycle (Equation 4.6). It continues to 9. Step.

9. Step: The perturbation voltage is updated as the previous perturbation voltage (Equation 4.8).

$$\mathrm{V}(\mathrm{k}-1) = \mathrm{V}(\mathrm{k}) \quad (4.8)$$

10. Step: The power value, which varies depending on the voltage, is also updated as the previous perturbation power. The loop returns to 2. Step.

$$P(k-1) = P(k) \quad (4.9)$$

4.4.2. Incremental Conductance (InCond) algorithm

Incremental conductance algorithm is one of the most preferred MPPT algorithms with its fast MMP detection feature. This algorithm is also referred to as the InCond algorithm. It has a different working methodology compared to the Perturb and Observe algorithm. The InCond algorithm uses the P-V curve and the I-V curve to track the MPP point. Combining these curves allows the InCond algorithm to track MPP faster and more accurately. The technique of tracking this point is based on the slope calculated on the P-V curve (Xia, 2012; Ishaque, 2014). Figure 4.12 shows the operating principle of the InCond algorithm on the P-V and I-V curves.

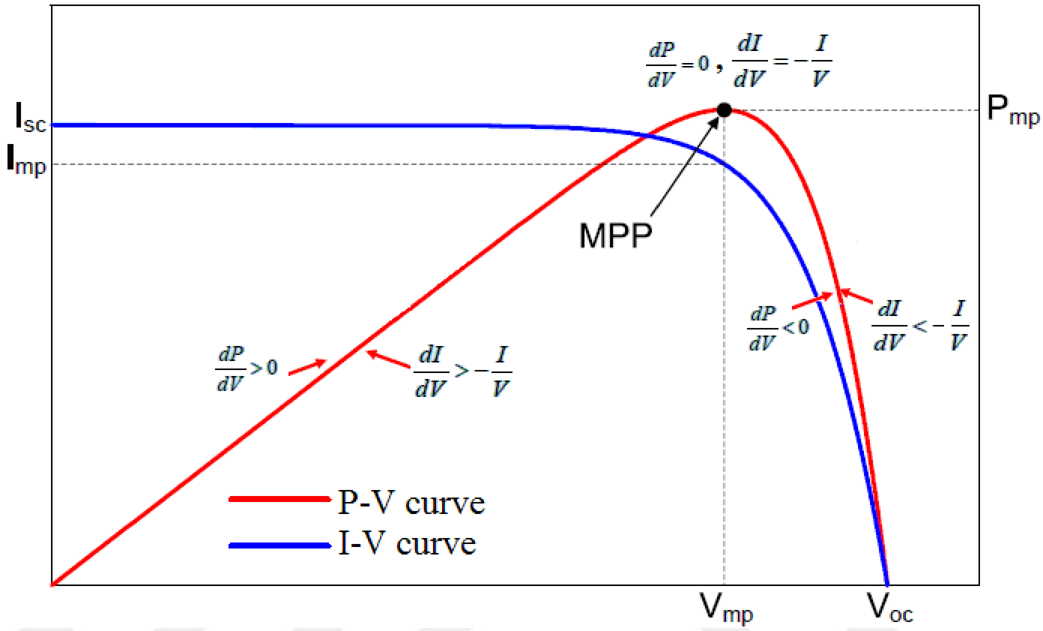

Figure 4.12. *The P-V and I-V characteristic of Incremental Conductance algorithm*

As can be seen from the expressions in Figure 4.12, the Incremental Conductance technique; It is based on the principle of comparing the ratio of the output current and output voltage of the PV panel with the rate of change in the current and voltage values compared to the previous operating point (Equation 4.12). The $\frac{dI}{dV}$ The dI/dV ratio and the slope of the InCond P-V curve are measured. And to find the MPP, it is continued until the slope is $\frac{dI}{dV}=0$ (Xia, 2012; Ishaque, 2014).

The mathematical calculation of this situation is as follows:

$$dV \cong \Delta V = V(k) - V(k-1)$$
$$dI \cong \Delta I = I(k) - I(k-1) \quad (4.10)$$

$$\frac{d\,(V,I)}{dV} = I + V * \frac{dI}{dV} = 0 \quad (4.11)$$

$$\frac{dI}{dV} \cong \frac{\Delta I}{\Delta V} = -\frac{I}{V} \quad (4.12)$$

Here; V is the voltage measured from the panel, I is the current measured from the panel, dI is the change in current compared to the previous loop, dV is the change in voltage compared to the previous loop.

In Equation 4.12, $\frac{I}{V}$ denotes conductance, while $\frac{\Delta I}{\Delta V}$ denotes incremental conductance.

First of all, the algorithm compares these two ratios and checks whether one ratio is larger or smaller than the other. As a result of the comparison of these ratios, the position of the operating point with respect to the MPP is determined and the direction of the next loop is decided according to its position. Using the equation in Equation 4.12, the position determined relative to the MPP is as follows (Equaiton 4.13):

$$\frac{\Delta I}{\Delta V} = -\frac{I}{V} \; ; indicates\ MPP$$
$$\frac{\Delta I}{\Delta V} > -\frac{I}{V} \; ; indicates\ the\ left\ side\ of\ MPP$$
$$\frac{\Delta I}{\Delta V} < -\frac{I}{V} \; ; indicates\ the\ right\ side\ of\ MPP \qquad (4.13)$$

While making each evaluation, each process takes place within the flowchart steps. The flowchart of the InCond algorithm is in Figure 4.13.

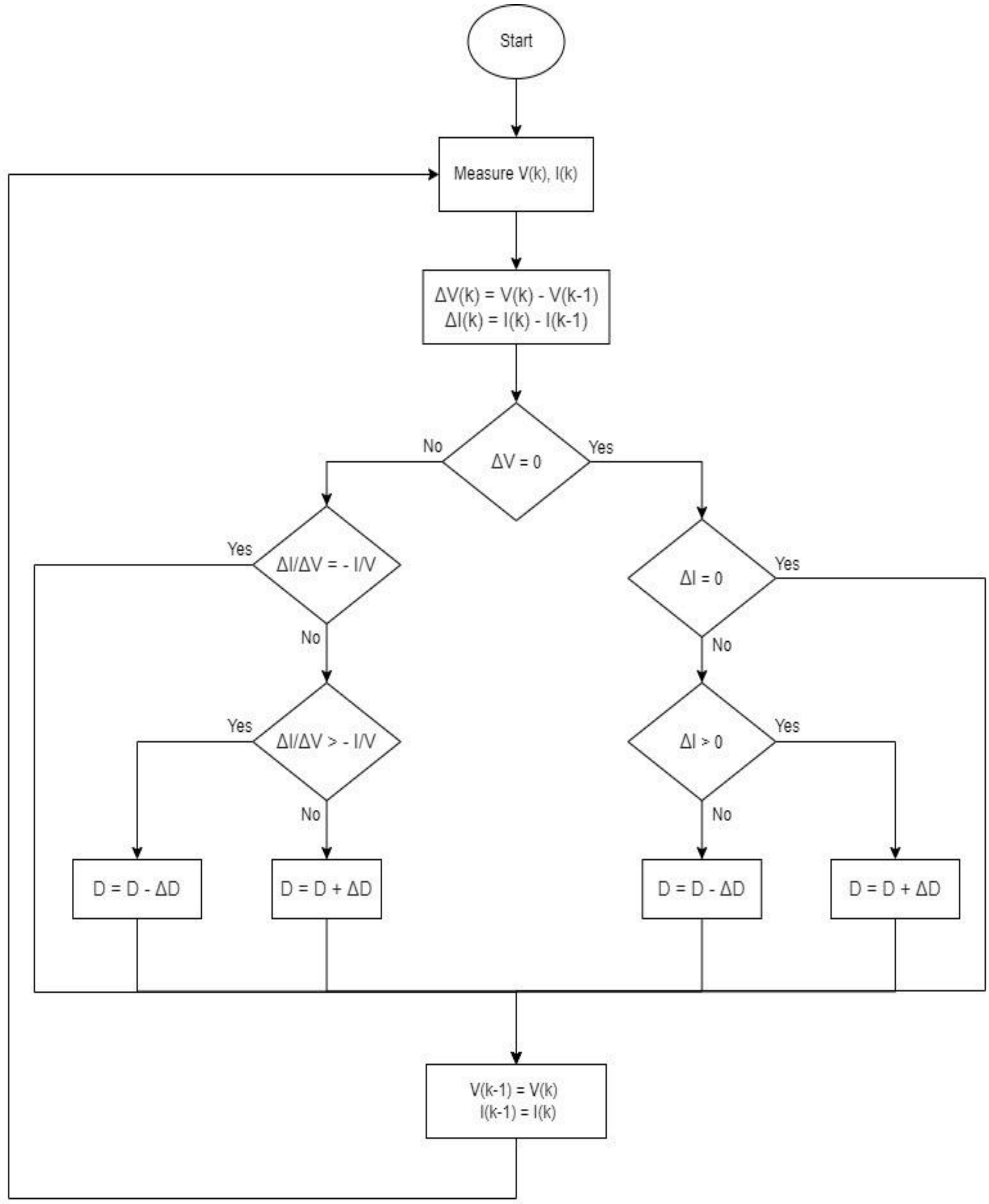

Figure 4.13. *The flowchart of Incremental Conductance algorithm*

The working steps of the Incremental Conductance algorithm are listed. During operation, the progress step is determined according to the instant situation.

1. Step: The program starts running.
2. Step: Sampling is done to measure the output current and output voltage of the PV panel.
3. Step: The current and voltage values from the PV panel are calculated as the difference between the current and voltage values from the previous InCond cycle. These are expressed as ΔI and ΔV, respectively (Equation 4.14).

$$\Delta V = V(k) - V(k-1)$$
$$\Delta I = I(k) - I(k-1) \tag{4.14}$$

4. Step: The equality of the voltage difference calculated in 3. step to 0 is evaluated (Equaiton 4.15). In this case, two conditions occur. If the voltage differential is not equal to 0, it continues to 5. step. If the voltage difference is equal to zero, it goes to 8. step.

$$\Delta V = 0 \tag{4.15}$$

5. Step: If ΔV≠0, conductance and incremental conductance are compared (Equation 4.16). There are two conditions depending on the situation if these situations are equal or not. If it is equal, it continues to 9. step directly with no change. Else, it continues to 6. step.

$$\frac{\Delta I}{\Delta V} = -\frac{I}{V} \tag{4.16}$$

6. Step: If $\frac{\Delta I}{\Delta V} \neq -\frac{I}{V}$, the conductance and incremental conductance are compared and the incremental conductance value is greater than the conductance value (Equation 4.17). In this case, there are two conditions. If incremental conductance value is greater than conductance value, the process continues to 6.1. step. Else, it continues to 6.2. step.

$$\frac{\Delta I}{\Delta V} > -\frac{I}{V} \tag{4.17}$$

6.1.Step: If $\frac{\Delta I}{\Delta V}$ is greater than $-\frac{I}{V}$, the duty cycle value in this cycle is reduced. This reduction value is the difference between the duty cycle value in the previous loop and the duty cycle value in this loop (Equation 4.18). Then the process continues to 9. step.

$$D(k) = D(k-1) - \Delta D \tag{4.18}$$

6.2.Step: If $\frac{\Delta I}{\Delta V}$ is not greater than $-\frac{I}{V}$, the duty cycle in this cycle is increased. This increment value is the difference between the duty cycle value in the previous loop and the duty cycle value in this loop. (Equation 4.19). Then the process continues to 9. Step.

$$D(k) = D(k-1) + \Delta D \tag{4.19}$$

7. Step: If $\Delta V = 0$, the difference between the current value in this loop and the previous current value is taken and expressed as ΔI. It is checked if this current difference is equal to 0 (Equation 4.20) and according to this situation, two conditions occur. If ΔI is equal to zero, it proceeds to 9. step without any change. Else, it continues to 8. step.

$$\Delta I = 0 \tag{4.20}$$

8. Step: If $\Delta I \neq 0$, the polarity of this difference value is evaluated (Equation 4.21). If ΔI is not greater than zero, it continues to 8.1. step. Else, it pass 8.2. stepe geçer.

$$\Delta I > 0 \tag{4.21}$$

8.1.Step: If ΔI is not greater than 0, the duty cycle in this loop is reduced. This reduction value is the difference between the duty cycle value in the previous loop and the duty cycle value in this loop (Equation 4.18). Then it continues to 9. Step.

8.2.Step: If ΔI is greater than 0, the duty cycle in this loop is increased. This increment value is the difference between the duty cycle value in the previous loop and the duty cycle value in this loop (Equation 4.19). Then it continues to 9. Step.

9. Step: The voltage and current values from the previous loop are updated with the voltage and current values from this loop (Equation 4.22). After updating, it returns to 2. Step.

$$\begin{gathered} V(k-1) = V(k) \\ I(k-1) = I(k) \end{gathered} \tag{4.22}$$

4.4.3. Hill Climbing algorithm

One of the most preferred algorithms due to its ease of implementation is the Hill Climbing Algorithm. The major advantage of this algorithm is that it can be implemented without the need for the values of the PV panel in the previous loop. dV and dI are not calculated in the flowchart of this algorithm. In addition, MPP tracking is reliable even if the irradiance value increases rapidly (Nguyen et al., 2020). The main purpose of the algorithm is to change the duty cycle to determine the change in power until the operating point reaches the MPP. Any small change in the duty cycle will affect the algorithm. It provides control by switching the MPPT PWM signal. In this way, the DC-DC converter performs the duty cycle change.

Another preferred way to make maximum use of the output power obtained from the PV panel is the curve created by associating the PV output power with the PWM duty cycle change (Esram and Chapman, 2007; Nguyen et al., 2020). Output and duty cycle curve of Hill Climbing Algorithm is given in Figure 4.14.

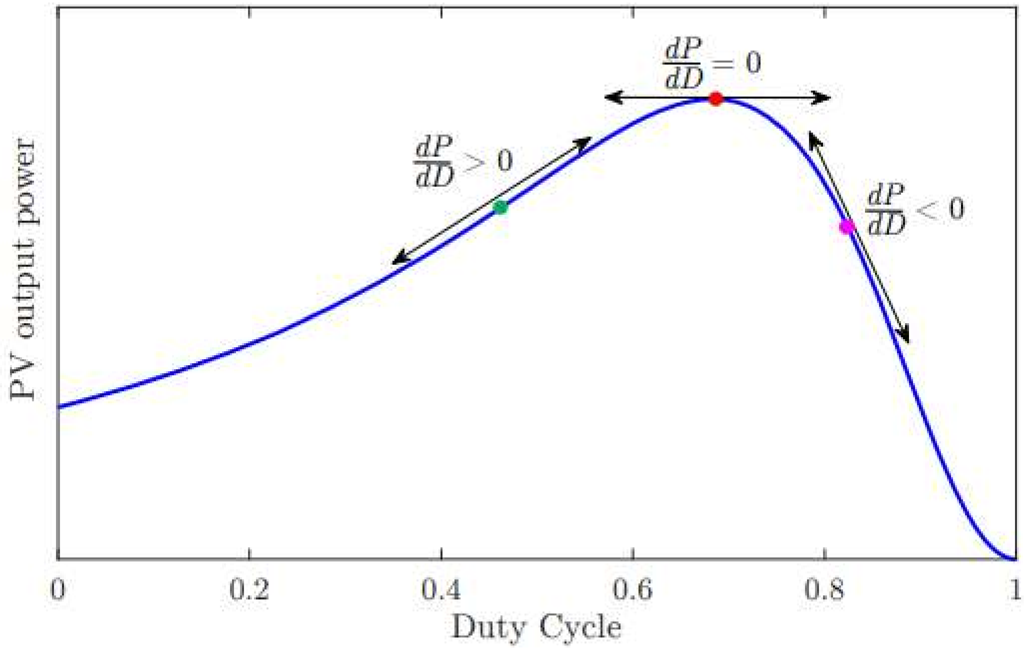

Figure 4.14. *The power-duty cycle curve of Hill Climbing algorithm (Nguyen et al., 2020)*

In Figure 4.14, there is a graph of PV output power corresponding to duty cycle values between 0 and 1. The possibilities that the algorithm may encounter during operation are:

If the Hill Climbing algorithm causes an increase in power when a positive change in the duty cycle is made during tracking, it means that the operating point remains to the left of the MPP and the tracking direction is kept the same.

If this algorithm causes a decrease in power when it makes a negative change in the duty cycle, it means that the operating point is to the left of the MPP and the tracking direction is reversed.

If this algorithm causes a decrease in power when it makes a positive change in the duty cycle, it means that the operating point stays to the right of the MPP and the tracking direction is reversed.

If this algorithm causes an increase in power when it makes a negative change in the duty cycle, it means that the operating point is to the right of the MPP and the tracking direction does not change.

Each loop is made to converge to the MPP. These evaluations can be made thanks to the decrease in the left and increase in the right of the MPP in the P-D graph of the Hill Climbing algorithm. The same evaluations are made again in each variable condition. This increase or decrease in duty cycle continues until $dP/dD = 0$. MPP is found when $dP/dD = 0$.

The flowchart of the Hill Climbing algorithm is given in Figure 4.15.

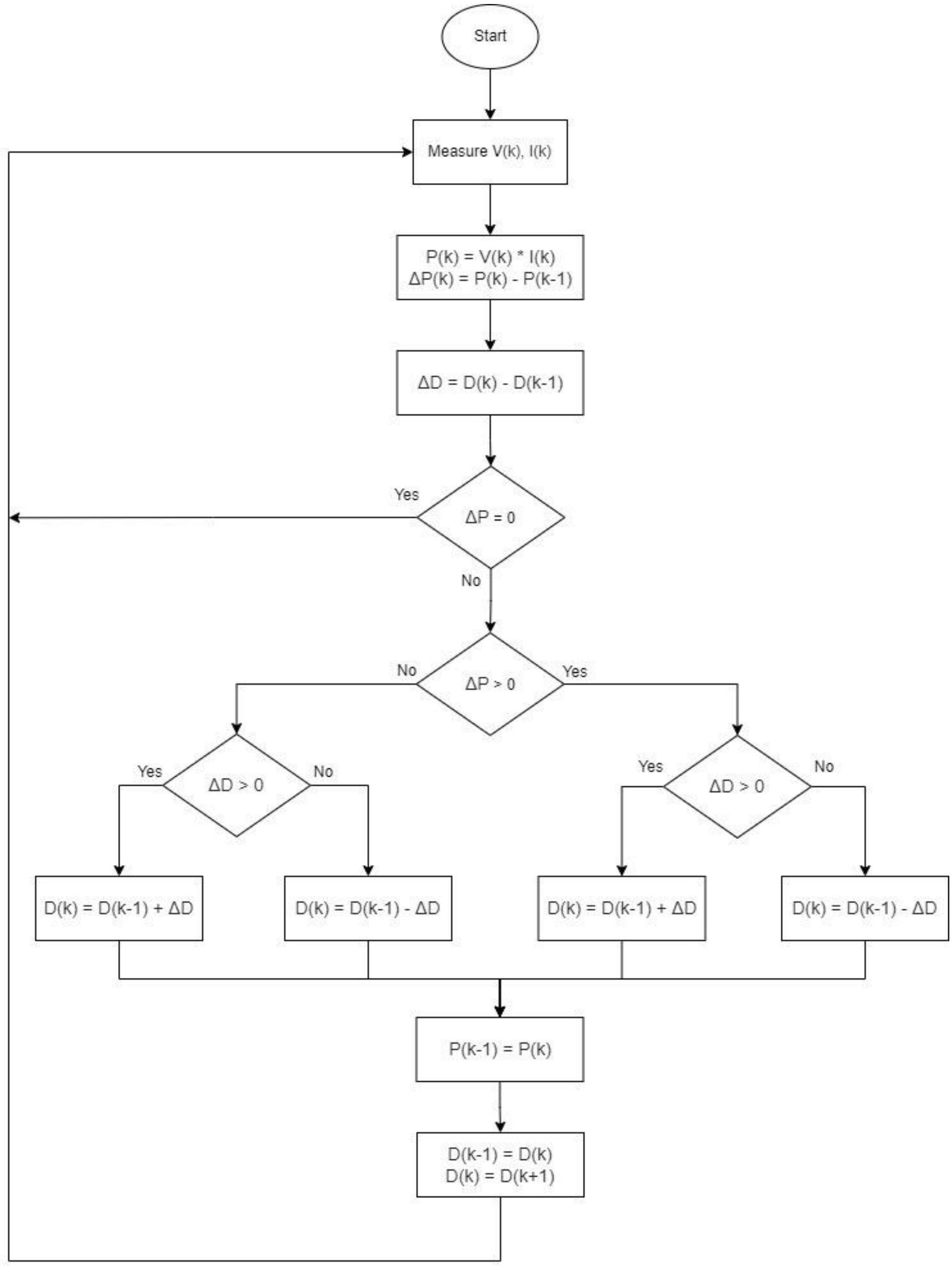

Figure 4.15. *The flowchart of Hill Climbing algorithm*

While making each evaluation, each process takes place within the flowchart steps.

1. Step: The program starts running.
2. Step: Sampling is done to measure the output current and output voltage of the PV panel.

3. Step: The output power of the PV panel is calculated with the values measured in 2. step (Equation 4.25) and the difference between the calculated power value and the previous power value is taken (Equation 4.26). These values are expressed with ΔP.

$$\mathrm{P}\,(\mathrm{k}) = \mathrm{V}(\mathrm{k}) * \mathrm{I}(\mathrm{k}) \tag{4.25}$$

$$\Delta\mathrm{P} = \mathrm{P}(\mathrm{k}) - \mathrm{P}(\mathrm{k}-1) \tag{4.26}$$

4. Step: The difference between the current duty cycle value of the algorithm and the previous duty cycle value is taken and these values are expressed with ΔD (Equation 4.27).

$$\Delta\mathrm{D} = \mathrm{D}(\mathrm{k}) - \mathrm{D}(\mathrm{k}-1) \tag{4.27}$$

5. Step: Whether the ΔP value calculated in Equation 4.26 is equal to zero is evaluated (Equation 4.28). If ΔP = 0, MPP is reached and the loop returns to Step 2. Else, it continues to 6. Step.

$$\Delta\mathrm{P} = 0 \tag{4.28}$$

6. Step: The polarity of the ΔP value, that is, whether it is greater than 0 or not, is evaluated (Equation 4.29). In this case, two conditions are met. If ΔP > 0, it continues to 7. Step. If ΔP > 0, it goes to 8. Step.

$$\Delta\mathrm{P} > 0 \tag{4.29}$$

7. Step: If ΔP is negative, the difference between the duty cycle value calculated in 4. step and the duty cycle value calculated in the previous cycle is taken. The polarity of the difference duty cycle values from 0 is evaluated (Equation 4.30). Two conditions occur as a result of this evaluation. If ΔD > 0, it continues to 7.1. step. Else, it continues to 7.2. step.

$$\Delta D > 0 \tag{4.30}$$

7.1.Step: If ΔD is positive, the algorithm detects that the operating point is to the left of the MPP and the direction is opposite from the MPP. That is, the next duty cycle value is increased (Equation 4.31). It continues to 9. Step.

$$D(k) = D(k-1) + \Delta\mathrm{D} \tag{4.31}$$

7.2.Step: If ΔD is negative, the algorithm detects that the operating point is to the right of the MPP and the direction is opposite from the MPP. In this case, the duty cycle value is reduced (Equation 4.32). It continues to 9. step.

$$D(k) = D(k-1) - \Delta D \tag{4.32}$$

8. Step: If ΔP > 0, the difference between the duty cycle values calculated in the 4. step and the previous cycle is taken. The polarity of the difference value is evaluated (Equation 4.30). Two conditions occur as a result of this evaluation. If ΔD > 0, it continues to 8.1. step. Else, it passes 8.2. step.

8.1.StepIf ΔD is positive, the algorithm detects that the operating point is to the left of the MPP and the direction is towards the MPP. In this case, the duty cycle is increased (Equation 4.31). It continues to 9. step.

8.2.Step: If ΔD is negative, the algorithm detects that the operating point is to the right of the MPPT and the direction is towards the MPP. In this case, the duty cycle is reduced (Equation 4.32). It continues to 9. step.

9. Step: The previous PV output power is updated with the PV output power calculated in 3. step (Equation 4.33).

$$\mathrm{P(k-1)} = \mathrm{P(k)} \tag{4.33}$$

10. Step: The previous duty cycle value is updated with the duty cycle value calculated in Step 4 and the duty cycle jumps to the next step (Equation 4.34). The loop returns to 2. step.

$$\begin{aligned} D(k-1) &= D(k) \\ D(k) &= D(k+1) \end{aligned} \tag{4.34}$$

The Hill Climbing Algorithm operating methodology is similar to the perturb and observe algorithm in terms of dP evaluation in the flowchart (Xiao, 2003; Liu et al., 2008). But the perturb and observe algorithm tracks the MPP with the ratio of power change to voltage change. Hill Climbing Algorithm references the ratio of change in power to change in duty cycle for tracking. In other words, the main feature that distinguishes the Hill Climbing algorithm from the P&O algorithm is that it uses the duty cycle value of the switching mode power interface.

5. SIMULATION AND RESULTS

The evaluation in the thesis was made by taking the DLR HAP-Alpha project as a reference and considering the features of the UAV used in this project. A model was created on MATLAB/Simulink to analyze the performance of the algorithms evaluated in the thesis. The model created on MATLAB/Simulink is in Figure 5.1. This section includes the PV system components and their features in this model. In order to evaluate the performance of each algorithm, a model for each algorithm has been designed.

Since the number of modules in one wing of the HAP-Alpha vehicle is odd, the system used for 1 PV module will be different. Since the number of PV modules connected to the circuit will change here, the current values of the PV panel in the circuit will be halved. This means that the current transmitted to the MPPT algorithm is halved.

The Perturb and Observe algorithm model, one of the designed MATLAB/Simulink models, is included in APPENDIX-1a. The model includes a power gui block, a bus, ramp signal builder, a PV array consisting of two modules, a boost converter, current measurement block, voltage measurement block, a MATLAB controller with a P&O algorithm, unit delays, sum block and PI (Proportional- Integral) Controller, repeating sequence block and load. The Powergui block in the model performs the calculation in the circuit. This block calculates in discrete mode. A bus is placed to measure the output voltage and current values of the PV panel. The ramp signal builder used creates irradiance and temperature signals for PV panels. In creating the PV array in the model, a solar cell based on ELO technology belonging to MicroLink company was used. The specification of this solar cell is in Table 5.1.

Table 5.1. *The specification of the PV cell*

Cell specification	Value
Area (cm^2)	20.1
I_{SC} (mA)	322.09
V_{OC} (V)	2.93
I_{MAX} (mA)	311.45
V_{MAX} (V)	2.59
P_{MAX} (P)	805.88
FF (%)	85.3
Eff (%)	29.3

The programming code of the P&O algorithm used in the designed model is included in APPENDIX-1b. PV voltages and currents are transmitted to the algorithm via unit delays. With the codes here, the maximum power point of the PV panel is found. The current from the P&O MATLAB controller proceeds through the sum and PI (Proportional-Integral) controller modules. It is then connected to the relation operation block with a repeating sequence. The output value of this block is transferred to the MOSFET of the Boost converter as a PWM signal. Thus, maximum power flow is provided for the load in the circuit.

The necessary calculations for the circuit are made with the sub-connections in the measurement module in APPENDIX-1a. Connections for the "Measurement" module are given in Figure 5.1.

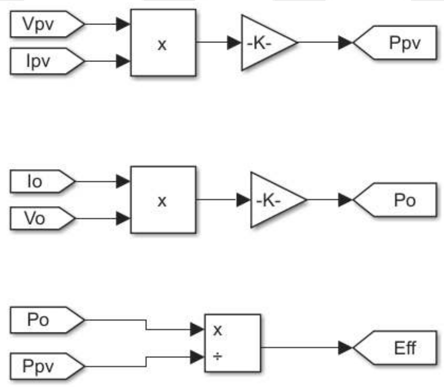

(a)

(b)

(c)

Figure 5.1. *Connections for 'measurement' module in the P&O MATLAB/Simulink model; (a) The power of PV panel, (b) The output power of the system, (c) The efficiency of the algorithm*

The MATLAB/Simulink model of the Incremental Conductance Algorithm is included in APPENDIX-2. The model includes a powergui block, a bus, ramp signal builder, a PV array, a boost converter, current measurement block, voltage measurement block, MATLAB controller with an InCond algorithm, PWM generator, and load.

On the other hand, a boost converter contains two capacitors, an inductor, a diode, and a MOSFET as a switching element. A PWM tag is connected to the MOSFET, which will transmit the signals from the InCond algorithm. The load has been added to the end of the Boost converter. To measure the current going to the load and the voltage generated, the current measurement block is connected to the circuit in series, and the voltage measurement block is connected in parallel.

In the designed model, the voltage and current values of the PV panel are transmitted to the boost converter and InCond MATLAB controller. The programming code of InCond MATLAB controller is in APPENDIX-2b. PV output voltages and currents are transmitted directly to the algorithm. With the codes here, the maximum power point of the PV panel is found. The value from the InCond MATLAB controller is transmitted to the PWM generator and transferred to the MOSFET of the Boost converter via the PWM generator. Thus, maximum power flow is provided for the load in the circuit.

The necessary calculations for the circuit are made with the sub-connections for the "measurement" module can be seen in APPENDIX-2a. Connections in the Measurement module are in Figure 5.1.

The MATLAB/Simulink model of Hill Climbing Algorithm, which is another of the designed models, is included in APPENDIX-3. The model includes a power gui block, a bus, ramp signal builder, a PV array, a boost converter, current measurement block, voltage measurement block, a MATLAB controller with a Hill Climbing algorithm, PWM generator, scopes, and load.

In the designed model, the voltage and current values of the PV panel are transmitted to the boost converter and Hill Climbing MATLAB controller. Programming codes of Hill Climbing MATLAB controller are in APPENDIX-3b. PV output voltages and currents are transmitted directly to the algorithm. With the codes here, the maximum power point of the PV panel is found. The value from the Hill Climbing MATLAB controller is transmitted to the PWM generator and transferred to the MOSFET of the Boost converter via the PWM generator. Thus, maximum power flow is provided for the load in the circuit.

The necessary calculations for the circuit are made with the sub-connections for the "measurement" module can be seen in APPENDIX-3a. The connections in the Measurement module are in Figure 5.1.

5.1. Model Inputs

In the designed models, some results were obtained by using the irradiance values specified in Table 3.1. These results formed the inputs of Perturb and Observe, Incremental Conductance, and Hill Climbing algorithms under the same conditions.

For MATLAB/Simulink modeling, three different altitude values were taken as reference. For the HAP Alpha UAV, 0 km, 5 km, and 25 km altitude values were taken as reference, and 12 different irradiance values, which vary depending on various factors at these altitudes, were used. Each irradiance value represents the average irradiance value for a month of the year.

The internal temperatures of the PV panels differ from the temperature that changes depending on the altitude. The heat change in these solar cells somewhat compensates for the negative effects of the extremely low temperature resulting from increasing altitude on the PV panels. In this case, the solar cell temperatures used in the UAV are calculated based on a NOCT (Nominal Operating Cell Temperature) value. NOCT is determined based on four basic parameters, which are standard. These parameters and values that are considered constant for NOCT are as follows;

- Irradiation on the solar cell = 800 W/m^2
- Wind velocity = 1 m/s
- Air temperature = 20°C.
- Inclination angle - from the horizontal = 45°

The typical module temperature for the solar cells NOCT used in the HAP Alpha UAV is assumed to be 48^o. The temperature of this solar panel was calculated according to the formula in Equation 5.1, taking into account the NOCT value.

$$T_S = T_A + (\left(\frac{NOCT-20}{80}\right) S) \quad (5.1)$$

Here, T_A is the ambient temperature where the panel is located, NOCT is the nominal operating cell temperature, S is irradiance (mW/cm^2), and T_S is the temperature of the solar cells.

The approximate solar cell temperature values calculated regarding the irradiance values given for HAP-Alpha in Table 3.1 are listed in Table 5.2. Equation 5.1 was used for this calculation.

Table 5.2. *Solar cells temperature of HAP Alpha corresponding to irradiance and ambient temperature values*

h=0 km at 15°C		h=5 km at -17.47°C		h=25 km at -51.6°C	
Irradiance (W/m^2)	**Solar Cells Temperature (°C)**	**Irradiance (W/m^2)**	**Solar Cells Temperature (°C)**	**Irradiance (W/m^2)**	**Solar Cells Temperature (°C)**
250	23.75	375	-4.6	500	-34.1
300	25.5	400	-3.7	550	-32.5
375	28.1	450	-1.99	575	-31.48
400	29	575	2.38	700	-27.1
450	30.7	625	4.13	775	-24.48
575	35.1	750	8.51	900	-20.1
650	37.7	800	10.2	975	-17.48
700	39.5	925	14.6	1100	-13.1
775	42.1	975	16.3	1150	-11.35
825	43.8	1000	17.2	1200	-9.6
850	44.7	1025	18.1	1225	-8.73
900	46.5	1050	19.1	1250	-7.85

5.2. Model Outputs

The result data of the Perturb and Observe algorithm, Incremental Conductance algorithm, and Hill Climbing algorithm models created in MATLAB/Simulink, taking into account the HAP Alpha UAV specifications, are included in this section. These results were compared considering the algorithm efficiency. The irradiance and solar cell temperature values in Table 5.2 were used as the input data of the PV panel in the designed models. The algorithm efficiencies of the UAV according to a specific flight altitude and ambient temperature values are discussed in separate tables. Model efficiencies of each algorithm under varying irradiance and solar cell temperature values were calculated using MATLAB R2021b.

The tests simulated for 0 km altitude according to the reference altitudes for the HAP Alpha flight are evaluated under the sections of 'Ground level test results', the tests simulated at 5 km altitude 'Low altitude test results', and the simulated tests at 25 km altitude 'High altitude test results'.

5.2.1. Ground level test results

For the ground-level simulation test of the HAP Alpha UAV, the altitude is assumed as 0 km, and the ambient temperature as 15ºC. In this case, the irradiance and solar cell values that the PV array will be exposed to in the P&O, InCond, and Hill Climbing models in APPENDIX-1a, APPENDIX-2a, and APPENDIX -3a are indicated as system input in Table 5.3. During the simulation test carried out with reference to the ground level, the PV output values formed depending on the PV panel input were used in the programming codes in APPENDIX-1b, APPENDIX-2b, and APPENDIX-3b. This has enabled the system to run at maximum power, and the ability of the algorithms to track the MPP point can be evaluated. Table 5.3 shows the P&O Algorithm, InCond Algorithm, and Hill Climbing Algorithm efficiencies under the same conditions.

Table 5.3. *Efficiencies of ground-level P&O, InCond and Hill Climbing models*

h = 0 km at 15ºC				
System Input		**Algorithm Efficiency**		
Irradiance (W/m²)	**Solar Cell Temperature (ºC)**	**P&O Algorithm**	**InCond Algorithm**	**Hill Climbing Algorithm**
250	23.75	96.63	96.42	93.37
300	25.5	97.15	97.05	94.38
375	28.1	97.64	97.47	95.24
400	29	97.84	97.77	95.91
450	30.7	98.09	98.03	96.31
575	35.1	98.32	98.2	97.49
650	37.7	98.41	98.49	98.65
700	39.5	98.44	98.59	98.64
775	42.1	98.52	98.61	98.76
825	43.8	98.55	98.94	98.82
850	44.7	98.56	99.51	99.06
900	46.5	98.59	99.68	99.41

5.2.2. Low altitude test results

For the low altitude simulation test of the HAP Alpha UAV, the altitude is assumed to be 5 km, and the ambient temperature -17.47ºC. In this case, the irradiance and solar cells values that the PV array will be exposed to using the P&O, InCond, and Hill Climbing models in APPENDIX-1a, APPENDIX-2a, and APPENDIX -3a are indicated as system input in Table 5.4. During the flight at an altitude of 5 km, the PV output values formed depending on the PV panel input are used in the programming code in APPENDIX-1b, APPENDIX-2b, and APPENDIX-3b. This has enabled the system to run at maximum power, and the ability of the algorithms to track the MPP point can be evaluated. Table 5.4 shows the P&O Algorithm, InCond Algorithm, and Hill Climbing Algorithm efficiencies under the same conditions.

Table 5.4. *Efficiencies of P&O, InCond and Hill Climbing models at low altitude*

h = 5 km at -17.47°C				
System Input		**Algorithm Efficiency**		
Irradiance (W/m²)	**Solar Cell Temperature (°C)**	**P&O Algorithm**	**InCond Algorithm**	**Hill Climbing Algorithm**
375	-4.6	97.63	97.73	96.36
400	-3.7	97.73	97.87	97.22
450	-1.99	97.97	98.01	96.52
575	2.38	98.11	98.25	97.76
625	4.13	98.49	98.42	97.97
750	8.51	98.68	98.73	97.87
800	10.2	98.86	98.82	98
925	14.6	98.92	98.85	98.38
975	16.3	98.94	99.06	99.23
1000	17.2	98.98	99.11	99.55
1025	18.1	99.02	99.39	99.31
1050	19.1	99.03	99.5	99.63

5.2.3. High altitude test results

For the high-altitude simulation test of the HAP Alpha UAV, the altitude is assumed to be 25 km and the ambient temperature to be -51.6°C. In this case, the irradiance and solar cells values that the PV array will be exposed to using the P&O, InCond, and Hill Climbing models in APPENDIX-1a, APPENDIX-2a, and APPENDIX -3a are indicated as system input in Table 5.4. The PV array output values, which are formed depending on the PV panel input during the flight at an altitude of 25 km, are used in the programming code in APPENDIX-1b, APPENDIX-2b, and APPENDIX-3b. This has enabled the system to run at maximum power, and the ability of the algorithms to track the MPP point can be evaluated. Table 5.5 shows the P&O Algorithm, InCond Algorithm, and Hill Climbing Algorithm efficiencies under the same conditions.

Table 5.5. *Efficiencies of P&O, InCond and Hill Climbing models at high altitude*

h = 25 km at -51.6°C				
System Input		**Algorithm Efficiency**		
Irradiance (W/m²)	**Solar Cell Temperature (°C)**	**P&O Algorithm**	**InCond Algorithm**	**Hill Climbing Algorithm**
500	-34.1	98.11	98.09	97.27
550	-32.5	98.29	98.15	97.56
575	-31.48	98.33	98.25	98.05
700	-27.1	98.53	98.61	98.54
775	-24.48	98.73	98.75	98.76
900	-20.1	98.9	98.86	99.05
975	-17.48	99.03	98.96	99.18
1100	-13.1	99.13	99.09	99.21
1150	-11.35	99.17	99.18	99.07
1200	-9.6	99.18	99.27	99.19
1225	-8.73	99.19	98.61	98.34
1250	-7.85	98.21	98.65	98.36

Perturb and Observe algorithm, Incremental Conductance Algorithm, and Hill Climbing Algorithm models were run at three different altitudes and environmental temperature values. The efficiency values obtained from the studies are shown in 3 different tables depending on the altitude and environmental temperature values. As shown in Table 5.2, Table 5.3, and Table 5.4, algorithms were compared according to irradiance and solar cell temperature values. The highest tracking efficiency value of different algorithms running under the same conditions is illustrated in green.

5.3. Results

The algorithm efficiencies obtained in Section 5.2 are given in Figure 5.2, Figure 5.3 and Figure 5.4.

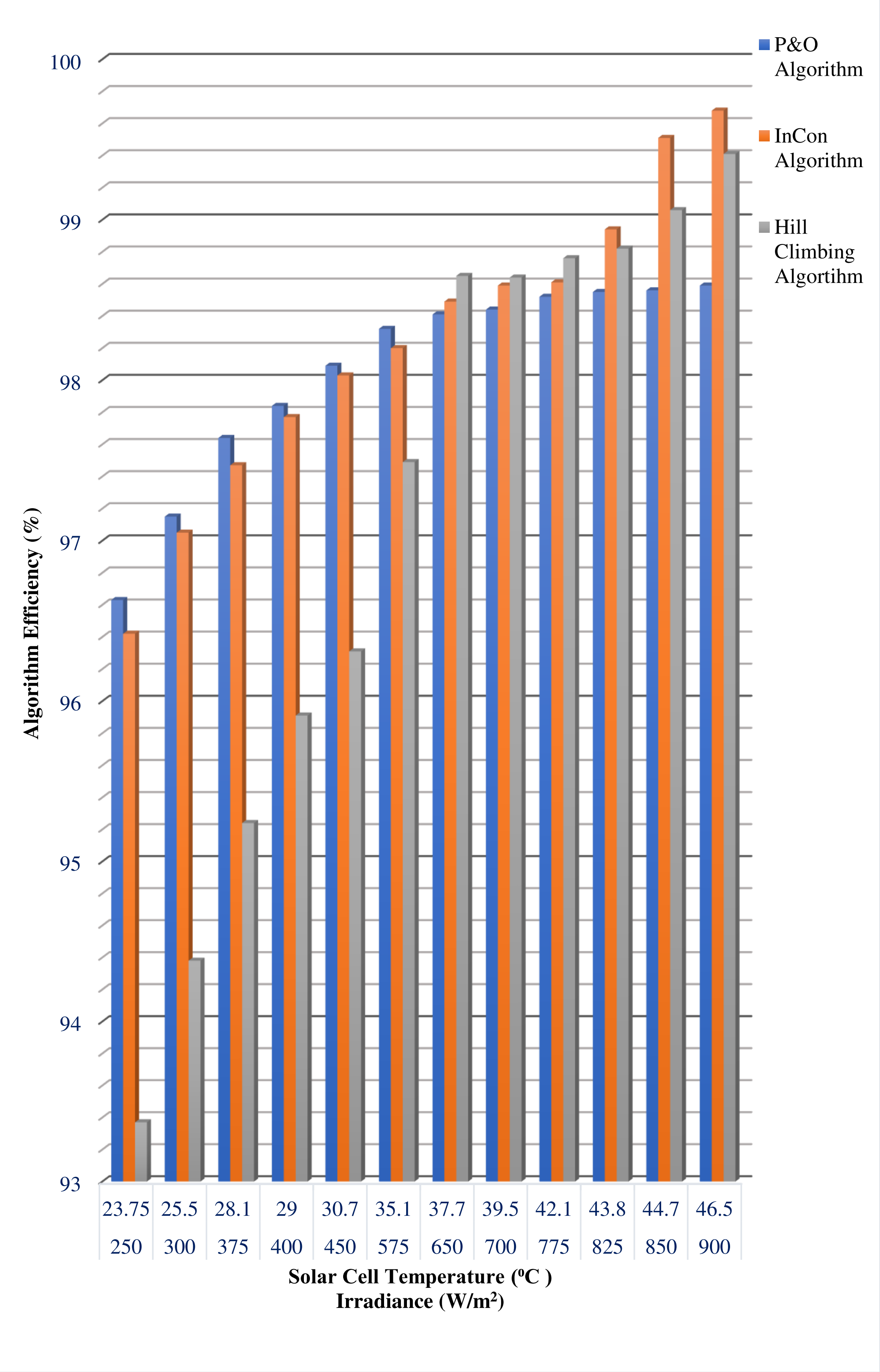

Figure 5.2. *Comparison of different algorithm's efficiencies at 0 km altitude and 15ºC ambient temperature*

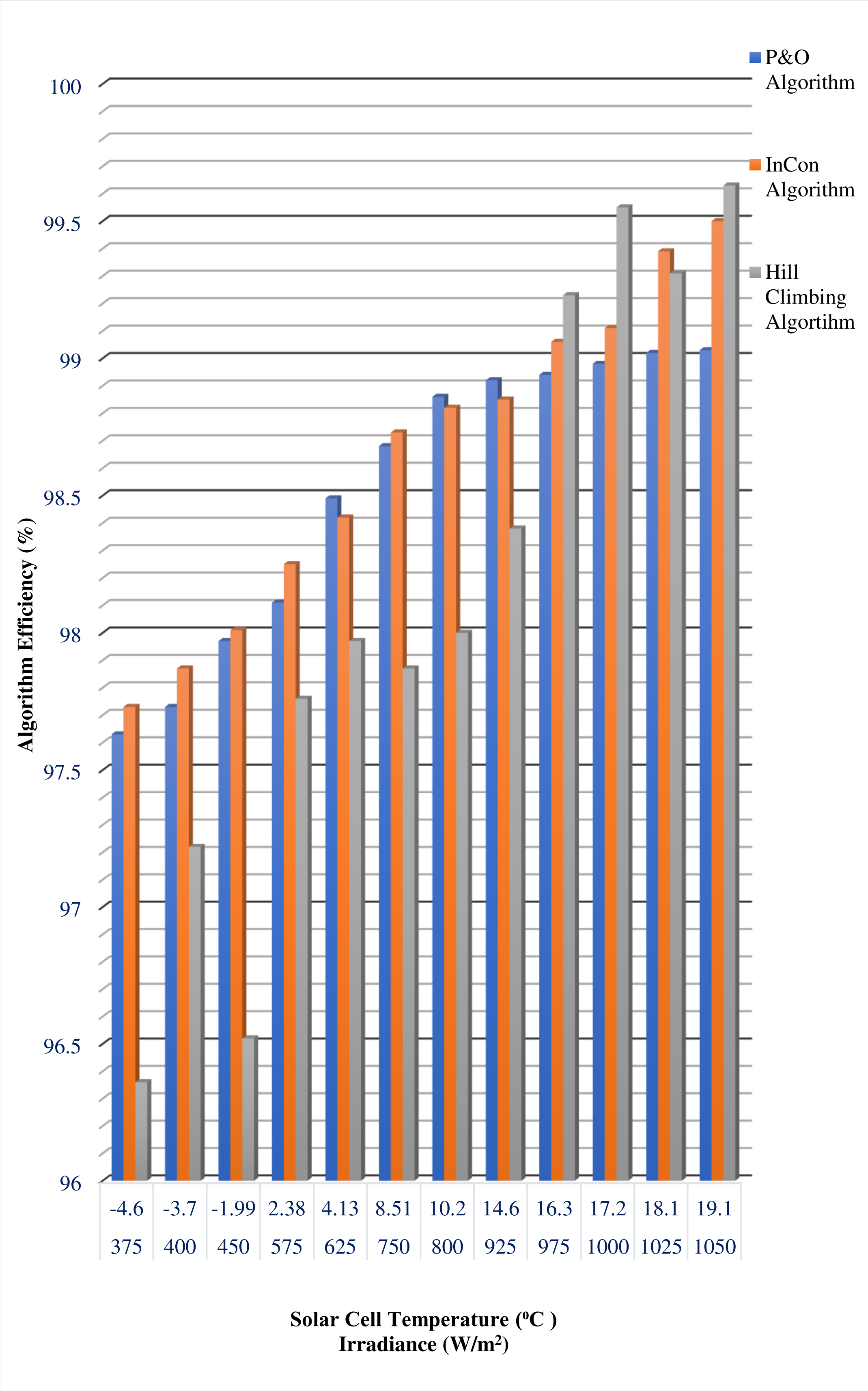

Figure 5.3. *Comparison of the different algorithm's efficiencies at 5 km altitude and -17.46⁰C ambient temperature*

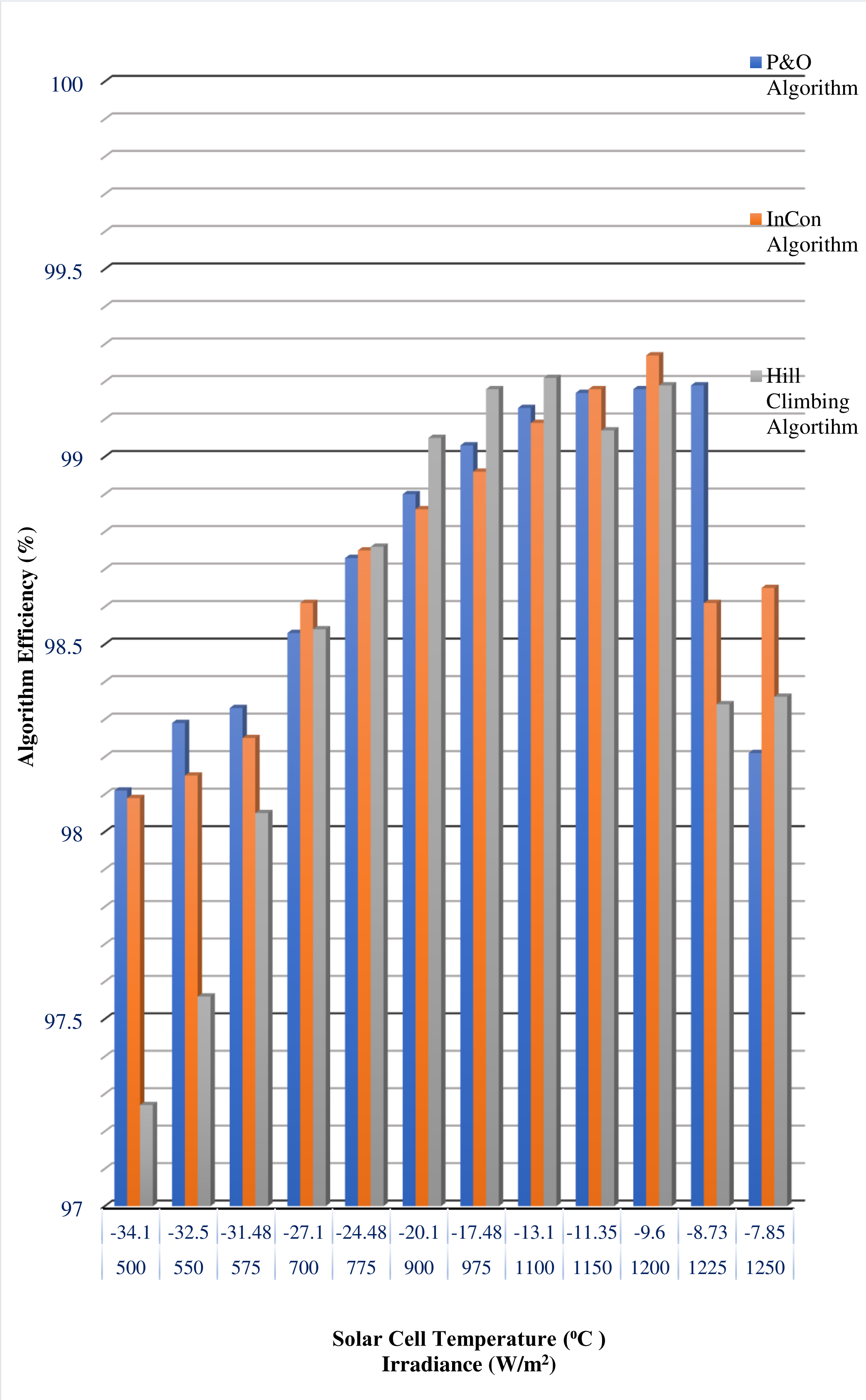

Figure 5.4. *Comparison of the different algorithm's efficiencies at 25 km altitude and -51.6ºC ambient temperature*

The comparison of the data obtained from the study was made using three different graphics. Algorithm efficiencies in each altitude-dependent irradiance (W/m^2) and solar cell temperature (^{0}C) are shown in the bar graph. The blue box in the graph represents the Perturb and Observe algorithm, the orange box represents the Incremental Conductance algorithm, and the grey box represents the Hill-Climbing algorithm. In the two conditions mentioned, by comparing the boxes of the three algorithms, it can be decided what is the most efficient algorithm in that condition.

5.3.1. Performance evaluation of MPPT algorithms

According to some studies, it has been seen that the efficiency of P&O and InCond algorithms is higher when compared to other traditional algorithms. When evaluated in terms of performance, it was seen that P&O and InCond performed at least as much as or higher than traditional algorithms (Hohm and Ropp, 2003; Jeddi and Ouni; 2014).

In the model created with reference to the technical features of the HAP-Alpha UAV, the operating performances of the MPPT, which is used to track the MPP point of the PV panel, were evaluated under three different algorithms. Models including Perturb and Observe, Incremental Conductance, and Hill Climbing algorithms may behave differently depending on the conditions they are exposed to during operation. In the designed models, each algorithm is evaluated with an irradiance and a certain solar cell temperature value. As a result of the evaluation, efficiency comparisons are made according to the performance of the models.

In addition, the oscillation state, which is considered neither the input nor the output of the model, is a negative factor that plays a critical role in the performance of algorithms. Since the formation of this oscillation situation causes a decrease in algorithm performance, it is an undesirable situation to be seen in the modeling. Therefore, it is necessary to examine the algorithms according to the oscillation state they create in the signals.

The performance evaluations of the P&O, InCond and Hill Climbing algorithms used as MPPT techniques in the models during the study of the designed models in the context of the oscillation state are as follows:

When the efficiency of the Perturb and observe algorithm is simulated under ground level and 15^{0}C ambient temperature, each irradiance and solar cell temperature change causes a fluctuation at the start time. Since this fluctuation occurs as a half period, it is negligible. When the oscillation is evaluated in terms of operating conditions, the tracking efficiency of the algorithm decreases at an increase after -35.1ºC temperature and 575W/m^2 irradiance value, which is affected by fluctuations in output power along with increasing temperature and irradiance. In this case, a few negligible oscillations take place. The output power of the system, on the other hand, has a lower level of oscillation compared to other altitude values. When the input values of the PV panel increase, there is also a small increase in the oscillation values.

While performing MPP tracking at 5 km altitude, which is called low altitude, and at a temperature of -17.46 ºC in the working of the P&O algorithm, low performance occurs under low irradiance and temperature values according to the changing PV panel input values, and oscillation in efficiency is observed. In addition, during the irradiance and temperature changes, a half-period oscillation wave is observed in efficiency. It is seen that the values obtained by running the model oscillate in efficiency at -4.6ºC, 16.3ºC and 17.2ºC temperatures at 5 km altitude and at 375W/m^2, 975W/m^2 and 1000W/m^2 irradiance values, respectively. The oscillation in the output power of the system also increases with the increase of temperature and irradiance.

When the P&O algorithm is operated at 25 km altitude, called high altitude, and at a temperature of -17.46ºC, it is observed that an instantaneous half-period oscillation wave occurs in efficiency. But unlike the other conditions, at -34.1ºC solar cell temperature and 575W/m^2 irradiance values, high amplitude half-wave oscillation takes place at the start of operation. It is also observed that there is negligible oscillation at -31.48ºC and 575W/m^2 irradiance values during operation. In terms of performance, although there is an increase in efficiency with the increase in irradiance and temperature, there is a decrease in performance under the 3 highest irradiance values. In the system output power, however, the oscillation changes in proportion to the increase in irradiance and temperature.

When the Incremental Conductance algorithm is simulated at ground level and under a temperature of 15ºC, no oscillation is observed at any point of the signal that shows the algorithm efficiency. The overall tracking performance, on the other hand, decreases with increasing irradiance and temperature. In the output power of the model, however, the oscillation is stably seen at a certain amplitude. Depending on the PV input parameters, no change is observed in the oscillation state.

When the InCond algorithm is simulated at a low altitude of 5 km and a temperature of -17.46 ºC, no oscillation is encountered. Its efficiency increases as irradiance and cell temperature increase. In the output power, as in the ground level, the oscillation level is at a certain amplitude and there is no increase or decrease in the oscillation level according to the PV input values.

When the InCond algorithm is run at an altitude of 25 km, called high altitude, and at a temperature of -17.46ºC, a few negligible oscillation waves occur only when the cell temperature is -9.6ºC and the efficiency signal is 1200 W/m^2 irradiance. Considering the general operating efficiency, although the efficiency decreases after -34.1ºC cell temperature and 500 W/m^2 irradiance value, the efficiency level increases with the increase in input values. As in other altitude values, the oscillation occurs at a constant amplitude in the output power.

When the Hill-Climbing algorithm is run at ground level and under 15ºC, the efficiency signal oscillates between 25.5ºC solar cell temperature and 300W/m^2 to 30.7ºC solar cell temperature and 450 W/m^2. In addition, when operating at 35.1ºC solar cell temperature and 575W/m^2 values, a short-term oscillation is observed at the start. Although an increase is observed in overall efficiency up to 37.7ºC and 650 W/m^2 in efficiency, a decrease occurs after these input values. An increase in the oscillation level in the system output power is observed with the increase in the PV input values.

When the Hill-Climbing algorithm runs at 5 km altitude, which is called low altitude, and at a temperature of -17.46ºC, oscillation is observed at -1.99ºC solar cell temperature and 450W/m^2 conditions. In addition, when operating under 4.13ºC and 625W/m^2 values, a short-term oscillation is observed at the start. In terms of efficiency, an increase in efficiency is observed up to 8.51ºC and 750W/m^2 values, but at higher irradiance values after this value, the efficiency increases or decreases differs; it does not vary linearly. In the system output power, an increase is observed in the oscillation level with an increase in the PV input values.

When the Hill-Climbing algorithm is run at 25 km altitude, called high altitude, and under a temperature of -17.46ºC, a short-term oscillation occurs at the initial moments when the input values are -27.1ºC and 700W/m^2 and -24.48ºC and 775W/m^2. In addition, it is observed that there is an oscillation in the efficiency signal when operating at -20.1ºC and 900W/m^2 values. It is not possible to make an assessment of the overall efficiency of the system. As soon as it shows an increase and decreases according to the irradiance and temperature value, each PV shows different behavior in the input values. The oscillation seen in the output power of the system increases with increasing input values.

The MPPT algorithms used in the designed model were evaluated according to the oscillations occurring in output and efficiency at different altitude values.

If the algorithms are compared according to the oscillation states at all altitudes, the algorithm with the most oscillation states is the Hill-Climbing algorithm. In addition, the algorithm with the lowest oscillation in all altitude values is the Incremental Conductance algorithm. It is seen that P&O and InCond algorithms show high performance in terms of running performance in all conditions. If a performance evaluation is made between these two algorithms, it is seen that the performance of the InCond algorithm is higher especially at low irradiance values, but the efficiency of the two algorithms is close to each other. It is seen that the InCond algorithm performs well in terms of rise time and dynamic response. The evaluation of 3 algorithms in tracking time is related to step size. If the algorithm's ability to track the MPP is evaluated as steps of two different sizes, the use of large step size results in high response speed, and the use of a small step size provides a more reliable result. However, if the three algorithms are run under the same conditions, the Hill-Climbing algorithm finds MPP faster in less tracking time than other algorithms because its structure is simpler. In addition, the oscillation problem in the use of the Hill-Climbing algorithm also affects the tracking speed.

6. CONCLUSION, DISCUSSION AND SUGGESTIONS

In this thesis, considering the flight conditions of the high-altitude unmanned aerial vehicle designed in the DLR HAP-Alpha project, 3 conventional MPPT algorithm modeling was used and the efficiency of the models was calculated. Algorithm models are designed using MATLAB/Simulink. The purpose of this study is to provide appropriate charge values for the batteries by evaluating the ability of the algorithms to track the maximum power obtained from the PV panel under variable conditions.

6.1. Conclusion

In order to create these models, the flight conditions of the HAP-Alpha UAV were examined and the basic parameters affecting the algorithm performance were determined and calculated.

In order to develop this system, first of all, solar powered UAVs and HALE background studies made within the scope of DLR were mentioned. Afterwards, solar powered UAV technologies are examined and general information about solar cell, DC-DC converter, battery technologies is given in this topic.

In the next chapter, the referenced HAP Alpha project is examined in detail. Technical information, purpose and target of the HAP-Alpha UAV, solar cell design, battery technologies, payloads used in the UAV are given. In addition, detailed information is given about the MPPT system used on the UAV, the PV module design on the wing and the MPPT connection design.

Afterwards, detailed information about the maximum power point tracking (MPPT) system is given. The operating structure and benefits of the MPPT system are mentioned. An evaluation has been made about the irradiance and temperature conditions that affect the operation of the MPPT system. Three traditional algorithms critical to MPPT are explained in detail with flowcharts.

Finally, MPPT algorithms are modeled in MATLAB/Simulink. In this study, the input values of the algorithm models designed for the HAP Alpha UAV were created and the output values were calculated. The working efficiency of the models was evaluated. The models were simulated according to the ground level, low altitude and high altitude conditions of the UAV according to the flight altitude, and the efficiency of the three algorithms used in these models were obtained.

The most preferred MPPT algorithms were simulated and their efficiency was compared. As a result of this comparison, the most suitable algorithm for the flight profile was determined. In this way, it is ensured that the batteries, which play a critical role especially for the solar powered UAV that makes long flights, are charged in a healthier way.

6.2. Discussion

The irradiance value, which is one of the inputs of the modeling, varies depending on many variables. Although the closest values are obtained in the thesis study, they may differ according to the flight conditions under real conditions. The results to be obtained vary depending on many parameters such as altitude, latitude, day of the year, time of day, season, and weather conditions. Depending on these parameters, the sun rays arriving at the earth from the sun can hit the location of the UAV at the time of flight with different values, together with atmospheric effects. It is necessary to obtain the most precise irradiance values by real flight test. This has been achieved theoretically as it is not currently possible within the scope of the project.

As seen in Table 5.3, numerical values are listed based on the irradiance values obtained from the flight tests previously performed by DLR. In addition, although the solar cell temperature value, which is another input, can be calculated as possible theoretical values, these temperature values can also vary depending on the flight conditions and the time the solar cells are exposed to sunlight.

6.3. Scope for future studies

Algorithm models developed in this study were simulated on the computer program, and the results were obtained theoretically. The models running under the controllable conditions give results within the expected values.

Real-life flight conditions, on the other hand, are not constant. It is variable, and sudden changes can be seen. In this case, the efficiency of the algorithms used may result contrary to what was predicted. Therefore, this study can be tested in real conditions. The running efficiency of the created models can be evaluated by comparing them with real-life and simulated conditions.

REFERENCES

Abbe, G. and Smith, H. (2016). Technological development trends in Solar-powered Aircraft Systems. *Renewable and Sustainable Energy Reviews*, 60, 770-783.

Abdel-Salam M., EL-Mohandes M. and Goda M. (2018). An improved perturb-and-observe based MPPT method for PV systems under varying irradiation level. *Solar Energy,* 171:547–561.

Abdel-Salam, M., EL-Mohandes, M. T., and Goda, M. (2020). On the Improvements of Perturb-and-Observe-Based MPPT in PV Systems. *In Modern Maximum Power Point Tracking Techniques for Photovoltaic Energy Systems* (pp. 165-198). Springer, Cham

Abouelela, M. (2020). Power Electronics for practical implementation of PV MPPT. *In Modern Maximum Power Point Tracking Techniques for Photovoltaic Energy Systems* (pp. 65-105). Springer, Cham.

Ackermann, D., Bierig, A., and Reininghaus, N. (2021, July). Modeling Spectrum Dependent Characteristics of Triple Junction Solar Cells for Solar-Powered Aircraft. *In 2021 Annual Modeling and Simulation Conference (ANNSIM)* (pp. 1-12). IEEE.

AlShemmary, E. N. A., Kadhom, L. M., and Al-Fahham, W. J. (2013). Information technology and stand-alone solar systems in tertiary institutions. *Energy Procedia*, 36, 369-379, doi: 10.1016/j.egypro.2013.07.042.

Atia, D. M. (2020). Global maximum power point tracking-based computational intelligence techniques. *Modern maximum power point tracking techniques for photovoltaic energy systems*, 131-163.

Baharudin, N. H., Mansur, T. M. N. T., Hamid, F. A., Ali, R., and Misrun, M. I. (2018, June). Performance analysis of DC-DC buck converter for renewable energy application. *In Journal of Physics: Conference Series* (Vol. 1019, No. 1, pp. 12-20). IOP Publishing.

Barreto, L. H. S., Praca, P. P., Oliveira, D. S., and Silva, R. N. (2014). High-Voltage Gain Boost Converter Based on Three-State Commutation Cell for Battery Charging Using PV Panels in a Single Conversion Stage. *IEEE Transactions on Power Electronics*, 29(1), 150–158. doi:10.1109/TPEL.2013.2248023

Bhattacharjee, S., and Saharia, B. J. (2014). A comparative study on converter topologies for maximum power point tracking application in photovoltaic generation. *Journal of Renewable and Sustainable Energy*, 6(5), 053140.

Birschmann, N. and Heil, J. (2021). DLRmagazine 167–The sky is the limit, *DLR (German Aerosspace Center),* No.167.

Boucher, R. (1984, June). History of solar flight. *In 20th joint propulsion conference*, p. 1429.

Boucher, R. J. (1985). Sunrise, the world's first solar-powered airplane. *Journal of Aircraft*, 22(10), 840-846.

Brizon, M. (2015). Solar energy generation model for high altitude long endurance platforms.

Bruß, H. (1991). Solarmodellflug: Grundlagen, Entwicklung, Praxis. *Verlag für Technik und Handwerk*, Baden-Baden.

Budde-Meiwes, H., Drillkens, J., Lunz, B., Muennix, J., Rothgang, S., Kowal, J., and Sauer, D. U. (2013). A review of current automotive battery technology and future prospects. *Proceedings of the Institution of Mechanical Engineers, Part D: Journal of Automobile Engineering*, 227(5), 761-776. doi:10.1177/0954407013485567

Canis, B. (2013). Battery manufacturing for hybrid and electric vehicles: Policy Issues. Congressional Research Service Report for Congress: R41709.

Cano, Z. P., Banham, D., Ye, S., Hintennach, A., Lu, J., Fowler, M., and Chen, Z. (2018). Batteries and fuel cells for emerging electric vehicle markets. *Nature Energy*, 3(4), 279-289. doi:10.1038/s41560-018-0108-1.

Chan, C. K., Peng, H., Liu, G., McIlwrath, K., Zhang, X. F., Huggins, R. A., and Cui, Y. (2008). High-performance lithium battery anodes using silicon nanowires. *Nature nanotechnology*, 3(1), 31-35.

Chen, H., and Khaligh, A. (2010). Hybrid energy storage system for unmanned aerial vehicle (UAV). *In IECON 2010-36th Annual Conference on IEEE Industrial Electronics Society* (pp. 2851-2856). IEEE.

Cristea M., Chiritoiu V., Costache M., Zaharie I. and Luminosu I. (2010). On a model of the typical cell from a solar panel. *In: AIP Conference Proceedings*, vol 1203, no 1. AIP, pp 433–438.

De Stasi, F. (2015). Working with Boost Converters. *Texas Instrument*.

Duffie, J.A. and Beckman, W. A., *Solar energy thermal proceseses*, 4th edition, John Wiley and Sons, Inc, 2013.

Dyatlov, S. A., Didenko, N. I., Ivanova, E. A., Soshneva, E. B., and Kulik, S. V. (2020). Prospects for alternative energy sources in global energy sector. *In IOP Conference Series: Earth and Environmental Science*, Vol. 434, No. 1, p. 012014, IOP Publishing.

El-Atab, N., Mishra, R. B., Alshanbari, R., & Hussain, M. M. (2021). Solar Powered Small Unmanned Aerial Vehicles: A Review. *Energy Technology*, 9(12), 2100587.

El Kamouny, K., Mahmoudi, H. and Lakssir, B. (2015). Solar charger sizing. *Journal of Electrical Systems*, 11(2), 117-130.

Eltamaly, A. M., and Farh, H. M. (2020). PV Characteristics, performance and modelling. *In Modern Maximum Power Point Tracking Techniques for Photovoltaic Energy Systems* (pp. 31-63). Springer, Cham.

Energy Information Administration [EIA] (May 2021), *Monthly Energy Review*, U.S.

Esram, T. and Chapman, P.L. (2007). Comparison of Photovoltaic Array Maximum Power Point Tracking Techniques. *IEEE Trans. Energy Convers*, 22, 439–449, doi:10.1109/TEC.2006.874230.

Faranda, R., Leva, S., and Maugeri, V. (2008). MPPT techniques for PV Systems: Energetic and cost comparison. *2008 IEEE Power and Energy Society General Meeting - Conversion and Delivery of Electrical Energy in the 21st Century*, 1– 6. Pittsburgh, PA, USA: IEEE.

Farh, H. M. and Eltamaly, A. M. (2020). Maximum power extraction from the photovoltaic system under partial shading conditions. *In Modern Maximum Power Point Tracking Techniques for Photovoltaic Energy Systems* (pp. 107-129). Springer, Cham.

Finger, S., Piccolino, M., and Stahnisch, F. W. (2013). Alexander von Humboldt: galvanism, animal electricity, and self-experimentation part 2: the electric eel, animal electricity, and later years. *Journal of the History of the Neurosciences*, 22(4), 327-352, doi: 10.1080/0964704X.2012.732728.

Gerlitz, E., Greifenstein, M., Hofmann, J., and Fleischer, J. (2021). Analysis of the Variety of Lithium-Ion Battery Modules and the Challenges for an Agile Automated Disassembly System. *Proceedings of the 8th CIRP Global Web Conference, Procedia CIRP*, 96, 175-180. doi:10.1016/j.procir.2021.01.071.

Grazioli, D., Magri, M. and Salvadori, A. (2016). Computational modeling of Li-ion batteries. *Computational Mechanics*, 58(6), 889-909, doi:10.1007/s00466-016-1325-8

Hagen, M., Hanselmann, D., Ahlbrecht, K., Maça, R., Gerber, D., and Tübke, J. (2015). Lithium–sulfur cells: the gap between the state-of-the-art and the requirements for high energy battery cells. *Advanced Energy Materials*, 5(16), 1401986.

Hart, D. W. (2011). Power electronics. New York, NY: McGraw-Hill.

Hegedus, S. S., and Luque, A. (2003). Status, Trends, Challenges and the Bright Future of Solar Electricity from Photovoltaics. *In: Handbook of Photovoltaic Science and Engineering*. John Wiley & Sons, Ltd, pp: 1–43.

Hepperle, M., Ruiz-Leon, A., Runge, H., and Horwath, J. (2007). *HALE platforms-a feasibility study*.

Hoffborn, M. (2009). *A historical survey of solar powered airplanes and evaluation of it's potential market*. Student thesis. Sweden: Mälardalen University, School of Innovation, Design and Engineering.

Hohm, D. P. and Ropp, M. E. (2003). Comparative study of maximum power point tracking algorithms. *Progress in photovoltaics: Research and Applications*, 11(1), 47-62.

Howey, D. A., and Alavi, S. M. (2015). Rechargeable battery energy storage system design. *Handbook of Clean Energy Systems*, 1-18.

Ibrahim, H., and Anani, N. (2017). Variations of PV module parameters with irradiance and temperature. *Energy Procedia*, 134, 276-285.

Ishaque, K., Salam, Z., and Lauss, G. (2014). The performance of perturb and observe and incremental conductance maximum power point tracking method under dynamic weather conditions. *Applied Energy*, 119, 228-236.

Jeddi, N., and Ouni, L. E. A. (2014, November). Comparative study of MPPT techniques for PV control systems. *In 2014 International Conference on Electrical Sciences and Technologies in Maghreb (CISTEM)* (pp. 1-7). IEEE.

Khaligh, A., and Li, Z. (2010). Battery, ultracapacitor, fuel cell, and hybrid energy storage systems for electric, hybrid electric, fuel cell, and plug-in hybrid electric vehicles: State of the art. *IEEE Transactions on Vehicular Technology*, 59(6), 2806-2814. doi:10.1109/TVT.2010.2047877.

Kisacikoglu, M. C., Bedir, A., Ozpineci, B., and Tolbert, L. M. (2012). PHEV-EV charger technology assessment with an emphasis on V2G operation. (Technical Report: ORNL/TM-2010/221) Oak Ridge National Laboratory. doi:10.2172/1050257.

Kranjec, B., Sladic, S., Giernacki, W., and Bulic, N. (2018). PV system design and flight efficiency considerations for fixed-wing radio-controlled aircraft—A case study. *Energies*, 11(10), 2648.

Kul B. (2020). Geçmişten Günümüze Piller. *Takvim-i Vekayi*, 8(1), 104-115.

Lelieveld, J., Klingmüller, K., Pozzer, A., Burnett, R. T., Haines, A., and Ramanathan, V. (2019). Effects of fossil fuel and total anthropogenic emission removal on public health and climate. *Proceedings of the National Academy of Sciences*, 116(15), 7192-7197.

Luo, X., Wang J., Dooner M., and Clarke J. (2015) Overview of Current Development in Electrical Energy Storage Technologies and the Application Potential in Power System Operation. *Applied Energy 137* (January). Elsevier Ltd: 511–536. doi:10.1016/j.apenergy.2014.09.081.

Lynn, P. A. (2011). Electricity from sunlight: an introduction to photovoltaics. John Wiley & Sons.

MacAlpine, S. M. (2014). *Characterization and capture of photovoltaic system losses due to nonuniform conditions* (Doctoral dissertation, University of Colorado at Boulder).

MEPs Ban Cadmium from Power Tool Batteries and Mercury from Button Cells. *European Parliament*. 10 October 2013.

Messenger, R. A., and Ventre, J. (2004). Photovoltaic systems engineering (2nd). *Boca Raton: CRC Press*.

Miao, Y., Hynan, P., Von Jouanne, A., and Yokochi, A. (2019). Current li-ion battery technologies in electric vehicles and opportunities for advancements. *Energies,* 12(6), 1-20. doi:10.3390/en12061074.

Miller, P. (2015). Automotive lithium-ion batteries. *Johnson Matthey Technology Review*, 59(1), 4-13. doi:10.1595/205651315X685445.

Mohamed, A., and Shareef, H. (2011). Hopfield neural network optimized fuzzy logic controller for maximum power point tracking in a photovoltaic system. *International Journal of Photoenergy.*

Mohsin, A. T., & Abdulbaqi, I. M. (2018, January). Analysis of an irrigation pump driver fed by solar PV panel. *In 2018 1st International Scientific Conference of Engineering Sciences-3rd Scientific Conference of Engineering Science (ISCES),* 92-97. IEEE.

Mosa, M., Shadmand, M. B., Balog, R. S., and Rub, H. A. (2017). Efficient maximum power point tracking using model predictive control for photovoltaic systems under dynamic weather condition. *IET Renewable Power Generation*, 11(11), 1401–1409.

Mota, A., and Vieira, J. (2010). Maximum Power Point Tracker Applied to Charging Batteries with PV Panels. *In Solar Collectors and Panels, Theory and Applications*. IntechOpen.

Motahhir, S., El Hammoumi, A., and El Ghzizal, A. (2020). The most used MPPT algorithms: Review and the suitable low-cost embedded board for each algorithm. *Journal of cleaner production*, 246, 118983.

Muratoglu, Y. and Akkaya, A. (2015). Elektrikli Araç Teknolojisi ve Pil Yönetim Sistemi-İnceleme. *Elektrik Mühendisliği Dergisi*, 458, 10-14.

National Transportation Safety Board (2013). Auxiliary Power Unit Battery Fire Japan Airlines Boeing 787-8. Boston, MA.

Nikodem, F., and Bierig, A. (2020). DLR HAP challenges in the development of the high-altitude platform and its applications.

Nguyen, B. N., Nguyen, V. T., Duong, M. Q., Le, K. H., Nguyen, H. H., and Doan, A. T. (2020). Propose a MPPT algorithm based on Thevenin equivalent circuit for improving photovoltaic system operation. *Frontiers in Energy Research*, 8, 14, doi:10.3389/fenrg.2020.00014.

Omar, N., Verbrugge, B., Mulder, G., Van Den Bossche, P., Van Mierlo, J., Daowd, M., Dhaens, M. and Pauwels, S. (2010). Evaluation of performance characteristics of various lithium-ion batteries for use in BEV application. *2010 IEEE Vehicle Power and Propulsion Conference*, 1-6, 1-3 September, Lille, France. doi:10.1109/VPPC.2010.5729083.

Othman, A. M., El-arini, M. M., Ghitas, A., & Fathy, A. (2012). Realworld maximum power point tracking simulation of PV system based on Fuzzy Logic control. *NRIAG Journal of Astronomy and Geophysics*, 1(2), 186-194.

Pandey, A. K., Tyagi, V. V., Selvaraj, J. A., Rahim, N. A., and Tyagi, S. K. (2016). Recent advances in solar photovoltaic systems for emerging trends and advanced applications. *Renewable and Sustainable Energy Reviews*, 53, 859–884.

Podder, A. K., Roy, N. K., and Pota, H. R. (2019). MPPT methods for solar PV systems: A critical review based on tracking nature. *IET Renewable Power Generation*, 13(10), 1615–1632.

Pózna, A. I., Magyar, A., and Hangos, K. M. (2017). Model identification and parameter estimation of lithium ion batteries for diagnostic purposes. *International Symposium on Power Electronics*, 1-6.

Rashid, M. H. (Ed.). (2017). *Power electronics handbook*. Butterworth-Heinemann.

Romeo, G., and Frulla, G. (2004). HELIPLAT®: high altitude very-long endurance solar powered UAV for telecommunication and Earth observation applications. *The Aeronautical Journal*, 108(1084), 277-293.

Runge, H., Rack, W., Ruiz-Leon, A., and Hepperle, M. (2007, September). A solar powered hale-uav for arctic research. *In 1st CEAS European Air and Space Conference* (No. September).

Saharia, B. J., and Saharia, K. K. (2016). Simulated study on nonisolated DC-DC converters for MPP tracking for photovoltaic power systems. *Journal of Energy Engineering*, 142(1), 04015001.

Sharma R. S. and Katti P. K. (2017) . Perturb & observation MPPT algorithm for solar photovoltaic system. *2017 International Conference on Circuit ,Power and Computing Technologies (ICCPCT)*, pp. 1-6, doi: 10.1109/ICCPCT.2017.8074191.

Shiau, J. K., Ma, D. M., Yang, P. Y., Wang, G. F., and Gong, J. H. (2009). Design of a solar power management system for an experimental UAV. *IEEE transactions on aerospace and electronic systems*, 45(4), 1350-1360.

Shpirt, M.Y. and Goryunova, N.P., (2009). Main methods for decreasing the emission of greenhouse gases formed in the production and processing of fossil fuels. *Solid Fuel Chemistry*, Vol. 43, No.6, pp.378-386.

Soloveichik, G. L. (2011). Battery technologies for large-scale stationary energy storage. *Annual Review of Chemical and Biomolecular Engineering*, 2(1), 503-527. doi:10.1146/annurev-chembioeng-061010-114116.

Sukumaran, S., and Sudhakar, K. (2017). Fully solar powered airport: A case study of Cochin International airport. *Journal of Air Transport Management*, 62, 176-188.

Taghvaee, M. H., Radzi, M. A. M., Moosavain, S. M., Hizam, H., and Marhaban, M. H. (2013). A current and future study on non-isolated DC–DC converters for photovoltaic applications. *Renewable and sustainable energy reviews*, 17, 216-227.

Tariq, M., Maswood, A. I., Gajanayake, C. J., and Gupta, A. K. (2017). Aircraft batteries: current trend towards more electric aircraft. *IET Electrical Systems in Transportation*, 7(2), 93-103.

Watts, A. C., Ambrosia, V. G., and Hinkley, E. A. (2012). Unmanned aircraft systems in remote sensing and scientific research: Classification and considerations of use. Remote Sensing, 4(6), 1671-1692.

Wen, J., Zhao, D. and Zhang, C. (2020). An overview of electricity powered vehicles: Lithium-ion battery energy storage density and energy conversion efficiency. *Renewable Energy*, 162, 1629-1648. doi:10.1016/j.renene.2020.09.055

Whiting, K., Carmona, L. G., and Sousa, T. (2017). A review of the use of exergy to evaluate the sustainability of fossil fuels and non-fuel mineral depletion. *Renewable and Sustainable Energy Reviews*, 76, 202-211.

Williard, Nicholas, Wei He, Christopher Hendricks, and Michael Pecht (2013). Lessons Learned from the 787 Dreamliner Issue on LithiumIon Battery Reliability. *Energies* 6 (9): 4682–95. doi:10.3390/en6094682.

Wu Z. and Yu D. (2018). Application of improved bat algorithm for solar PV maximum power point tracking under partially shaded condition. *Appl Soft Comput* 62:101–109.

Xia, Q. (2012). *Solar photovoltaic system modeling and control* (Doctoral dissertation, University of Denver).

Yadav, A. P. K., Thirumaliah, S., Haritha, G., and Scholar, P. G. (2012). Comparison of mppt algorithms for dc-dc converters based pv systems. *International Journal of Advanced Research in Electrical, Electronics and Instrumentation Engineering*, 1(1), 18-23.

Yahdou, A., Hemici, B., and Djilali, A. B. (2017). Modified perturb and observe MPPT control for avoid deviation in photovoltaic systems. *Journal of Electrical Engineering*, 17(1), 10-10.

Yildiz, M., and Karakoc, T. H. (2017) Havacılıkta Kullanılan Bataryaların Tasarım Parametrelerine Göre Boyutlandırılması. *Sürdürülebilir Havacılık Araştırmaları Dergisi*, 2(1), 26-34.

York, R., and Bell, S. E. (2019). Energy transitions or additions?: Why a transition from fossil fuels requires more than the growth of renewable energy. *Energy Research & Social Science*, 51, 40-43.

Young, K., Wang, C., Wang, L. Y., and Strunz, K. (2013). Electric vehicle battery technologies. *In Electric vehicle integration into modern power networks* (pp. 15-56). Springer, New York, NY.

Youtsey, C., Adams, J., Chan, R., Elarde, V., Hillier, G., Osowski, M., McCallum, D., Miyamoto H., Pan, N., Stender, C., Tatavarti, R., Tuminello, F., and Wibowo, A. (2012, April). Epitaxial lift-off of large-area GaAs thin-film multi-junction solar cells. *In CS Mantech Conference* (pp. 23-26).

Vidyanandan, K. V. (2019). Batteries for Electric Vehicles. IEEE

Von Handorf, D.E. (2002). The Baghdad Battery – Myth or Reality?. *Platin and Surface Finishing*, 89(5), 84-87.

Zhang, C., Zhang, C., Li, L., and Guo, Q. (2021). Parameter analysis of power system for solar-powered unmanned aerial vehicle. *Applied Energy*, 295, 117031.

Zhu, Q., Cheng, M., Zhang, B., Jin, K., Chen, S., Ren, Z., and Yu, Y. (2019). Realizing a Rechargeable High-Performance Cu–Zn Battery by Adjusting the Solubility of Cu2+. *Advanced Functional Materials*, 29(50), 1905979, doi: 10.1002/adfm.201905979.

http-1:https://en.wikipedia.org/wiki/La_R%C3%A9publique_(airship)#cite_note-Flight_Vol_I(26)a-1 (Date of access 12.04.2022)

http-2:https://outerzone.co.uk/images/_thumbs/models_more/5471/006.jpg (Date of access 12.04.2022)

http-3: MacCready Solar Challenger,

https://en.wikipedia.org/wiki/MacCready_Solar_Challenger (Date of access 12.04.2022)

http-4: MacCready Gossamer Penguin,

https://en.wikipedia.org/wiki/MacCready_Gossamer_Penguin (Date of access 12.04.2022)

http-5: Solitair at DLR http://www.dlr.de/ft/Desktopdefault.aspx/tabid-1388/1918_read-3385/ (Date of access: 13.04.2022)

APPENDIX-1A. MATLAB/SIMULINK MODEL FOR P&O ALGORITHM

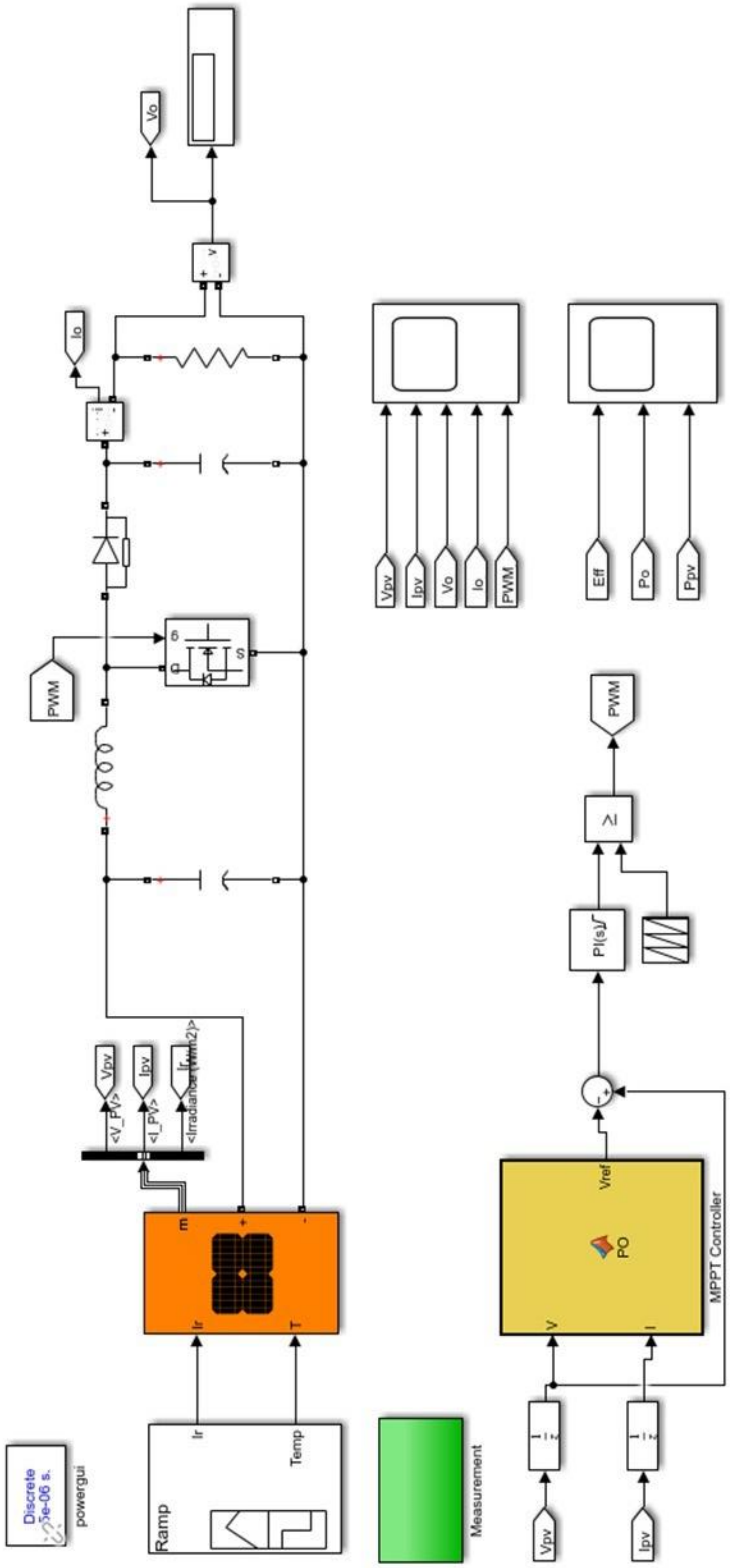

APPENDIX-1B. MATLAB/SIMULINK CODE FOR P&O ALGORITHM

```
function ref_ voltage = pao (pv_voltage, pv_current)

max_ref_voltage = 71.328

min_ref_ voltage = 0;

init_ref_ voltage = 62.352

delta_ref_ voltage = 125e-3

persistent  previous_ voltage previous_power previous_ref_ voltage;

if isempty(previous_V)

   previous_ voltage = 0;

   previous_power= 0;

   previous_ref_ voltage = init_ref_ voltage;

end

pv_power= pv_voltage* pv_current;

dV = pv_voltage – previous_voltage;

dP = pv_ power – previous_power;

if dP ~= 0

         if dP <0

                  if dV<0

                           ref_ voltage = previous_ref_ voltage + delta_ref_ voltage;

                           else

                           ref_ voltage = previous_ref_ voltage - delta_ref_ voltage;

                  end

                  else

                  if dV<0
```

```
                ref_ voltage = previous_ref_ voltage – delta_ref_ voltage;
                else
                ref_ voltage = previous_ref_ voltage + delta_ref_ voltage;
            end
        end
        else
        ref_ voltage = previous_ref_ voltage;
end
if Vref >= max_ref_ voltage %ref_ voltage <= min_ref_ voltage
        ref_ voltage = previous_ref_voltage;
end
previous_ ref_voltage = ref_voltage;
previous_ voltage = pv_voltage;
previous_power= pv_power;
```

APPENDIX-2A. MATLAB/SIMULINK MODEL FOR INCOND ALGORITHM

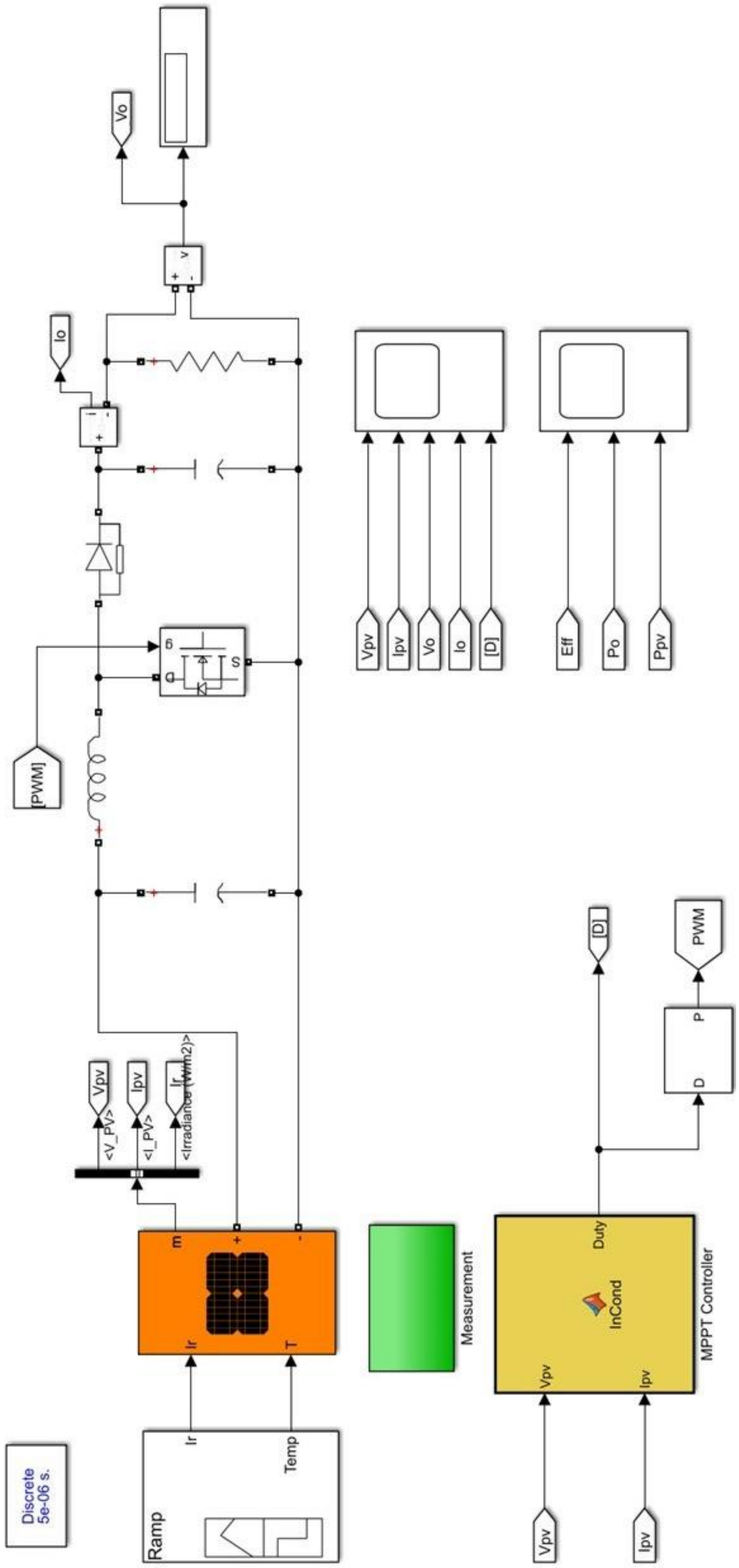

APPENDIX-2B. MATLAB/SIMULINK CODE FOR INCOND ALGORITHM

```
function Duty = InCond(pv_voltage, pv_current)

Delta = 125e-6;

init_duty= 0.45;

min_duty=0;

max _duty=0.85;

persistent previous_voltage previous_duty previous_current;

if isempty(previous_voltage)

    previous_voltage=0;

    previous_current=0;

    previous_duty = init_duty;

end

dV = pv_voltage - previous_voltage;

dI = pv_current - previous_current;

if dV == 0

    if dI == 0

        Duty = previous_duty;

    else

        if dI > 0

            Duty = previous_duty - Delta;

        else

            Duty = previous_duty + Delta;

        end

    end
```

```
else
   if dI/dV == - pv_current / pv_voltage
      Duty = previous_duty;
   else
      if dI/dV > - pv_current / pv_voltage
         Duty = previous_duty - Delta;
      else
         Duty = previous_duty + Delta;
      end
   end
end
if Duty >= max _duty || Duty <= min_duty
   Duty = previous_duty;
end
previous_duty =Duty;
previous_voltage= pv_voltage;
previous_current= pv_current;
```

APPENDIX-3A. MATLAB/SIMULINK MODEL HILL CLIMBING ALGORITHM

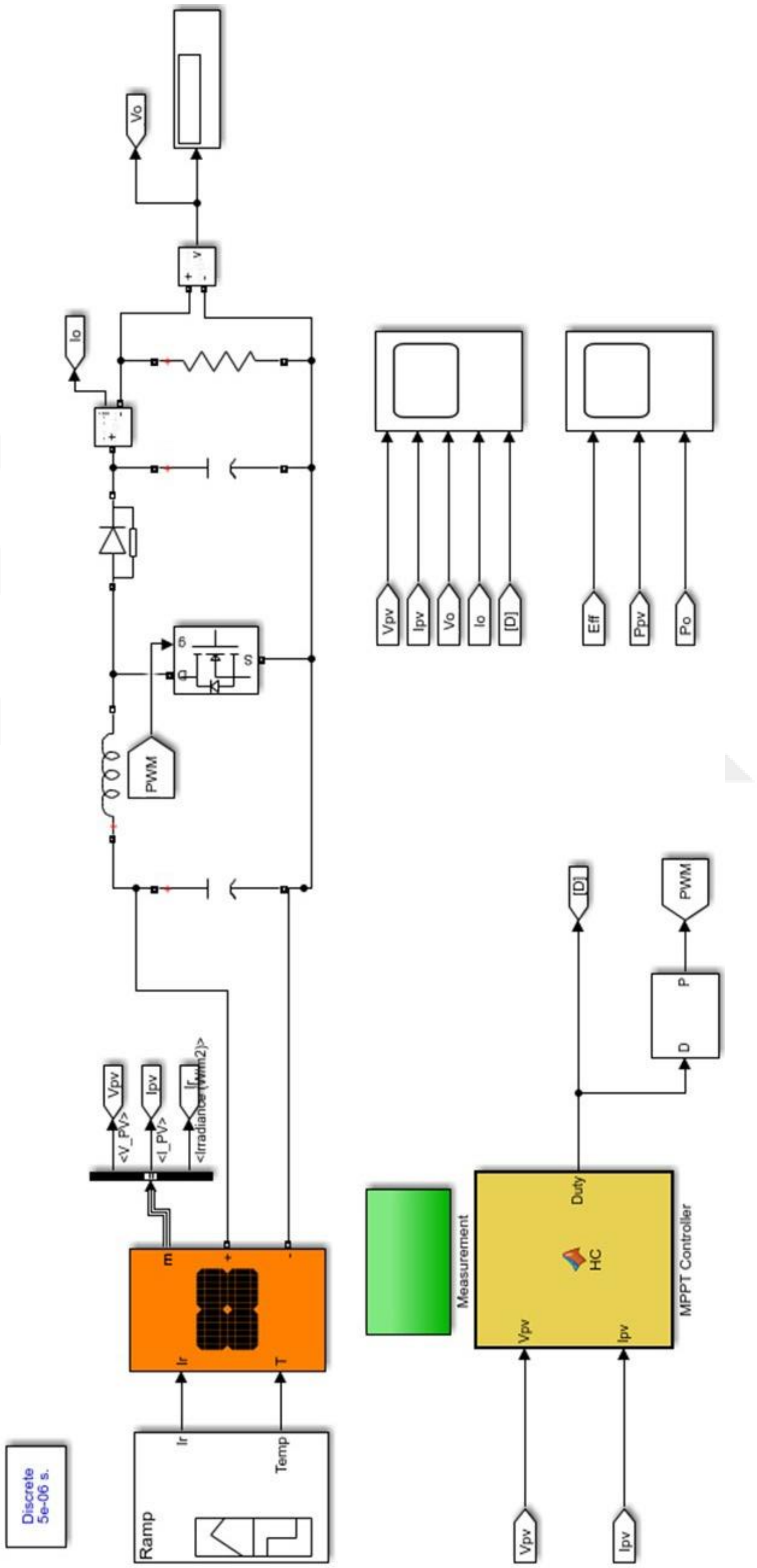

APPENDIX-3B. MATLAB/SIMULINK CODE FOR HILL CLIMBING ALGORITHM

```
function Duty = HC(pv_voltage, pv_current)

Delta = 125e-6;

init_duty= 0.45;

min_duty=0;

max _duty=0.85;

persistent previous_power previous_duty;

if isempty(previous_power)

   previous_power=0;

   previous_duty = init_duty;

end

pv_power= pv_voltage*pv_current;

dP = pv_power – previous_power;


dP= pv_power - previous_power;

if dP ~= 0

   if dP > 0

      Duty = previous_duty + Delta;

   else

      Duty = previous_duty - Delta;

   end

else

   Duty = previous_duty;
```

```
end
if Duty >= max _duty || Duty <= min _duty
   Duty = previous_duty;
end
previous_duty =Duty;
previous_power = pv_power;
```

CURRICULUM VITAE

ORCID ID: Click or tap here to enter text.

Personal Information:

Name - Surname : Özge Küçükkör
Language Profeciency : English

Education and Professional Background:

- **2021 – Present**
  Lecturer, Cappadocia University
- **2020 – Present**
  Department of Civil Aviation, Eskisehir Technical University
- **2018 – 2019**
  Intern, Aircraft Maintenance Engineer, SunExpress Airlines
- **2015 – 2020**
  Department of Avionics, Eskisehir Technical University
- **2011 – 2015**
  Muzaffer Çil Anatolian High School

Project and Articles

TUBITAK 2531 Bilateral Cooperation Program with the German Academic Exchange Service (DAAD), 2021, German Aerospace Center (DLR) - Eskisehir Technical University (ESTU)

Kucukkor O., Aras O., Ozbek E., Ekici S., Karakoc T.H., (2022). Design and Analysis of an IoT Enabled Unmanned Aerial Vehicle to Monitor Carbon Monoxide: Methodology and Application. *International Journal of Global Warming.*

Ozbek E., Aras O., Kucukkor O., Ekici S., Karakoc T.H., (2021). Desing and Testing of an IOT Based Carbon Monoxide Monitoring UAV: Methodology, Challenges, Opportunities. *TUBA World Conference on Energy Science and Technology (TUBA WCEST-2021)*

Aras O., Kucukkor O., Ozbek E., Ekici S., Karakoc T.H., (2020). An Air Quality Measurement Unmanned Aerial Vehicle Design Methodology: Challenges, Opportunities, Costs and Risks. *International Journal of Aviation Science and Technology (IJAST)*